The Dissertation Committee for Dhananjay Kumar

certifies that this is the approved version of the following dissertation:

Analysis of Multicomponent Seismic Data From the Hydrate Ridge, Offshore Oregon

Committee:

Mrinal K. Sen, Supervisor

Paul L. Stoffa, Co-Supervisor

Stephen P. Grand

Nathan L. Bangs

Robert J. Ferguson

Robert H. Tatham

Analysis of Multicomponent Seismic Data From the
Hydrate Ridge, Offshore Oregon

by

Dhananjay Kumar, B.Sc., M.Sc.

Dissertation

Presented to the Faculty of the Graduate School of

The University of Texas at Austin

in Partial Fulfillment

of the Requirements

for the Degree of

DOCTOR OF PHILOSOPHY

The University of Texas at Austin

May, 2005

Dedicated to my parents

Sr. Raghunath Singh & Smt. Shanti Devi

Acknowledgements

First, I would like to sincerely thank my supervisors, Dr. Mrinal K Sen and Dr. Paul L Stoffa for their guidance, encouragement and discussions throughout my graduate studies. I would also like to acknowledge Dr. Steve P Grand, Dr. Nathan L Bangs, Dr. Robert J Ferguson and Dr. Robert H Tatham for serving as my committee members and for their suggestions to improve the dissertation and Dr. William E Galloway for serving as an examining committee member during my PhD proposal.

I would like to thank Dr. Nathan L Bangs, Dr. Yosio Nakamura and Dr. Ingo Pecher for discussions on various issues of gas hydrates and multicomponent seismic data, and other scientists at the Institute for Geophysics their suggestions and help. Also, discussions on multicomponent data analysis with Dr. James E Gaiser (WesternGeco) and Paul Murray (BEG, UT) are acknowledged.

I would like to extend my gratitude to my present and former colleagues at the Institute for Geophysics University of Texas at Austin: Imtiaz Ahmed, Anubrati Mukherjee, Armando Sena, Chandan Kumar, Rishi Bansal, Carmen Gomez, Sanjay Sood, Samarjit Chakraborty, Chengshu Wang, Jason Gumble, Erick Leuro, Irina Filina, Krishnavikas Gudipati, Eric Tuitjer, Sylvia Nordfjord, Alejandro Escalona, Xinxia Wu, Hongbo Lu, Hao Xun, Sasha Carter, Paresh Patel, David Soto, David Gomey, Nedra Bonal, Abdulaziz Al-Aslani, Bob Burger, Timothy Meckel, Robert Rogers, Ricardo Combellas and Martha Jaimes. My

Analysis of Multicomponent Seismic Data From the Hydrate Ridge, Offshore Oregon

Publication No._____

Dhananjay Kumar, Ph.D.

The University of Texas at Austin, 2005

Supervisors: Mrinal K. Sen and Paul L. Stoffa

Multicomponent seismic data can be used to derive P- and S-wave velocity structures of the subsurface, which can be used further to estimate rock and reservoir properties. Most seismic analysis methods and algorithms assume that the earth is isotropic. In many geologic situations, however, sedimentary rocks exhibit anisotropic behavior, and the isotropic assumption will introduce errors in the estimates of the elastic properties of the subsurface. With the goal of analyzing multicomponent seismic data from complex regions (which may show anisotropic behavior), I have developed new algorithms for 1) seismic modeling based on a ray-Born approximation and 2) traveltime computation in tilted transversely isotropic media based on Fermat's principle. This new traveltime computation algorithm is tested on prestack depth migration of a physical model dataset. Such algorithms are essential for estimating subsurface rock properties in complex areas such as the Hydrate Ridge area, offshore Oregon.

I participated in the acquisition of multicomponent seismic data (summer 2002), at the Hydrate Ridge of the Cascadia convergent margin. The primary goal of the experiment was to map the gas hydrates and free gas, and to understand the mechanism of fluid migration. Gas hydrate is an ice-like substance that contains low molecular weight gases (mostly methane) in a lattice of water molecules. Gas hydrates and free-gas are generally detectable with seismic methods because the seismic velocity increases in the presence of gas hydrates, and it decreases in the presence of free-gas. My analysis results in estimates of P- and S-wave interval velocities and anisotropic parameters with the final goal of relating these parameters to the presence and quantification of gas hydrate and free gas. I performed interval velocity analysis in the τ-p (intercept time - ray parameters) domain following three main steps: 1) P-wave velocity analysis, 2) P- to S-wave (converted PS-wave) event correlation, and 3) S-wave velocity analysis. P- to S-wave event correlation is done using synthetic seismograms and traveltime tables. Seismic velocities are correlated to gas hydrate and free gas saturation using a Modified Wood equation. I find that Hydrate Ridge is heterogeneous and is weakly anisotropic (maximum of 10%) in some regions caused possibly by the hydrate veins. The P-wave velocity is more sensitive to the saturation of gas hydrates (maximum of 7% of rock volume) and free gas than the S-wave velocity. The S-wave velocity does not show an anomalous increase in the hydrate-bearing sediments. Thus, I conclude that hydrate does not cement sediment grains enough to affect shear properties. It is more likely that the hydrates are formed within the pore space in this region.

Table of Contents

List of Figures

List of Tables

Symbols

4-C   Four-component data (three-component geophone and a hydrophone)

3-C   Three-component data (two horizontal and a vertical component)

OBS   Ocean bottom seismometer (records 4-C data)

VSP   Vertical seismic profile (records 3-C data)

VTI   Vertical transverse isotropy

TTI   Tilted transverse isotropy (TI with a tilted axis of symmetry)

HTI   Horizontal transverse isotropy (TI with a horizontal axis of symmetry)

NMO   Normal moveout

VFSA   Very fast simulated annealing

p Ray parameter

τ Intercept time (2-way vertical traveltime)

PP-wave   Incident P-wave reflected as P-wave

PS-wave   Incident P-wave reflected as S-wave (converted S-wave)

α_0 Vertical P-wave velocity

β_0 Vertical S-wave velocity

α_{90} Horizontal P-wave velocity

$\delta, \varepsilon, \gamma$ Thomsen's VTI anisotropic parameters (unitless)

HR   Hydrate Ridge

BSR   Bottom simulating reflection

HSZ   Gas hydrate stability zone

Chapter 1: Introduction

1.1 MOTIVATION

Appropriate combinations of elastic properties (seismic wave velocities) of the earth's subsurface can be used to infer reservoir flow properties and lithology. In many geologic situations, estimation of elastic properties is not a trivial task since seismic wave (compressional-wave (P-wave) and shear-wave (S-wave)) velocities vary spatially (i.e., they are heterogeneous) and with the direction of wave propagation (i.e., they are anisotropic). The assumption, therefore, of homogeneity and isotropy in seismic-data analysis can give erroneous results. The importance of anisotropy in seismic exploration has been demonstrated by various authors (e.g., Banik, 1984; Thomsen, 1986, 2002; Isaac and Lawton, 1999).

Both P- and S-wave velocities can be estimated only from multicomponent seismic data. The need to use S-waves together with the P-waves in reservoir characterization (e.g., lithology interpretation and fluid saturation estimation) and the 3-D nature of geological formations has led to the entry of multicomponent technology into exploration (Tatham and McCormack, 1991). In marine surveys, multicomponent data are recorded on instruments placed at the seafloor and in boreholes. In such situations, the S-wave is a converted wave from an incident P-wave at different layer boundaries. Unlike the reflected P-wave paths, the reflected S-wave paths are asymmetric (due to the mix of wave-types) making data analysis more difficult. Even if S-wave data are available, S-wave data analysis methods are not well developed.

1

The university of Texas Institute for Geophysics (UTIG) collected multicomponent seismic data (Ocean bottom seismometer (OBS), and vertical seismic profile (VSP)) during the summer of 2002 at Hydrate Ridge in the Cascadia convergent margin to map the gas hydrates and free gas (methane) and understand the mechanism of fluid migration. The large amount of methane gas trapped in gas hydrates (Kvenvolden, 1999), the possible effects of gas hydrates on continental slope stability and global climate change, and the possibility that it is a hazard for drilling have attracted the attention of the scientific community.

Gas hydrates and free gas can be detected with seismic methods because seismic velocity increases in the presence of gas hydrates and decreases in the presence of free gas (Yuan et al., 1996). The saturation of gas hydrates can be correlated with the seismic velocities (e.g., Lee et al., 1996). Detection and quantification of gas hydrates and free gas require accurate mapping of elastic parameters, and relating these parameters to the saturation of gas hydrates and free gas. The primary goal of my research is to develop advanced seismic data processing tools for the analysis of multicomponent data with application to multicomponent VSP and OBS data from the Hydrate Ridge.

In this chapter, I will review seismic anisotropy, the need for multicomponent data, data analysis steps, and the relevance of each to gas hydrates and the seismic experiment performed on the Hydrate Ridge, offshore Oregon. Finally, I will outline my research objectives and describe the organization of the rest of my thesis chapters.

1.2 SEISMIC ANISOTROPY

Seismic anisotropy is the variation of velocity with direction of wave propagation (e.g., Winterstein, 1990; Figure 1.1) and/or the polarization of shear-waves. In isotropic media, velocity is independent of the direction of wave propagation and particle motion polarization. Seismic anisotropy is likely to be present throughout much of the crust and mantle (e.g., Hess, 1964; Stephen, 1985; Silver and Chan, 1988; Silver, 1996), and a wealth of evidence documents the importance of elastic anisotropy in a wide variety of geological settings (Crampin, 1981; Crampin et al., 1984; Thomsen, 1986, 2002; Winterstein and Paulsson, 1990).

Measurements of seismic velocity anisotropy have revealed that many sedimentary rocks in the earth's subsurface exhibit significant anisotropy (e.g., Helbig, 1994). Shales are intrinsically anisotropic (Banik, 1984; Vernik and Nur, 1992, 1997; Wang, 2002), and they constitute about 75% of sedimentary rock and play an important role in fluid flow and seismic wave propagation. Slowness (inverse of velocity) and polarization anomalies are sensitive diagnostics of anisotropy, and they can be used to infer anisotropy in the subsurface from seismic data. In the past, anisotropy was largely ignored in exploration and production applications due to insufficient and poor quality seismic data. With the recent advances in acquisition and processing of data, the effects of anisotropy are being incorporated in data analysis (e.g., Yilmaz, 2001). There are distinct differences between isotropic and anisotropic media, which will be described in the subsequent sections.

1.2.1 CAUSES OF ANISOTROPY

A range of phenomena may cause rocks to display seismic anisotropy. In most of the cases anisotropy is due to some internal structure on a scale that is small compared to the resolution of the method applied (Crampin et al., 1984). Causes of anisotropy can be categorized as,

1) Intrinsic Anisotropy

a) Crystalline anisotropy, for example anisotropy in the upper mantle due to the preferred orientation of olivine (Hess, 1964), b) Stress-induced anisotropy (Nikitin and Chesnokov, 1984) , and c) Lithologic anisotropy, for example anisotropy due to the presence of shale (Sayers, 1994).

2) Crack-induced Anisotropy

Cracks are likely to be preferentially aligned by a variety of stress-induced processes (Crampin, 1978, 1981, 1987).

3) Long Wavelength Anisotropy

When wave propagation through arrangements of thin parallel layers is simulated by an average simplified anisotropic solid (Backus, 1962).

In general, the cause of anisotropy may not be unique, and the anisotropy of an "effective" medium is often called "apparent anisotropy" (Schoenberg and Douma, 1988). Clays and fine layering in sedimentary rocks are the main causes of seismic anisotropy (Wang, 2002). Transverse isotropy (TI) is the most widely observed anisotropy (Helbig, 1984a, 1984b; Thomsen, 1986, 2002).

1.2.2 ELASTIC TENSORS

The elastic behavior of a homogeneous material with respect to the appropriate seismic wavelengths can be described by its elastic constants (p.60, Auld, 1990). The generalization of Hooke's law for elastic material is that each component of the stress tensor is a linear combination of all components of the strain tensor (Nye, 1957). For linear elasticity, there exist constants C_{ijkl} such that,

$$\tau_{ij} = C_{ijkl}\varepsilon_{kl}\,, \tag{1.1}$$

where $\boldsymbol{\tau}$ is the second order stress tensor, $\boldsymbol{\varepsilon}$ is the second order strain tensor, and $\mathbf{C}$ is the fourth order elastic tensor (i.e., $\mathbf{C}=C_{ijkl}\hat{x}_i\hat{x}_j\hat{x}_k\hat{x}_l$). Equation (1.1) is the elastic constitutive relation. Indices i, j, k and l can take values of 1, 2 or 3 resulting in 81 (3x3x3x3) elastic constants. The elastic coefficient tensor $\mathbf{C}$ has the following symmetries (p.21, Aki and Richards, 2002):

1) $C_{ijkl} = C_{ijlk}$, since $\varepsilon_{kl} = \varepsilon_{lk}$ ($\boldsymbol{\varepsilon}$ is symmetric),

2) $C_{ijkl} = C_{jikl}$, since $\tau_{ij} = \tau_{ji}$ ($\boldsymbol{\tau}$ is symmetric), and $\qquad$ (1.2)

3) $C_{ijkl} = C_{klij}$, on the basis of energy conservation.

From the symmetries above, we recognize that the most general anisotropic solid (triclinic system) has 21 elastic constants. Structures of a 6x6 stiffness matrix $\mathbf{C}$ for various anisotropic systems are described in Auld (1990). Isotropy is the simplest system for which the tensor $\mathbf{C}$ in terms of elastic parameters (λ and μ) becomes, $C_{ijkl} = \lambda\delta_{ij}\delta_{kl} + \mu(\delta_{ik}\delta_{jl} + \delta_{il}\delta_{jl})$.

5

1.2.3 VTI, HTI, AND TTI

VTI

Transverse isotropy is usually associated with a vertical axis of symmetry (Figure 1.2) and a horizontal isotropy plane; it is also called vertical transverse isotropy (VTI). VTI is commonly caused by thin horizontal layering, and it represents a hexagonal symmetry described by five elastic parameters (C_{11}, C_{33}, C_{44}, C_{66}, and C_{13}). Thomsen (1986) re-arranges these parameters and defines a new set that has a more intuitive physical interpretation. Thomsen's parameters (α_0, β_0, ε, δ, and γ) for a VTI medium are defined below (Thomsen, 1986) (symbol '$\approx$' represents the expression for weak anisotropy):

$$\alpha_0 = \sqrt{\frac{C_{33}}{\rho}},$$

$$\beta_0 = \sqrt{\frac{C_{44}}{\rho}}, \tag{1.3}$$

$$\varepsilon = \frac{C_{11} - C_{33}}{2C_{33}} = \frac{\alpha_{90}^2 - \alpha_0^2}{2\alpha_0^2} \approx \frac{\alpha_{90} - \alpha_0}{\alpha_0},$$

$$\gamma = \frac{C_{66} - C_{44}}{2C_{44}} = \frac{V_{SH}^2(90) - \beta_0^2}{2\beta_0^2} \approx \frac{V_{SH}(90) - \beta_0}{\beta_0}, \text{ and}$$

$$\delta = \frac{\alpha_{nmo}^2 - \alpha_0^2}{2\alpha_0^2} \approx \frac{\alpha_{nmo} - \alpha_0}{\alpha_0} \approx 4\left[\frac{\alpha_{45}}{\alpha_0} - 1\right] - \left[\frac{\alpha_{90}}{\alpha_0} - 1\right].$$

6

Following Thomsen (1986), α_0 and β_0 are vertical P- and S-wave velocities respectively, α_{45} and α_{90} are the P-wave velocities at those respective angles, α_{nmo} is the P-wave normal moveout velocity, $V_{SH}(90)$ is the SH-wave horizontal velocity, and ε, δ and γ are dimensionless anisotropic parameters. If ε, δ and γ are very small (< 1), then the anisotropy is called weak. Wave propagation is dominated by δ near vertical propagation, and ε near horizontal propagation. Parameters, ε and γ represent the amount of P- and SH-wave anisotropies, while δ is roughly the difference between P- and SV-wave anisotropies of a medium (Banik, 1987). Intrinsic properties of shales display an $\varepsilon > \delta > 0$ relation (Vernik and Liu, 1997). If $\varepsilon = \delta$, the anisotropy is called elliptic anisotropy, and $\varepsilon - \delta$ is the measurement of anellipticity (deviation from an ellipse). Other parameters used in VTI media are, σ (Tsvankin and Thomsen, 1994), η (Alkhalifah and Tsvankin, 1995), and κ (Sen and Mukherjee, 2003) expressed as,

$$\sigma = \left(\frac{\alpha_0}{\beta_0} \right)^2 (\varepsilon - \delta),$$

$$\eta = \frac{\varepsilon - \delta}{1 + 2\delta}, \tag{1.4}$$

$$\kappa = \frac{\varepsilon - \delta}{(1 + 2\delta)^2} = \frac{\eta}{1 + 2\delta}.$$

The VTI medium has been studied extensively by various researchers including, Daley and Hron, 1977; Berryman, 1979; White, 1982; Helbig, 1984a; Banik, 1984, 1987; Thomsen, 1986, 2002; Graebner, 1992; Tsvankin, 1996, 2001; Alkhalifah, 1998; Fowler, 2003.

HTI

Transverse isotropy with a horizontal axis of symmetry (Figure 1.2) is known as horizontal transverse isotropy (HTI) (Tsvankin, 1997a). This is azimuthally anisotropic and is commonly caused by vertical cracks or fractures (Crampin, 1985). Therefore, HTI parameters may contain information about fracture properties (Tsvankin, 1997a). An HTI medium is better constrained by S-wave analysis since an S-wave splits into two S-wave (or quasi-shear) components traveling with different velocities, when the polarization of the incident S-wave deviates from the strike of aligned fractures (Crampin, 1985). This effect is termed shear wave splitting (MacBeth and Crampin, 1991). The S-wave splitting occurs, in general, when S-wave enters into an effective anisotropic medium (Crampin, 1981).

TTI

Transverse isotropy with a tilted axis of symmetry is known as tilted transverse isotropy (TTI) (Tsvankin (1997b). This type of anisotropy is common in thrust zones with dipping beds (Vestrum et al., 1999). Processing with a VTI assumption in a TTI medium will not image the subsurface correctly (Isaac and Lawton, 1999; Vestrum et al., 1999; Kumar et al., 2003, 2004a). Although the physical reasons leading to TI models with a vertical and a tilted symmetry axis are similar (Figure 1.2), data analysis in TTI media is more difficult, even if the tilt is assumed to be known. TTI media will be studied in detail in Chapter 3.

8
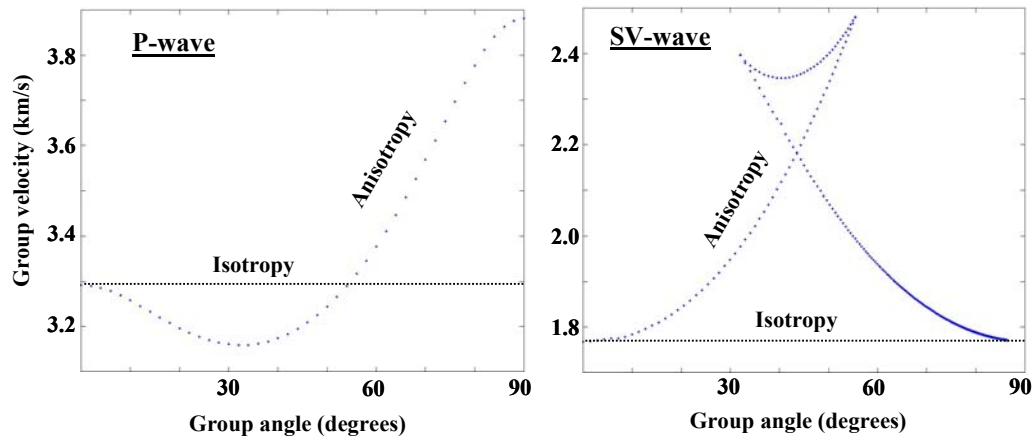
Figure 1.1. Velocity of P- and SV-waves in isotropic and anisotropic medium (Green River Shale): note that the velocity varies with angles of wave propagation in an anisotropic medium but is invariant in an isotropic medium.
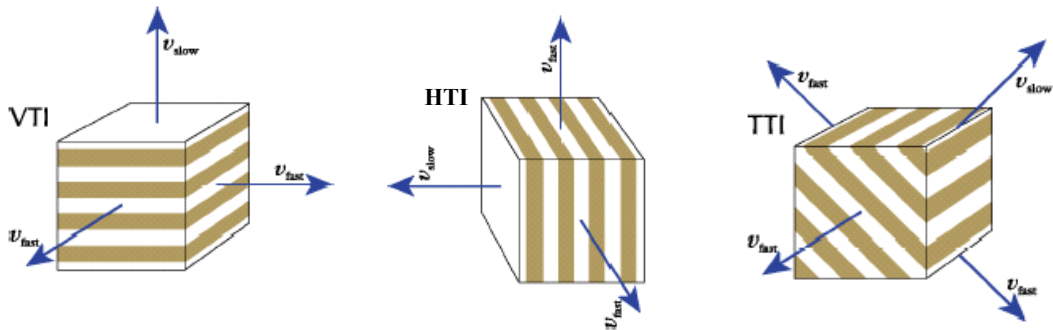
Figure 1.2. Common types of seismic anisotropy (VTI, HTI, and TTI) observed in sedimentary basins: VTI, HTI, and TTI anisotropy are commonly caused by horizontally layered sand-shale formation, vertically aligned parallel fractures, and dipping or thrust formations, respectively. Propagation directions and velocities for P-waves are shown. (Figures modified from Vestrum, 2001).

9

1.3 MULTICOMPONENT SEISMOLOGY

A geophone typically records one component (i.e., vertical) of the vector wavefield response of wave propagation. For a complete description of the wavefield (to analyze both P- and S-waves), multicomponent recording is essential. P- and S-waves have been recorded on three component seismographs by earthquake seismologists (e.g., Lay and Wallace, 1995). In exploration seismics until the 1970s, single component vertical geophones (on land) and pressure sensitive hydrophones (in marine) were typically deployed to record P-waves. The advent of shear-wave applications (Tatham and Stoffa, 1976) and the need for better reservoir images led to the use of multicomponent technology in exploration seismology (Tatham and McCormack, 1991). Multicomponent data improve characterization of the reservoir properties, e.g. porosity, lithology, and fracture parameters.

Ocean-bottom cable (OBC) data and dual-sensor technology (Barr, 1997) (comprising a hydrophone and a vertical geophone on the seafloor), started in the late 1980s. Interest in 4-C (1 hydrophone and 3 geophones) marine acquisition on the seafloor increased when the importance of converted shear-waves was realized (Granli et al., 1999; Jin et al., 2000; Yuan, 2001). Marine multicomponent technology became commercial in the 1990s in the North Sea. Presently multicomponent data are recorded frequently as 4-C data with a cable (OBC) or individual seismometers (Ocean Bottom Seismometer, OBS), and 3-C data are often acquired with vertical seismic profiles (VSPs).

10

1.3.1 ESTIMATION OF ANISOTROPIC PARAMETERS

Anisotropic wave propagation is manifested in seismic data as anomalies in traveltimes, amplitudes and waveforms. Traveltime data are commonly used in seismic parameter estimation with normal moveout (NMO) based analysis (e.g., Tsvankin, 2001). In NMO analysis, a truncated Taylor series is used to approximate the reflection traveltime equation in a common-mid-point (CMP) geometry. van der Baan and Kendall (2002) and Sen and Mukherjee (2003) have given traveltime expressions for NMO in the τ-p (intercept traveltime – ray parameter) domain in a VTI medium. It has been established that from P-wave traveltime analysis alone, three anisotropic parameters (α_0, ε and δ) responsible for P-wave propagation in a VTI medium (dependence on the fourth parameter β_0 is very weak), cannot be determined uniquely from the surface seismic data (Tsvankin and Thomsen, 1994). Anisotropic parameters in a VTI medium (five parameters as shown in equation 1.3) can be estimated with the analysis of multicomponent seismic data.

VSP data are better suited for anisotropic parameter estimation (Hardage, 2000; Macbeth, 2002). Information that can be used for parameter estimation using VSP data are: 1) traveltime (Sayers, 1997; Leaney et al., 1999), 2) slowness vectors (Gaiser, 1990; Miller and Spencer, 1994), and/or 3) polarization vectors (Horne and Leaney, 2000; Dewangan and Grechka, 2003). In the VSP recording, the depth is known and therefore the vertical velocity can be uniquely determined. Estimation of P-wave anisotropic parameters using walkaway VSP and OBS data is discussed in Chapter 4.

11

1.4 SEISMIC DATA ANALYSIS

Seismic data analysis (Claerbout, 1985; Yilmaz, 2001) consists broadly of processing, inversion, and interpretation of seismic data. Interpretation is involved throughout the data analysis (e.g., velocity analysis, model building for imaging). For multicomponent data analysis all three steps can be integrated.

1.4.1 SEISMIC PROCESSING

The principal goal of seismic processing is to derive an image of the earth. A typical processing flow includes preprocessing, deconvolution, velocity analysis, stacking, and migration. Velocity analysis is performed commonly in the CMP (common midpoint) domain for the pure-mode waves (P- or S-wave) and in ACCP (Asymptotic common conversion point) domain for converted shear-waves (incident P-wave reflected back as S-wave) especially for OBC data.

Migration aims at imaging reflectors by removing propagation effects (Berkhout, 1985). There are various methods available for migration (e.g., Schneider, 1978; Stolt, 1978; Gazdag, 1978; Baysal et al., 1983; Claerbout, 1985; Stoffa et al., 1990), and migration methods are based on the solution of the acoustic wave equation. However, elastic migrations that make use of multicomponent data are currently being developed (Zhe and Greenhalgh, 1997; Hokstad, 2000; Hou and Marfurt, 2002). Migration and inversion are very closely related processes. Stolt and Weglein (1985) define migration as an inversion process which derives 2-D/3-D maps of local reflectivity from seismic data.

1.4.2 SEISMIC INVERSION

Seismic inversion produces an earth model in depth (e.g., Xia et al., 2000), described by the elastic properties of the subsurface materials (rocks and fluids). Thus it is an elastic parameter estimation method (e.g., Sen and Stoffa, 1991; Xia et al., 1998). This method can be used further to estimate the reservoir properties (fluid saturation, pore pressure, and fracture properties) using a rock physics model and/or amplitude versus offset (AVO) analysis (Connolly, 1999; Duffaut et al., 2000; Mallick et al., 2000; Goodway, 2001).

Seismic inversion typically involves matching of theoretical and observed data resulting in a model that "best fits" the data (Tarantola, 1987). Seismic inversion is iterative in nature and repeated until a satisfactory result is obtained in terms of data fitting and the validity of the result (model) in a given geological setting. In general, there are many sets of model parameters that fit the data to the same level of confidence, so there is always ambiguity in the inversion result (Menke, 1984). Ambiguity can be reduced by imposing constraints on the model parameters obtained from other sources. The resolution of estimated model parameters depends on the data quality, data coverage (amount and distribution of data), data types (prestack or poststack), type of data (only traveltime or amplitude or both i.e., full waveform) and the inversion method used (linear or nonlinear). Prestack waveform inversion with good quality data is expected to give better model parameter estimates. Data interpretation is involved throughout the inversion process.

13

1.5 GAS HYDRATES AT THE HYDRATE RIDGE

Gas hydrate occurs naturally as a solid composed of rigid cages of water molecules that enclose small gas molecules (mostly methane) (Sloan, 2000, 2003). It is widely present in permafrost and deep oceanic environment (Kvenvolden, 1988). In the oceanic environment, methane hydrates are usually stable at temperatures in the range of 0^0C to 15^0C, water depths greater than 500m and sediment depths up to 300m below the seafloor (Figure 1.3a). The formation and the occurrence of gas-hydrates require the presence of gas and water in the thermodynamic stability range. Gas hydrate is of interest to many international geoscientists, due to the various possibilities associated with gas-hydrate as (Figure 1.3b) 1) a major future energy source (Kvenvolden, 1999), 2) possible geohazard (Bagirov and Lerche, 1997; Henriet and Mienart, 1998), and 3) a potential green-house gas (Kvenvolden, 1993; Hornbach et al., 2004).

1.5.1   PROPERTIES OF GAS-HYDRATE BEARING SEDIMENT

The presence of gas hydrate changes the physical properties of sediment, replacing pore-space fluid with a solid, reducing the permeability, lowering the chlorinity of pore water upto 20%, and significantly increasing the seismic velocities. For pure hydrates, the P-wave velocity is 3.8 km/s, and the S-wave velocity is 1.7 km/s. A unit volume of methane hydrates (structure I hydrate) at one atmosphere pressure produces 160 unit volumes of gas (Kvenvolden, 1993) that is proportional to its (hydrates) density (0.91 g cm^{-3}), and molecular weight (124 g mol^{-1}) (Dickens et al., 1997).

14
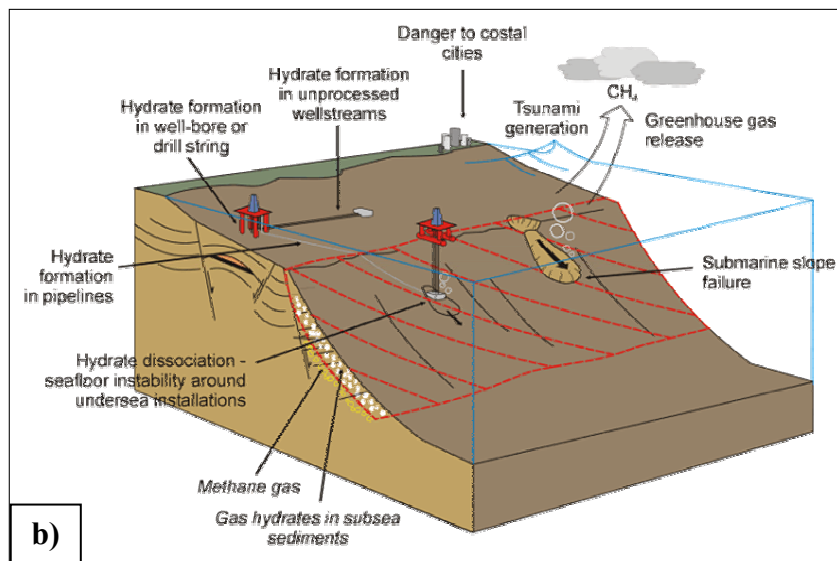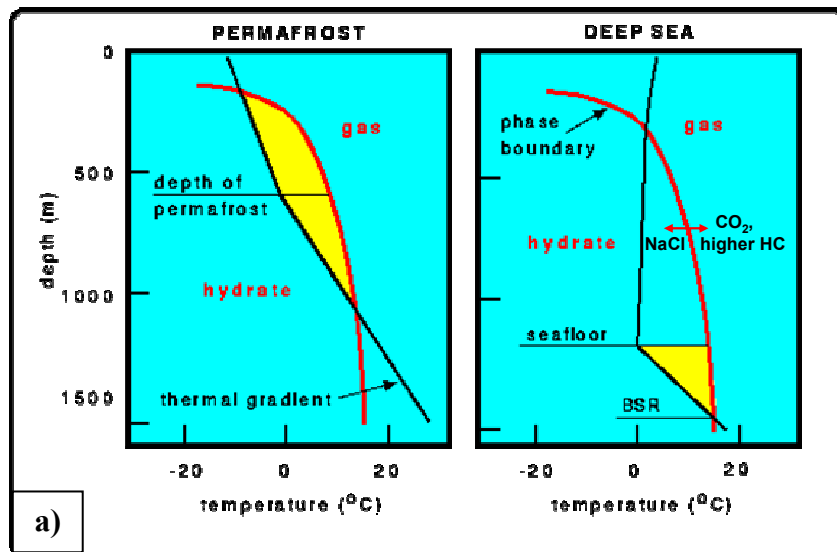
Figure 1.3. a) Phase diagram showing thermodynamic stability range of hydrates in a pure water/methane system (area highlighted with the yellow color) in permafrost and deep sea sediments (after Kvenvolden, 1988). b) Various issues of gas hydrate in marine settings (From the website of Centre for Gas Hydrate Research, Heriot-Watt University, Edinburgh, UK).

15

1.5.2 DISTRIBUTION AND SATURATION OF GAS HYDRATE

The contact between gas hydrate and free gas below the gas hydrate makes a strong acoustic interface, which is evident in a seismic section as a very bright reflection known as a bottom simulating reflection (BSR). Seismic velocity increases in the presence of gas hydrates (e.g., Shipley et al., 1979; Yuan et al., 1996). The velocity also increases if the hydrate content in the pore spaces increases (Hyndman and Spence, 1992). The presence of a BSR and a seismic velocity anomaly can help in detection and quantification of gas-hydrate and free-gas. Seismic velocity has been widely used (other methods are resistivity data from well logs, chloride measurement from core data, infra-red camera, and pressure core sampler) to estimate the saturation of gas hydrates and free gas (Lee et al., 1996; Ecker et al., 2000; Lu and McMechan, 2002).

1.5.3 THE HYDRATE RIDGE EXPERIMENT

Hydrate Ridge (HR) is a 25-km long and 15-km wide accretionary ridge in the Cascadia convergent margin (MacKay, 1995); formed as the Juan de Fuca plate subducts obliquely beneath the North American plate (Figure 1.4). A two-ship seismic experiment was conducted during summer 2002 with the seismic ship *Maurice Ewing* and the drilling ship *JOIDES Resolution*. The cruise was designed to acquire surface (streamer recording, MCS) and subsurface (VSP and OBS) seismic data, to map the elastic properties of gas hydrate and free gas beneath the HR. Hydrates and its seismic proxies (BSR, and amplitude blanking) appear to be well developed beneath the HR (Trehu et al., 1999).
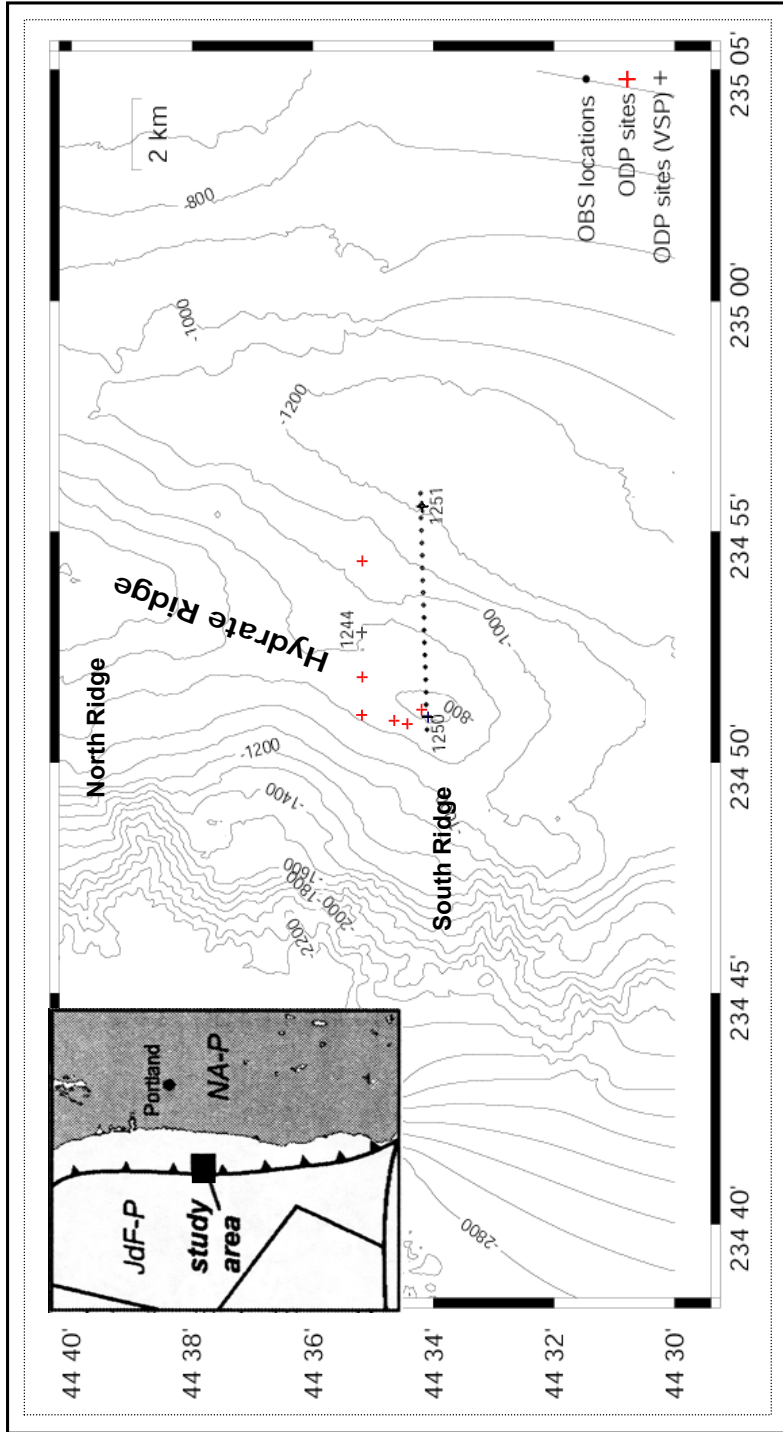
Figure 1.4. Bathymetry map (contours in m) on the Hydrate Ridge of the Cascadia convergent margin. The ridge is characterized by a northern peak having a minimum water depth of 600 m and a southern peak with a water depth of 800 m. Drilling and seismic experiment (VSP and OBS) are concentrated on the south summit. Inside map shows subduction of the Juan de Fuca plate (JdF-P) beneath the North American plate (NA-P).

17

1.6 OBJECTIVES AND ORGANIZATION

My objectives include development of new algorithms for multicomponent seismic data analysis and applying those to data acquired at the Hydrate Ridge. My analysis aims at estimating the P-wave and S-wave velocity and anisotropic parameters with the final goal of relating these parameters to the presence and quantification of gas hydrates and free gas.

The first few chapters are focused on the development of methods followed by applications to seismic data from the Hydrate Ridge (HR). Basic elements of computing synthetic seismograms in anisotropic media based on a ray-Born method are discussed in Chapter 2. A new method of P-wave traveltime calculation in tilted transversely isotropic media and its extension to S-wave traveltime computation in VTI media are presented in Chapter 3. The traveltime computation method has been used for P-wave anisotropic prestack depth migration using a physical model dataset, and subsequently for traveltime inversion in anisotropic media. Chapters 4 and 5 are focused on the analysis of P- and S-wave data, respectively from HR. Chapter 6 summarizes the research and highlights future research areas.

Chapter 2: Synthetic seismogram in anisotropic media: a ray-Born approach

2.1 INTRODUCTION

The general theory of wave propagation in anisotropic elastic solids is well known (Love, 1944; Auld, 1990; Červený, 2001; Carcione, 2001; Aki and Richards, 2002). Some of the theoretical insights and numerical techniques have been reviewed by Crampin (1981). In an anisotropic medium, there are three types of body waves, namely, a quasi-compressional (qP) wave and two quasi-shear (qS1 and qS2) waves that propagate with different velocities and particle motions which vary with direction.

Advances in our understanding of wave propagation in uniform layered anisotropic media have been achieved principally as a consequence of extensive numerical experimentation with computer modeling. Synthetic seismograms give valuable insights into the behavior of seismic waves in complicated earth models. Constructing seismogram requires the solution of the elastodynamic wave equation (a linearized momentum equation) given by (e.g., p.9, Červený, 2001)

$$\rho \ddot{\mathbf{u}} = \nabla . \boldsymbol{\tau} + \mathbf{f} , \tag{2.1}$$

where ρ is the mass density of the medium, $\ddot{\mathbf{u}}$ is the second order time derivative of the displacement vector $\mathbf{u}$, and $\mathbf{f}$ is a body force. The stress tensor $\boldsymbol{\tau}$ is given by equation (1.1), and then the elastodynamic wave equation (in a Cartesian axis system) in homogeneous media in a source free region can be written as

19

$$c_{ijkl}u_{l,ki} = \rho\ddot{u}_j .$$

(2.2)

```
                    ┌──────────────────────────┐
                    │  Seismic modeling methods │
                    └──────────────────────────┘
```
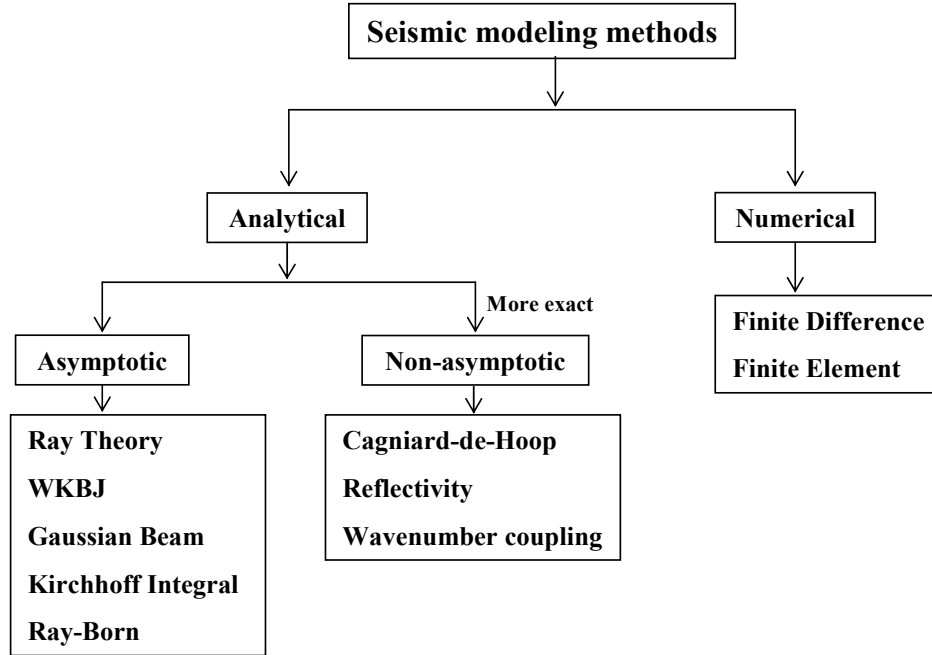
Figure 2.1. Various seismic modeling methods.

There are various methods available to solve the wave equation (equation 2.1) as summarized in Figure 2.1. They can be broadly classified into two categories: analytical methods and numerical methods (e.g., Sen, 2002). Numerical methods can handle all kinds of model complexities, but they are computationally expensive. On the other hand analytical methods either make use of approximate models or derive an approximate solution. For example, the

reflectivity method (Fuchs and Müller, 1971; Kennett, 1983) is valid for modeling in 1-D layered media. Booth and Crampin (1983) have extended the reflectivity technique for calculating synthetic seismogram in plane-layered models to include layers with general anisotropy. Modeling in inhomogeneous and anisotropic media is done mostly with asymptotic methods (Červený, 1972, 2001), because they are fast and work well for most of the models. I will discuss one of these, a ray-Born method for seismogram synthesis in anisotropic media.

2.2 RAY-BORN METHOD

Ray perturbation theory and the Born approximation have been used for seismic modeling and inversion (Farra and Madariaga, 1987; Coates and Chapman, 1990; Jin et al., 1992). In the Born approximation, the wave equation is linearized by considering the medium as a perturbation from a background model (Beyklin and Burridge, 1990). Ray theory is used to find the solution in background media and Born approximation gives the perturbation response over background media. The aim of this method is to model the effects of the nature and distribution of localized perturbations from the long wavelength model (Beydoun and Mendes, 1989; Eaton and Stewart, 1994). In the ray-Born method the scattered wavefield is the ray-Born approximate solution of the wave equation. The ray-Born solution of a wave equation requires knowledge of the phase velocity, group velocity, polarization vector, and Green's function in the background media.

2.3 PARAMETERS REQUIRED FOR RAY-BORN SYNTHETICS

2.3.1 GROUP VELOCITY AND PHASE VELOCITY

The velocity of a wave is defined by the phase difference between the vibrations observed at two different points in a free plane wave (e.g., Lecture 12, Sen, 2002). A plane wave represented by $\psi = A\cos(\mathbf{k}.\mathbf{x} - \omega t)$ travels along x axis with a phase velocity $\mathbf{v}_P = \omega \dfrac{\hat{\mathbf{k}}}{|\mathbf{k}|}$, where $\mathbf{k}$ is a wavenumber vector and A is the maximum amplitude of the plane wave (e.g., p.16, Auld, 1990). Note that the velocity of plane wave propagation is referred to as the 'phase velocity'. Consider a change of amplitude impressed on a train of waves like modulation impressed on a carrier. Modulation results in the building up of some groups or packets of amplitude that move with a velocity different from the phase velocities of the constituent plane waves and is called the 'group velocity' (e.g., p.253, Aki and Richards, 2002). A simple combination of groups are obtained when one plane wave is superimposed on another plane wave with slightly different phase velocity and frequency such that

$$\cos(\mathbf{k}.\mathbf{x} - \omega t) + \cos[(\mathbf{k} + \delta\mathbf{k}).\mathbf{x} - (\omega + \delta\omega)t] = 2\cos[(\mathbf{k} + \frac{\delta\mathbf{k}}{2}).\mathbf{x} - (\omega + \frac{\delta\omega}{2})t]\cos(\frac{\delta\mathbf{k}}{2}.\mathbf{x} - \frac{\delta\omega}{2}t)$$

where on the right side of above equation, the first (cosine) term corresponds to a carrier wave (propagates with phase velocity, $\mathbf{V}_P$) and the second term corresponds to the modulation envelope which propagates with group velocity, $\mathbf{V}_g$, such that (following section 7.H, p.227, Auld, 1990)

22

$$V_P = (\omega + \frac{\delta\omega}{2}) \frac{\hat{k}'}{\left|\mathbf{k} + \dfrac{\delta\mathbf{k}}{2}\right|} \rightarrow \frac{\omega}{\mathbf{k}}, \tag{2.3}$$

and,

$$V_g = \frac{\delta\omega}{|\delta\mathbf{k}|} \hat{k}'' \rightarrow \frac{\partial\omega}{\partial\mathbf{k}}. \tag{2.4}$$

The expression after "$\rightarrow$" is for the non-dispersive media. Unit vectors in above equations (2.3 and 2.4) are given by,

$$\hat{k}' = \frac{\mathbf{k} + \dfrac{\delta\mathbf{k}}{2}}{\left|\mathbf{k} + \dfrac{\delta\mathbf{k}}{2}\right|}, \tag{2.5}$$

and,

$$\hat{k}'' = \frac{\delta\mathbf{k}}{|\delta\mathbf{k}|}, \tag{2.6}$$

where $\hat{k}''$ is in the direction where the variation of ω with respect to $\mathbf{k}$ is maximum. In three dimensions the group velocity therefore becomes (if dispersion relation is given by $\omega = f(k_x, k_y, k_z)$)

$$V_g = \frac{\delta\omega}{\delta k_x} \hat{x} + \frac{\delta\omega}{\delta k_y} \hat{y} + \frac{\delta\omega}{\delta k_z} \hat{z}. \tag{2.7}$$

The relation between group velocity and phase slowness in general media can be derived from the plane wave equation (Figure 2.2; Garmany, 1989) given by

$$\mathbf{p}.\mathbf{x} = t ,$$ (2.8)

where $\mathbf{x}$ is the distance traveled in time t with wave slowness $\mathbf{p}$. In terms of group velocity, the equation of a plane wave (equation 2.8) can be written as

$$\mathbf{p}.\frac{\mathbf{x}}{t} = \mathbf{p}.\mathbf{V}_g = 1 .$$

This shows that the scalar product of the phase slowness vector and group velocity vector is always unity. Also, the group velocity $V(\phi)$ at group angle ϕ, is expressed through the phase velocity (wavefront velocity, $v(\theta)$) at phase angle θ as (e.g., Berryman, 1979)

$$V^2(\phi(\theta)) = v^2(\theta) + \left(\frac{dv}{d\theta}\right)^2 .$$ (2.9)

Phase slowness enters naturally in the discussion of wave propagation and a slowness surface is the fundamental entity. Figure 2.3 describes the relationship between a slowness surface and a group velocity surface. Appendices A and B discuss the algorithms for analytical estimation of phase slowness and group velocity.
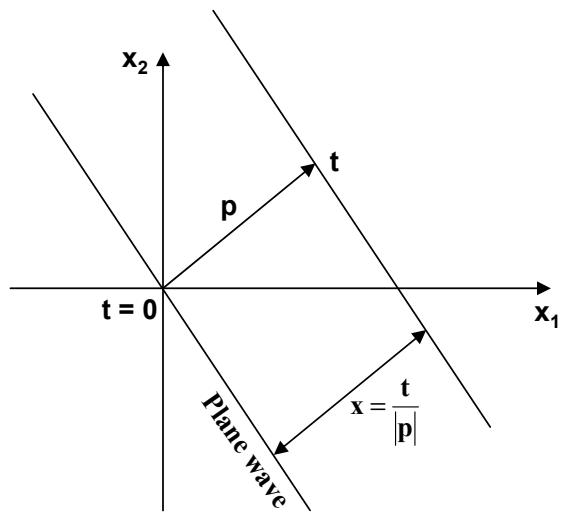
Figure 2.2. Plane wave propagation ($\mathbf{p}.\mathbf{x} = t$). Normal to the plane wave in regular space (x_1, x_2) is parallel to the slowness vector ($\mathbf{p}$) in slowness space (p_1, p_2). (Garmany, 1989).
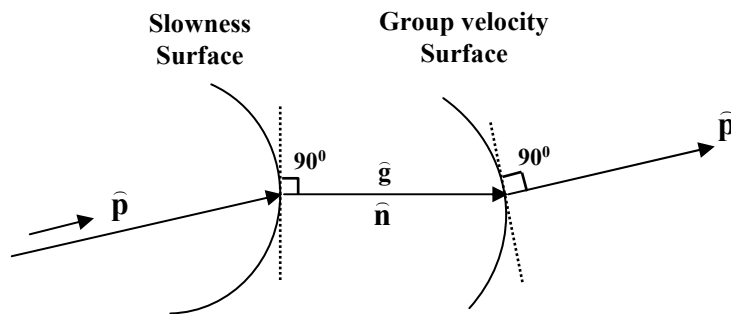
Figure 2.3. Schematic diagram showing the relation of slowness surface and group velocity surface, where $\widehat{\mathbf{p}}$ is slowness direction, $\widehat{\mathbf{g}}$ is group velocity direction, and $\widehat{\mathbf{n}}$ is normal to the slowness surface. Notice that, normal $\widehat{\mathbf{n}}$ is parallel to $\widehat{\mathbf{g}}$, and slowness direction is normal to the group velocity surface.

Now I will show some examples of slowness and group velocity surfaces calculated with the algorithms discussed in appendices A and B, and compare my results with some published results given in Auld (1990) for validating my algorithms. Table 2.1 lists the elastic properties and density for a few natural materials.

Elastic coefficients (Auld, 1990)								
Material	System	Density	C_{11}	C_{33}	C_{44}	C_{12}	C_{13}	C_{14}
Quartz	Trigonal	2651	8.674	10.72	5.794	0.699	1.191	1.791
Thomsen's parameters (Thomsen, 1986)								
Material	System	Density	α_0 (m/s)	β_0 (m/s)		ϵ	δ	γ
GRS	Hexagonal	2075	3292	1768		0.195	-0.22	0.18
BSS	Hexagonal	2140	4206	2664		0.002	0.020	0.005

Table 2.1. Elastic coefficients for some natural materials in terms of c_{ij} or Thomsen's parameters, where, c_{ij} is in 10^{10} N/m^2, density is in kg/m^3. GRS stands for Green River Shale (found in many central US basins) and BSS stands for Berea sandstones.

Figure 2.4 shows the group-velocity surfaces and slowness surfaces in the xz plane and xy plane for a pure crystalline material Quartz (Table 2.1). Notice the triplication in S-wave group-velocity surfaces. Triplications occur when one

ray direction is associated with more than one phase direction. Figures 2.4(d) and 2.4(b) match with Figures 3.6 and 3.8 in Auld (1990), respectively. Figure 2.5 shows the 2-D (xz plane) and 3-D group-velocity surfaces and slowness surfaces for a Green River Shale (a VTI medium, Table 2.1). In this model, wave propagation in the horizontal plane (xy plane, Figures 2.5 c & d) behaves as in an isotropic medium whereas the two S-waves propagate with different velocities (they are the same in an isotropic medium).

A set of vertical parallel fractures in an isotropic background makes the medium HTI. Schoenberg and Douma (1988) and Hudson (1981) developed equivalent media theory for rotationally invariant parallel fractures (linear slip model) and for penny shaped cracks, respectively. Figure 2.6 shows a 3-D group-velocity surface and a slowness surface in a fractured medium (HTI). This fracture system is modeled by incorporating normalized (horizontal) fractures, with parameters, E_n (30%) and E_t (10%) into a VTI medium. The result is a VTI medium (Schoenberg and Douma, 1988). HTI results when a VTI medium is rotated by 90^0 with respect to one of the horizontal axes. In the present (HTI) model, fractures strike in the y-direction, and therefore, the yz-plane behaves as an isotropic medium (similar to the xy-plane in VTI). The fracture system can also be incorporated in any dip and azimuth, for which the effective elastic coefficient matrix can be computed using equivalent media theory and Alford rotation, and then phase and group velocities can easily be evaluated.
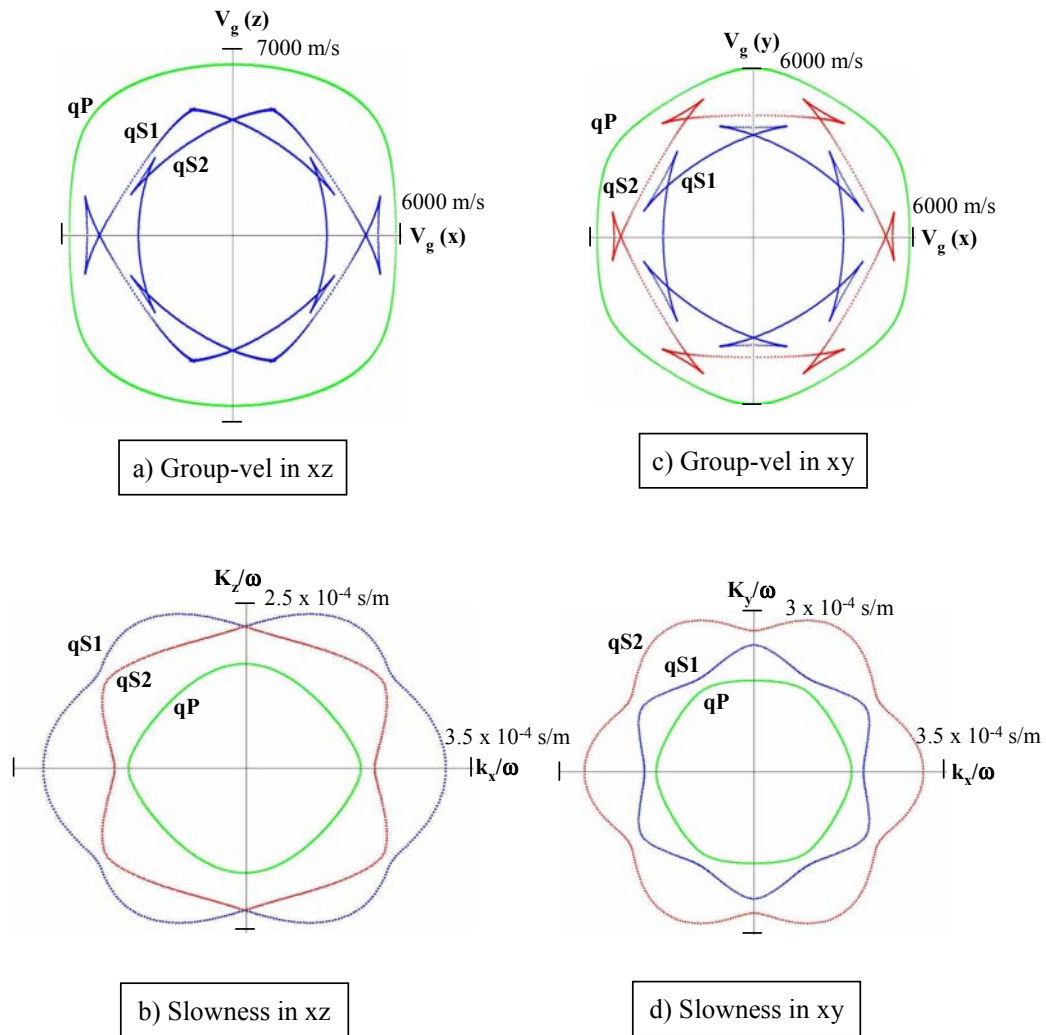
Figure 2.4. Group velocity surfaces (a, d) and slowness surfaces (b, c) in xz plane and xy plane for Quartz. Wavefields are separated in slowness domain in xy plane. Figures 2.4 (d) and 2.4 (b) match with Figures 3.6 and 3.8 in Auld (1990), respectively.

a) Group-vel in xz

b) Slowness in xz

c) 3-D Group-vel
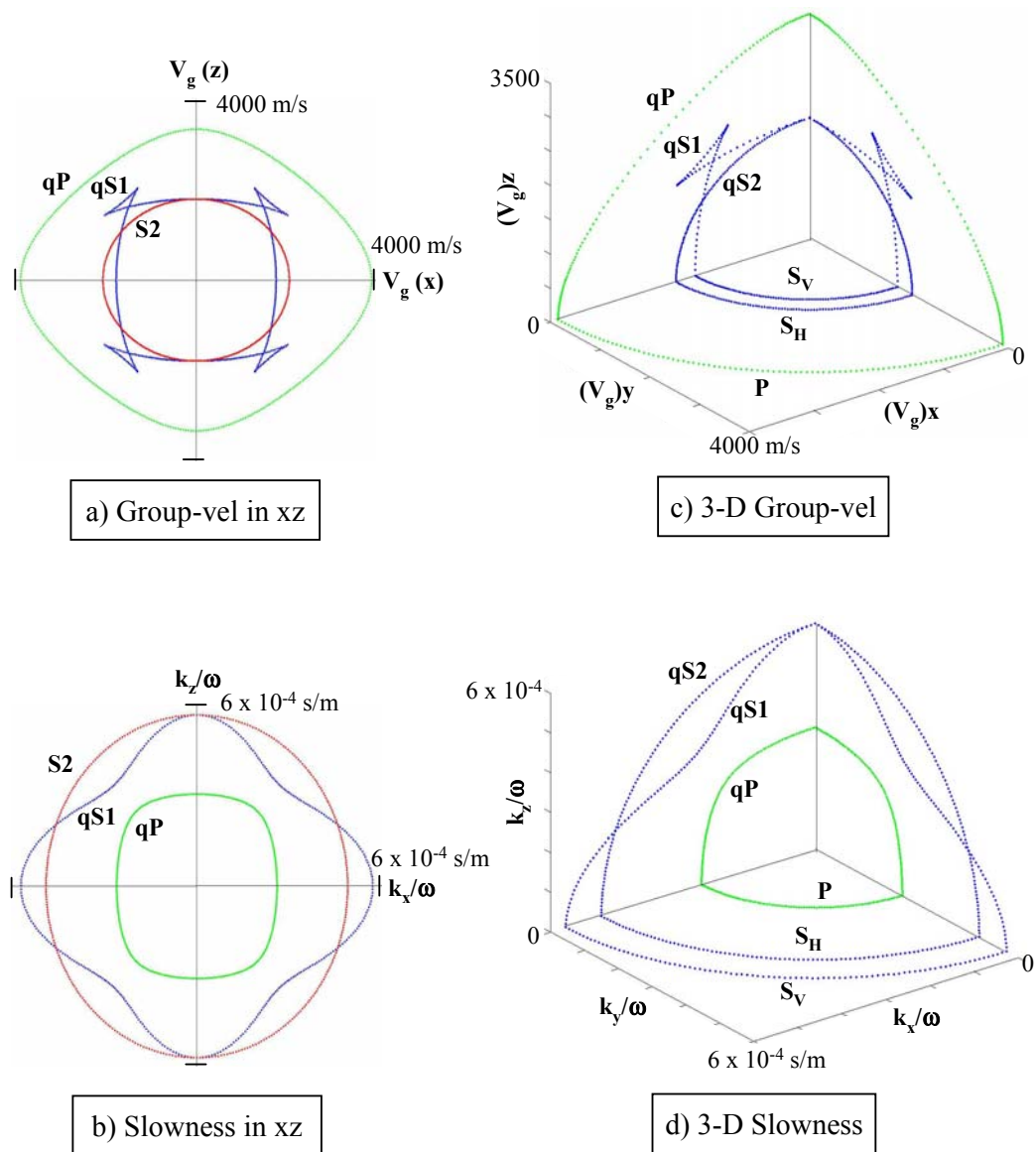
d) 3-D Slowness

Figure 2.5. Group velocity surface (a) and slowness surface (b) in xz plane for Green River Shale. Figures c and d show the 3-D plot of group velocity surface and slowness surface. GRS is a VTI medium. It behaves as an isotropic medium in the xy plane.
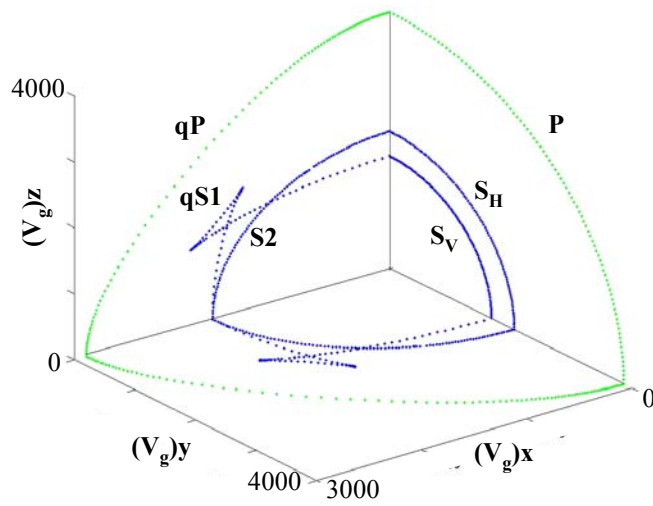
a) 3-D Group-vel
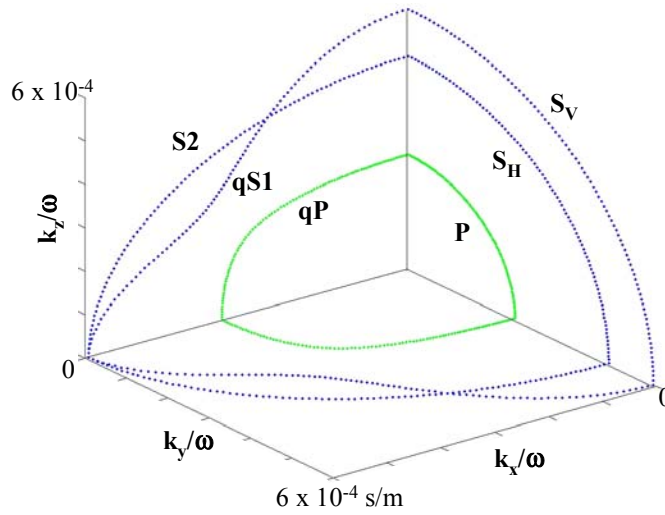
b) 3-D Slowness

Figure 2.6. 3-D plots of group velocity surface (a) and slowness surface (b) for a fractured medium (HTI). It behaves as an isotropic medium in the fracture plane (yz plane) with fractures strike in y-direction.

30

2.3.2 POLARIZATION VECTOR

A polarization vector describes the particle motion direction of a seismic wavefield (Vidale, 1986), and it can be obtained from the solution of an Eigen value problem involving the Christoffel equation (equation A.1). Slowness and polarization information are used to discriminate different wave types. As shown in the Figures 2.4 to 2.6, shear-waves (qS1 and qS2) may have the same velocity (called singular points) for a particular propagation direction, and they can only be differentiated with the polarization information (Chapman and Shearer, 1989) as shown in Figure 2.7. It is also useful in anisotropic parameter estimation (e.g., Horne and Leaney, 2000).
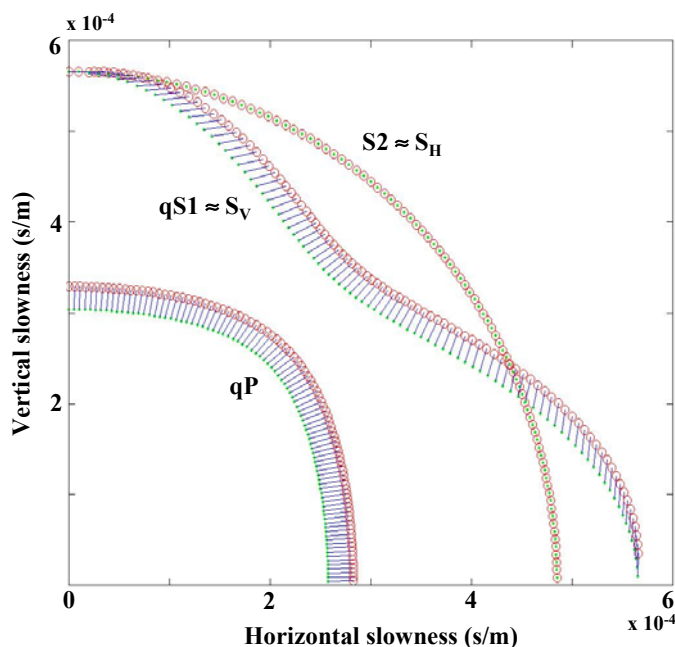
Figure 2.7. Polarization vectors with slowness surface in xz plane for Green River Shale (Table 2.1). SH-wave is polarized into the plane. Polarization direction is used to distinguish qS1- and qS2- waves.

31

2.3.3 GREEN'S FUNCTION AND RADIATION PATTERN

The displacement field (at a given point in space and time) from a unidirectional impulsive source (point source) is the elastodynamic Green's function (e.g., P.27, Aki and Richards, 2002). This means that the Green's function is the point source solution of the wave equation. In a heterogeneous medium, the Green's function cannot be evaluated analytically, and approximate Green's functions are generally used. The ray-Born method makes use of a ray-theoretical Green's function (e.g., Ben-Menahem et al., 1991; Vavryčuk, 1997; Pšenčík, 1998). In a homogeneous and anisotropic medium, the Green's function is given by (Eaton and Stewart, 1994)

$$G_{mk}(\mathbf{r},\mathbf{s},\omega) = \sum_{\Omega} \frac{g_m g_k e^{i\omega \mathbf{p}.(\mathbf{r}-\mathbf{s})}}{4\pi\rho V |r-s|\sqrt{K}} \tag{2.10}$$

and in a homogeneous and isotropic medium, it reduces to

$$G_{mk}(\mathbf{r},\mathbf{s},\omega) = \sum_{\Omega} \frac{g_m g_k e^{i\omega|x-s|/V}}{4\pi\rho V^2 |r-s|}, \tag{2.11}$$

where $\mathbf{r}$ is the receiver location, $\mathbf{s}$ is the source location, $|r-s|$ is the distance between source and receiver, V is the group velocity, K is the Gaussian curvature of slowness surface (Ben-Menahem and Sena, 1990), g_m and g_k are the source and receiver polarization where subscripts m and k represents source and receiver polarization direction respectively, $\mathbf{p}$ is the ray parameter, and Ω

represents summation over different wavetypes. The exponent in equation (2.10) is given by

$$\mathbf{p}.(\mathbf{r}-\mathbf{s}) = \frac{1}{v_{phase}}|r-s|\cos(\psi),\qquad\qquad(2.12)$$

where ψ is the angle between group and phase velocity direction, and v_{phase} is the phase velocity.

The radiation pattern due to a point source is given by the Green's function (Gajewski, 1993). I consider a Green River Shale model for calculating the radiation pattern. Figures 2.8 and 2.9 show the radiation patterns in the vertical plane for P- and SV-waves (qP- and qS1-waves) respectively in a homogeneous and anisotropic medium (GRS). Isotropic (equation 2.19) and anisotropic (equation 2.18) radiation patterns are shown in the same plot in red and blue color respectively.

In Figures 2.8 and 2.9, receivers are placed 200m away from the source in a semi-circular geometry. The numbers shown for the contours (2, 4, 6, and 8 in the P-wave, and 5, 10, and 15 in the SV-wave response) are the traveltimes in tens of milliseconds. The source is a vertical point source and receivers are horizontal (Figures 2.8a and 2.9a) and vertical (Figures 2.8b and 2.9b). It is evident from the figures that isotropic arrivals are always at the same time but this is not true for the anisotropic response because of the varying of velocity with angles. Also for horizontal receivers, a change in polarity is observed at the two sides from vertical propagation.

The radiation pattern for the S-wave (Figure 2.9) is more complicated compared to that of the P-wave (Figure 2.8). Between 30 and 60 degrees for the group angles, triplications (three arrivals) are observed in the S-wave propagation as shown in Figure 2.10. Therefore, S-waves are affected more than the P-wave in an anisotropic medium. This then requires more attention and care in seismic data analysis and interpretation.

33
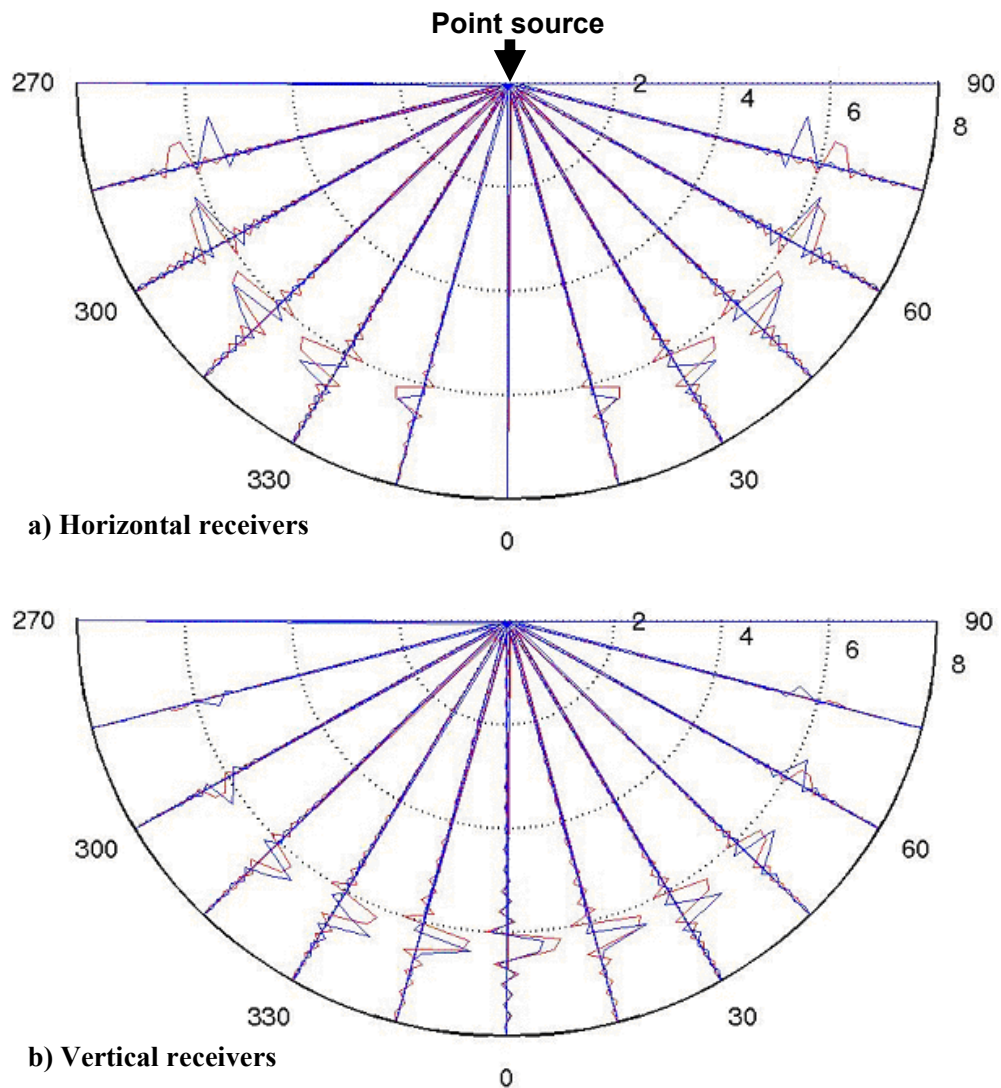
Figure 2.8. Radiation pattern of P-wave for a vertical point source and (a) horizontal receivers and (b) vertical receivers for a GRS model (Table 2.1) in the vertical plane: receivers are kept at the same distance from the source at different angles (semi-circle geometry). Isotropic and anisotropic arrivals are shown in red and blue color respectively. Isotropic arrivals are always at the same traveltime (distance) but anisotropic arrivals are varying according to the velocity variations. Note the polarity reversal at the two sides of source in the case of horizontal receivers.

34

Point source

a) Horizontal receivers

b) Vertical receivers
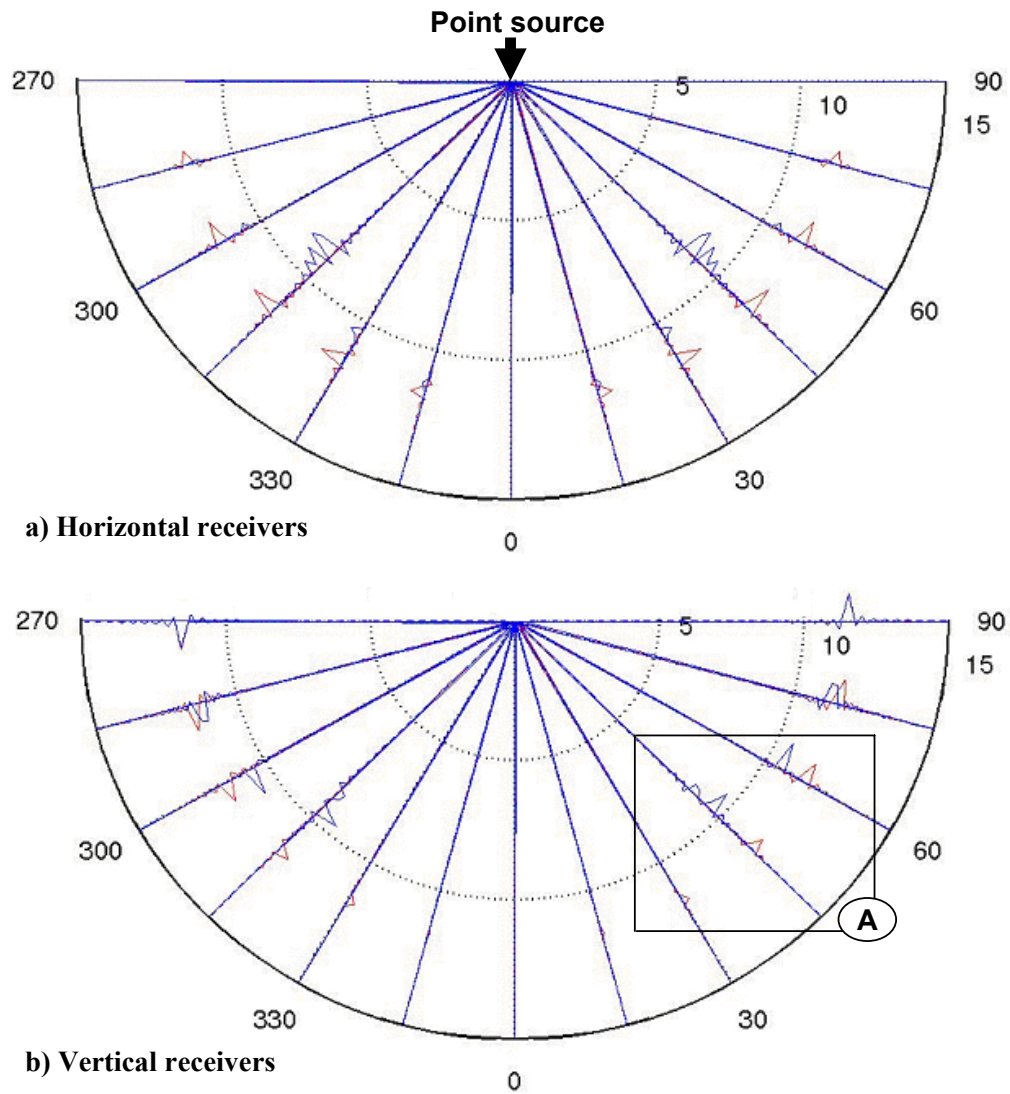
Figure 2.9. Radiation pattern of SV-wave for a vertical point source and (a) horizontal receivers and (b) vertical receivers for a GRS model (Table 2.1) in the vertical plane: receivers are kept at the same distance from the source at different angles (circle geometry). Isotropic and anisotropic arrivals are shown in red and blue color, respectively. Note multiple arrivals at certain angles as marked with a box (A) and discussed in detail in Figure (2.10).
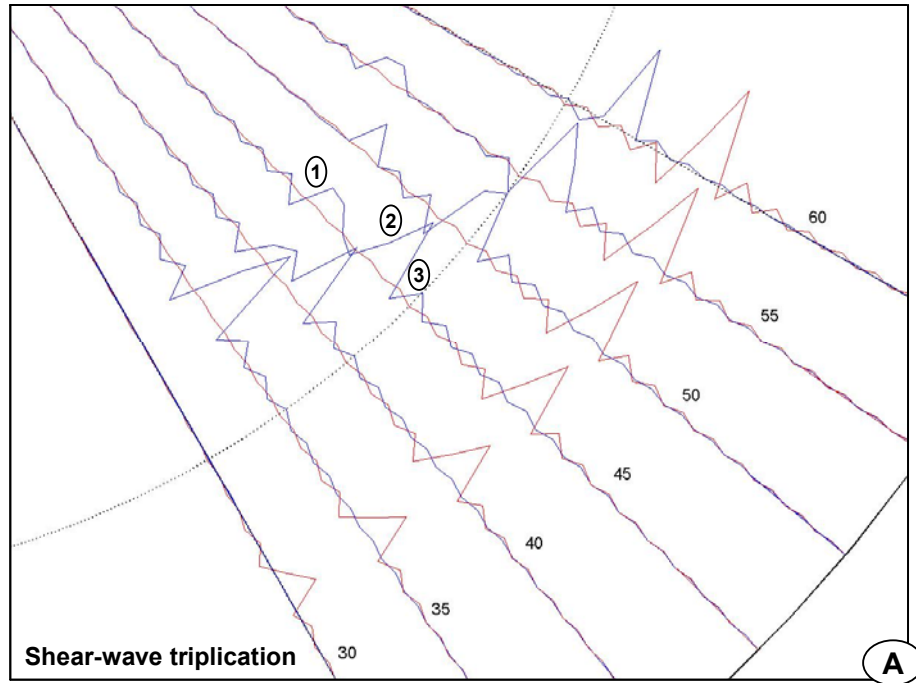
Figure 2.10. Shear-wave triplications (a zoom plot of the area (A) marked in Figure 2.9). There is only one arrival in isotropic case at the same time (in red) but multiple arrivals are observed in the anisotropic case (in blue). Three arrivals are marked for the 45^0 of wave propagation direction (group angle). Triplication response in the radiation pattern is the result of triplication in the group velocity surface (Figure 2.5a), which is caused by the fact that for a given phase angle three group angles are possible in the anisotropic media.

2.4 RAY-BORN APPROXIMATION

Rays are geometrical characteristics of a wave, and are defined as the normal to the wavefront (e.g., p.70, Lay and Wallace, 1995). In ray methods, Huygens's principle controls the geometry of a wave surface, where every point on a wavefront acts like a secondary wave and Fermat's principle governs the geometry of the ray paths in which a ray follows a stationary time path. This means that the rays bend during propagation and they may not see parts of a model creating shadow zones. Seismic ray theory is based on the asymptotic high frequency solution of the elastodynamic wave equation in the form of a ray series. Consider a time-harmonic solution of the elastodynamic wave equation for inhomogeneous media in a vectorial ray series (e.g., p.568, Červeny, 2001)

$$\vec{U}(x_j,t) = e^{i\omega T(x_j)} \sum_{n=0}^{\infty} \frac{1}{(-i\omega)^n} \vec{U}^{(n)}(x_j), \qquad (2.13)$$

where $\vec{U}^{(n)}(x_j)$ is vectorial amplitude coefficients of the ray series, which depend only on the coordinates x_j, and $T(x_j)$ is the eikonal or phase function. This equation has an asymptotic behavior as $\omega \to \infty$. The zeroth-order ray approximation of the ray series (2.13) is mostly used and is given by,

$$\vec{U}(x_j,t) = e^{i\omega T(x_j)} \vec{U}^{(0)}(x_j). \qquad (2.14)$$

Note the following limitations of this ray theory: 1) it is a high frequency approximation, 2) energy is traveling along the ray, and 3) diffractions (non geometrical phenomenon) and shadow zones are neglected.

The Born series solution of a differential equation can be written as (Rajan and Frisk, 1989),

$$U = U_0 + mU_1 + m^2U_2 + ---,$$ (2.15)

where U_0 is the solution in the reference medium, m is an ordering parameter, and U_1 and U_2 are the solutions for first- and second-order perturbations. This first order Born approximation gives a linear relationship between the perturbation and the change of the wavefield in terms of the reference medium, and is written as

$$U = U_0 + mU_1.$$ (2.16)

In this approximation (2.16), only the first order (single reflection) scattered wavefield is modeled; the mode conversions of waves are not included. The first order Born approximation is mostly used due to its simplicity, and is good for weak scattering (weakly heterogeneous) media only.

In the ray-Born approximation, the solution in the reference medium is given by ray theory (in the form of Green's function), and the Born approximation gives the scattering response. The resultant response is that the wavefield excited by a point source is propagated through the background medium, diffracted from each scattering (perturbation) point, and then propagated to the receiver.

2.4.1 RAY-BORN SOLUTION OF A WAVE EQUATION

The scattered wavefield in 3-D anisotropic medium after ray and Born approximations (equation C.8, appendix C) is given by the following multi-dimensional integral

$$U_{mn}(\mathbf{s},\mathbf{r},\omega) \approx \omega^2 \sum_{\Omega} \widetilde{g}_m(\mathbf{s})\hat{g}_n(\mathbf{r})\iiint R(\mathbf{\mu}_0,\widetilde{\mathbf{p}},\hat{\mathbf{p}},\widetilde{\mathbf{g}},\hat{\mathbf{g}})Ae^{i\omega t}\,dxdydz , \qquad (2.17)$$

where U_{mn} is the summation of all the single scattered wavefield, the tilde (~) and caret (^) superscripts are used to denote quantities associated with the incident and scattered wavefields respectively, A is an amplitude coefficient ($A = \tilde{A}\hat{A}$), t is traveltime ($t = \widetilde{t} + \hat{t}$), R is the scattering function, $\mathbf{\mu}_0$ represents a model-parameter vector (perturbations in terms of elastic stiffness and density), $\mathbf{p}$ is slowness vector, $\mathbf{g}$ is polarization vector, and Ω represents the summation over different wavetypes. Spatial dependence in the above equation (2.17) comes from polarization vectors, amplitude, and traveltime. The scattering function is written as (comparing equations 2.17 and C.8),

$$R(\mathbf{\mu}_0,\widetilde{\mathbf{p}},\hat{\mathbf{p}},\widetilde{\mathbf{g}},\hat{\mathbf{g}}) \equiv \left(\Delta\rho\delta_{ik} + \Delta c_{ijkl}\widetilde{p}_l\hat{p}_j\right)\widetilde{g}_k\hat{g}_i , \qquad (2.18)$$

and the amplitude coefficient in a homogeneous background medium is given by

$$A = \frac{1}{4\pi V |r-s|\sqrt{K}} , \qquad (2.19)$$

where K is Gaussian curvature of the slowness surface, and V is group velocity.

39

2.5 ALGORITHM

The seismic response due to a reflector, for the given acquisition parameters (e.g., source and receiver positions and orientation) and an earth model, can be calculated by assuming the reflector to be made of point diffractors, where each point on a reflector sends energy towards all the receivers (Trorey, 1970). For each point on the reflector in a subsurface model, I calculate slowness, group velocity, polarization, and traveltime (from source to subsurface point and then to receivers). Typically the offsets (and group angles) are known from the source to the subsurface point and then to the receiver. Here I describe an algorithm starting with offset information (say, x_s and x_r are the source and the receiver horizontal distances from a subsurface point). The steps for generating a synthetic seismogram in anisotropic media are given below.

1. make a table of offset x (x_s / x_r) and phase angle for a unit depth ($z = 1$),

   i) calculate horizontal slowness (p) and vertical slowness (q) for phase angles

     (see appendix A)

   ii) evaluate $\dfrac{dq}{dp}$ using a finite difference scheme, $\dfrac{dq}{dp} = \dfrac{q(n) - q(n-1)}{p(n) - p(n-1)}$

   iii) calculate the offset, $x = -\dfrac{d\tau}{dp} = -z\dfrac{dq}{dp} = -\dfrac{dq}{dp}$, where τ is the intercept time

     and z is the depth of subsurface point (here, $z = 1$).

2. find the phase angle (and then p) for a given offset x (using step 1),

3. calculate traveltime using the following equation,

$$t = (\tau + px)_{inc} + (\tau + px)_{ref} = (zq + px_s)_{inc} + (zq + px_r)_{ref} \qquad (2.20)$$

40

where subscripts *inc* and *ref* refer to the incident and reflected wave response.

4) calculate amplitude (equation 2.19), and polarization vector (section 2.4) for the source and receiver side,

5) evaluate the scattered wavefield response (equation 2.17) using the scattering function given by equation (2.18). For a VTI medium, the scattering function is given by the following expression

$$R = [\Delta\rho + \Delta c_{11}\tilde{p}_1\hat{p}_1 + \Delta c_{44}\tilde{p}_3\hat{p}_1]\tilde{g}_1\hat{g}_1 + [\Delta c_{13}\tilde{p}_1\hat{p}_3 + \Delta c_{44}\tilde{p}_3\hat{p}_1]\tilde{g}_1\hat{g}_3$$

$$+ [\Delta\rho + \Delta c_{44}\tilde{p}_1\hat{p}_1 + \Delta c_{33}\tilde{p}_3\hat{p}_3]\tilde{g}_3\hat{g}_3 + [\Delta c_{13}\tilde{p}_3\hat{p}_1 + \Delta c_{44}\tilde{p}_1\hat{p}_3]\tilde{g}_3\hat{g}_1 \qquad (2.21)$$

where **p** and **g** are the slowness and polarization vectors, respectively, and the symbol Δ shows the perturbation values from the background medium.

6) convolve the result from step 5 with a wavelet.

Determination of the phase angle and offset relation (step 1) is not trivial in strongly anisotropic media, especially for S-waves, as there may be multiple values of phase angles for a given offset x. Figure 2.11a shows the offset and phase angle curve for qS1-wave for a GRS model (a VTI model). The offset is related to the group angle (Figure 2.11b). This will result in multiple arrivals (triplications) for those ranges of offsets or angles (see Figures 2.5 and 2.10). In the following section, I will show two model examples: 1) a flat reflector, and 2) a basin model, where the background medium I used is a homogeneous GRS and the perturbation to the background which forms the inhomogeneous model (e.g., the reflector) I used the properties of Berea sandstone (Table 2.1).

41
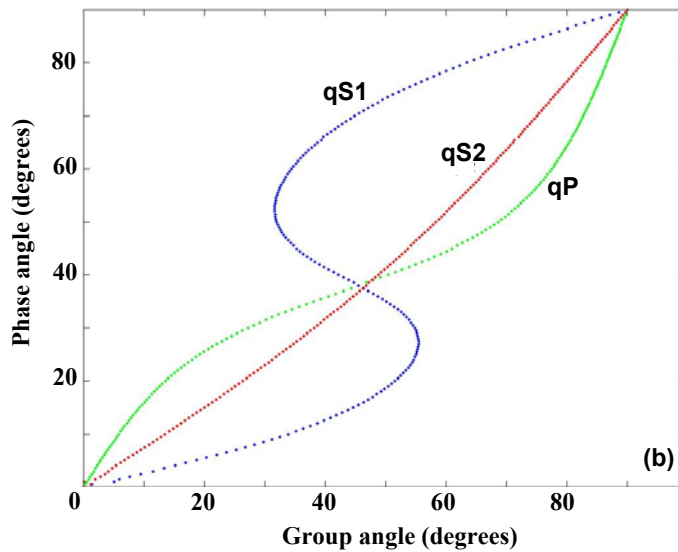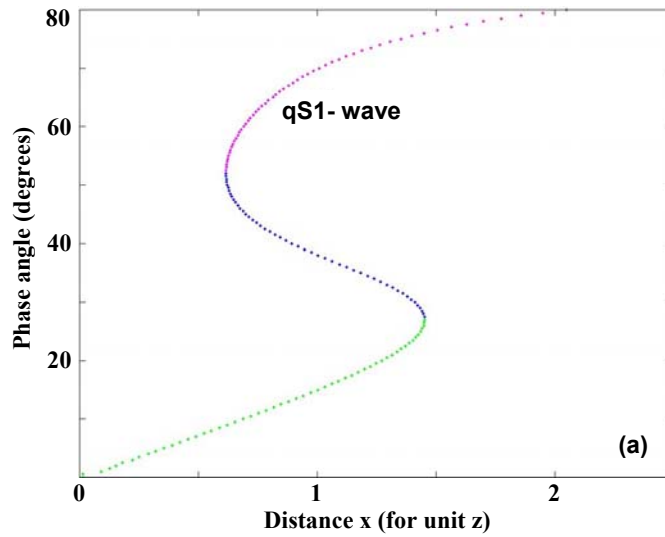
Figure 2.11. For a Green River Shale model, a) shows offset and phase angle relation for SV-wave (qS1-wave) and b) shows the group angle and phase angle relation for three waves. For some range of offsets, three phase angles are possible for SV-wave, and these result in triplication in shear-wave response.

2.6 EXAMPLES

Flat layer model

Consider a flat interface (reflector) at a depth of 300m below the source-receiver level (Figure 2.12). The source is on the left of model and the receivers are placed in a line from left to the right (end-on geometry). The background medium is a Green River Shale and the perturbation (reflector) is the Berea sandstone. Both are of type VTI anisotropy. Synthetic seismograms have been generated using the algorithms given in the previous section. Figure 2.13 shows the P- and SV-wave synthetic seismograms using the ray-Born method. Triplication is observed in the SV-wave response as expected in the middle range of the angle of wave propagation which follows from Figure 2.11. This triplication is caused by the wave propagation in the background medium and not the perturbations.
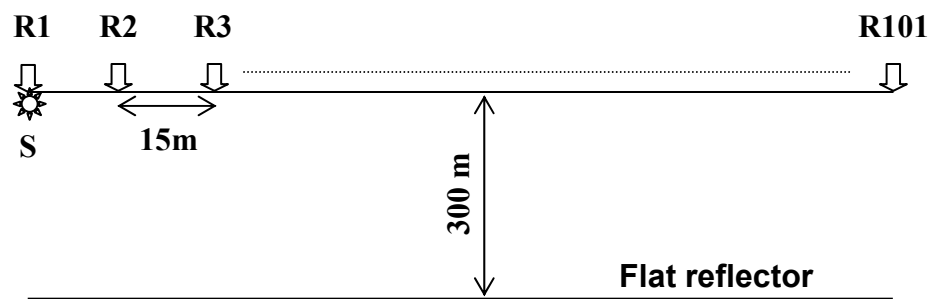
Figure 2.12. A flat layer model with end-on survey geometry: the receivers (R) spacing is 15m and the shot (S) is placed on the left of the model. The reflector can be assumed to be made of many point diffractors and then the seismic response can be estimated by summing the scattering response from all the points on subsurface reflector.

43
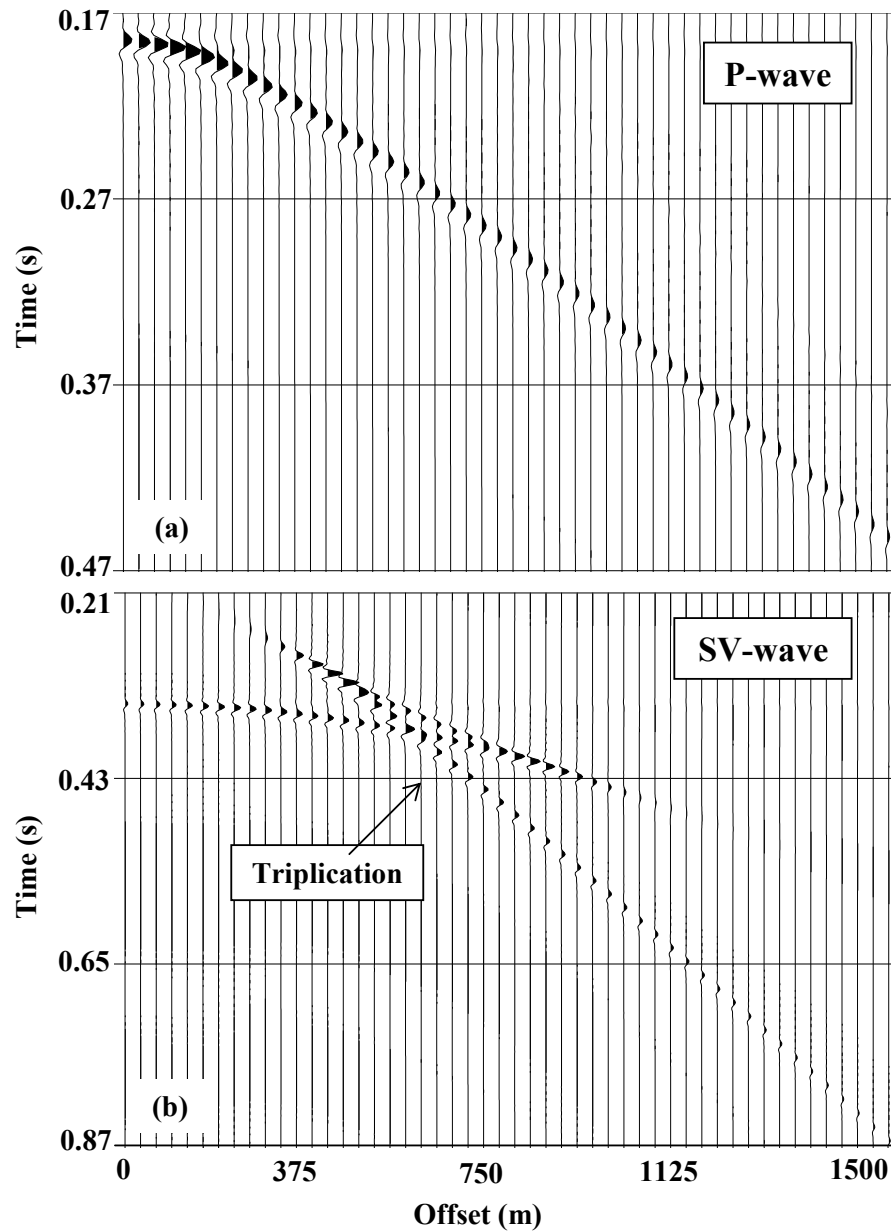
Figure 2.13. P-wave (a) and SV-wave (b) seismograms for a flat layer model (Figure 2.12) with vertical point source placed at left of the model (source and receivers are on the surface). Polarization is not considered to highlight the triplication response.

44

Basin model

Consider a basin model (Figure 2.14), where the shape of basin is given by

$$z(x) = z_0 + \frac{D}{2}\left[1 - \cos\{2\pi(x - \frac{w}{2})/w\}\right],$$
(2.22)

where x is offset, z_0 is the thickness of overburden, D is the maximum depth of basin below overburden, and w is the width of the basin (2000m). The source is placed at the middle of the model and the receivers are located on both sides of the source (split-spread geometry). I consider point diffractors along the basin interface at every 10m of offset (equation 2.22), and sum the scattered wavefield due to all points. Figure 2.15 shows the P- and SV-wave synthetic seismograms for a vertical point source and vertical receivers. Triplications are possible due to the basin geometry and also due to the triplication in the group velocity surface.
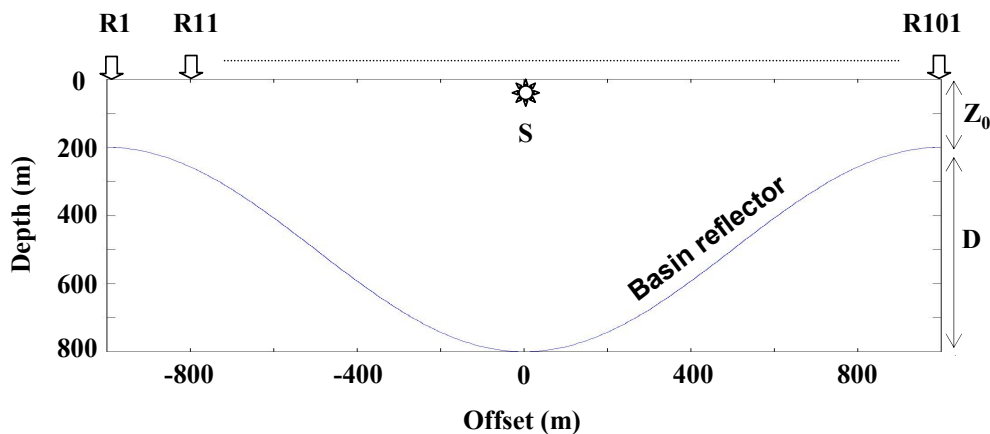
Figure 2.14. A basin model with split-spread survey geometry. The receivers (R) spacing is 20m and the shot (S) is placed on the center of the model.
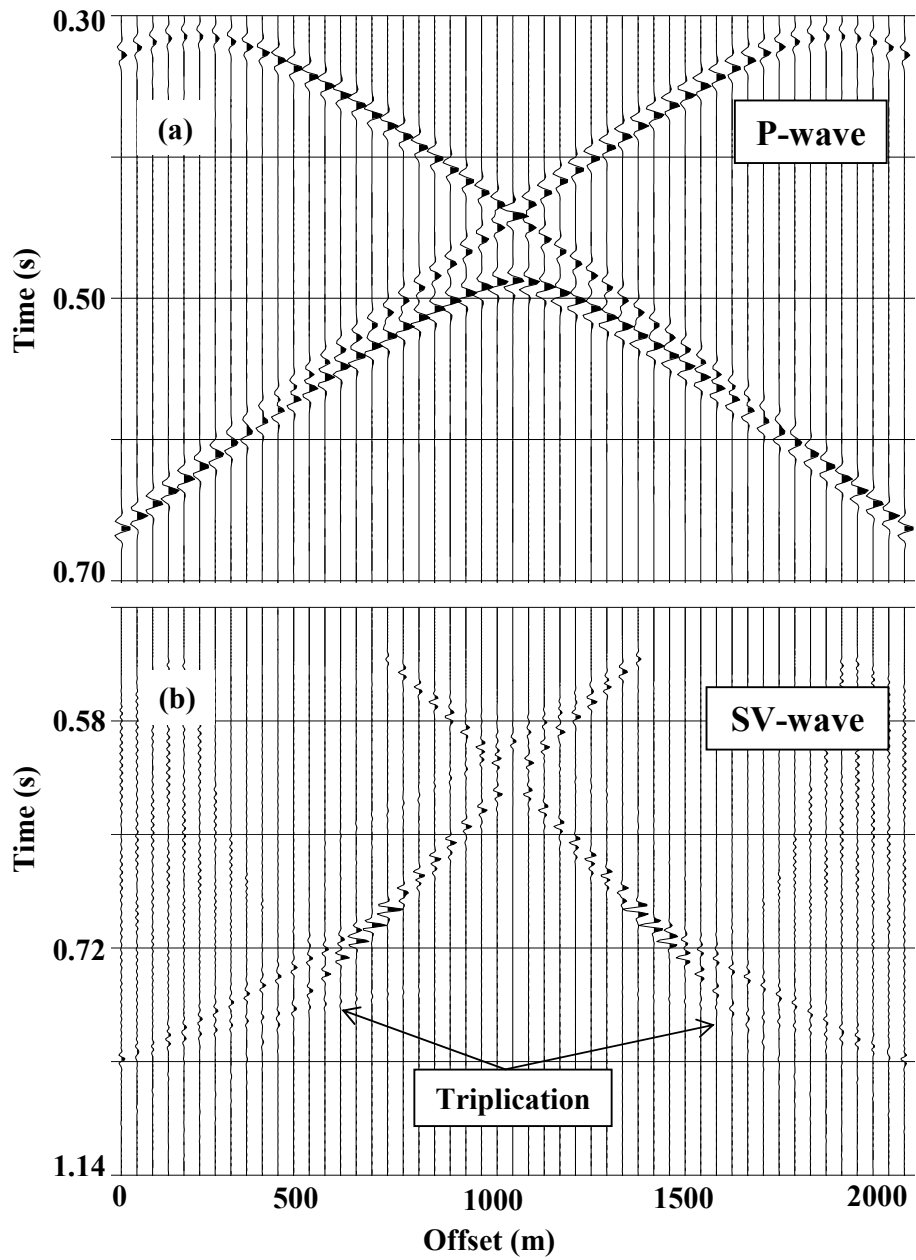
Figure 2.15. P-wave (a) and SV-wave (b) synthetic seismograms for the basin model (Figure 2.14) with vertical point source placed in middle of the model and vertical receivers (source and receivers are on the surface). Triplication in the P-wave seismogram is due to the shape of the reflector.

46

2.7 SUMMARY

Calculation of synthetic seismograms with a focus on the ray-Born method has been discussed in this chapter. The ray-Born method is one of the asymptotic methods used to generate seismograms in heterogeneous and anisotropic media. It models the subsurface as a background medium and a perturbation, in which, the wave propagation in the background medium is approximated with ray theory and the Born approximation gives the scattered wavefield due to the perturbation (heterogeneity) with respect to the background medium. I used a first-order Born approximation which is simple to implement but gives only the single-scattering response. However, this method can model S-wave triplications in anisotropic media and works well in many geologic setting where heterogeneity and changes in the wavefield (due to perturbations) can be linearly represented in terms of a background medium. The background medium can indeed be heterogeneous and anisotropic. However, the choice of such a background medium may not always be straightforward. Ray-Born modeling is widely used due to its simplicity but the approximations are valid only for weakly heterogeneous media. In a strongly heterogeneous and anisotropic medium, synthetic seismograms can only be generated if the traveltime and amplitude of the seismic waves propagating through the medium can be determined.

Chapter 3: Traveltime calculation and prestack depth migration in TTI media

3.1 INTRODUCTION

Migration is an imaging procedure that takes seismic wavefields recorded at the surface as the input data and calculates the locations and strengths of the reflectors in the subsurface. Kirchhoff based migration is the most widely used method for seismic imaging because of its simplicity. It involves calculating source and receiver traveltimes to each point in a subsurface model, and the Kirchhoff integral (Schneider, 1978) is used to obtain the migrated images. The speed and accuracy of this method depends on the traveltime computation which is usually achieved by ray-tracing or finite-difference methods.

Ray-tracing methods (Červený, 2001) are general in that multipathing of rays can be included easily. However, such methods are sometimes difficult to use in practice, for example, in shadow zones. Further, once the rays and traveltimes have been computed, interpolation to a uniform grid is required, which can introduce error. The problem of finding ray-paths between a source and/or a receiver location and a subsurface gridpoint can be solved by two-point ray tracing, for which there are two main approaches: shooting (Bulant, 1999) and bending (Um and Thurber, 1987). The shooting method is formulated as an initial value problem, where a ray path is given an initial take-off angle and a starting position, and then it incrementally traces a ray through the velocity model. Ray bending is formulated as a boundary value problem, where the source and

receiver locations are specified, an initial guess of the ray path is constructed, and the algorithm iteratively perturbs the ray path until convergence based on a minimum time criterion is reached. Another family of ray calculation techniques is ray field propagation in which the entire wavefield for a given mode (P- or S-wave in isotropic media; qP-, qSV-, or qSH-wave in TI media) is propagated rather than individual rays (Vinje et al., 1993).

Finite-difference methods of traveltime calculation (Vidale, 1988, 1990; van Trier and Symes, 1991; Lecomte, 1993; Dellinger and Symes, 1997; Sethian and Popovici, 1999, Alkhalifah, 2002; Qian and Symes, 2002) attempt to overcome some of the problems associated with the ray-based methods. Based on the finite-difference solution of the Eikonal equation, these methods provide first arrival traveltimes for each gridpoint. However, they tend to be restricted to moderate velocity contrasts. Podvin and Lecomte (1991) proposed an algorithm that can handle strong velocity contrasts, but is inaccurate in regions where plane waves are not good approximations for wavefronts. Eikonal solvers are fast and robust for simple geologic models but many of these algorithms fail to give accurate traveltimes in media with strong velocity contrasts (Vidale, 1988).

Because of the problems associated with ray-based and finite-difference methods, direct calculation of traveltime is becoming popular. Schneider, Jr. et al. (1992) proposed a robust method based on Fermat's principle for traveltime calculation in isotropic media that implements a local ray-trace solution of the Eikonal equation. The traveltime at each grid point is calculated eight times and

49

the minimum time is retained. The method is highly robust though it computes first-arrivals only.

Many common imaging algorithms assume an isotropic earth model. Seismic imaging based on an isotropic medium can result in, a) mis-tie of seismic data with well-log data (Banik, 1984), b) poor quality of seismic images (due to incoherent stacking as NMO is not perfect even for isotropic media), and c) mis-positioning of the exploration targets (Isaac and Lawton, 1999). For improving images, the imaging algorithms should be modified to include the effects of anisotropy whenever anisotropy is present.

Various authors (Sena and Toksöz, 1993; Le Rousseau, 1997; Alkhalifah, 1995) have demonstrated different imaging methods in TI media. These methods assume either weak lateral heterogeneity, or weak anisotropy (Thomsen, 1986). For Kirchhoff based migration in TI media, traveltime is an important task which requires group velocity estimation in anisotropic media. Faria and Stoffa (1994) modified the Schneider, Jr. et al. (1992) method of traveltime calculation to include transverse isotropy with a vertical symmetry axis.

When elastic boundaries in the subsurface are dipping, the symmetry axis of the TI may be non-vertical. Such media are often referred to as TI with a tilted axis of symmetry (TTI). They can be found in regions with anticlinal structures and/or thrust sheets. Imaging below tilted TI media has been reported by Isaac and Lawton (1999), and Vestrum et al., (1999). They assumed weak anisotropy to simplify the calculation. Ferguson and Margrave (2002) proposed a depth imaging method in dipping TI media using a symmetric non-stationary phase shift

migration method, in which anisotropic velocity is approximated by polynomial curve fitting with about twenty coefficients. This method also assumes weak lateral heterogeneity.

In this chapter I discuss the development of a technique for traveltime computation in tilted TI media based on a direct method. The approach is an extension of the algorithm of Faria and Stoffa (1994) that allows for the tilt angle and the anisotropy parameters to vary spatially. I used a simple approximate method for the group velocity calculation in tilted TI media and then used it in the traveltime computation. I use the traveltime tables calculated with this technique in a 2D prestack Kirchhoff depth migration of a physical model data set and compare my results with those obtained by a recursive extrapolation method.

3.2 TRAVELTIME CALCULATION

3.2.1 Direct method of traveltime calculations

Schneider, Jr. et al. (1992) used a simple calculus based technique to compute traveltime and made no assumption on velocity smoothness. The traveltime computation begins with the starting values computed near a source location. The mapping systematically steps through the grid, where each new traveltime is calculated using two previously computed neighbor traveltimes. After eight calculations at each grid point, the minimum time is assigned to the grid. At any stage during the mapping, only the most recently computed traveltime is used to calculate new traveltimes. Schneider, Jr. et al. (1992) proposed two mapping procedures, a brute force approach that advances across

the grid one column (or row) at a time and a more natural approach that computes times along expanding rectangles.

The first approach of Schneider, Jr. et al. (1992) is the easiest to program; since the brute force scheme is model-independent, it is more robust because it can handle more complicated velocity distributions. The second approach, however, is model-dependent similar to that of Vidale (1988), but considers both linear (plane-wave) and nonlinear (point-source) interpolation of traveltimes. The nonlinear approach requires group velocities for traveltime computation.

Faria and Stoffa (1994) used the nonlinear brute-force approach of Schneider, Jr. et al. (1992) for traveltime calculation in VTI media. For fast computation they vectorized the program, which makes the order of calculation different from Schneider's, requiring one additional traveltime mapping step (total nine). They considered a Fourier based cosine expansion for anisotropic group velocity estimation following Byun et al. (1989).

As described in Schneider, Jr. et al (1992) and Faria and Stoffa (1994), two known traveltimes t_1 and t_2 are used to compute the traveltime at a third grid point (Figure 3.1a). In appendix D, I summarize this approach, and describe its extension to tilted TI media. The resulting expression computes a group angle corresponding approximately to the minimum traveltime from the source to the point of interest as a function of t_1 and t_2. For a given point of interest, eight traveltimes can be computed based on the eight grid points surrounding the point of interest (Figure 3.1b). The minimum of these eight evaluations provides the first-arrival traveltime from the source to the point through all possible paths.
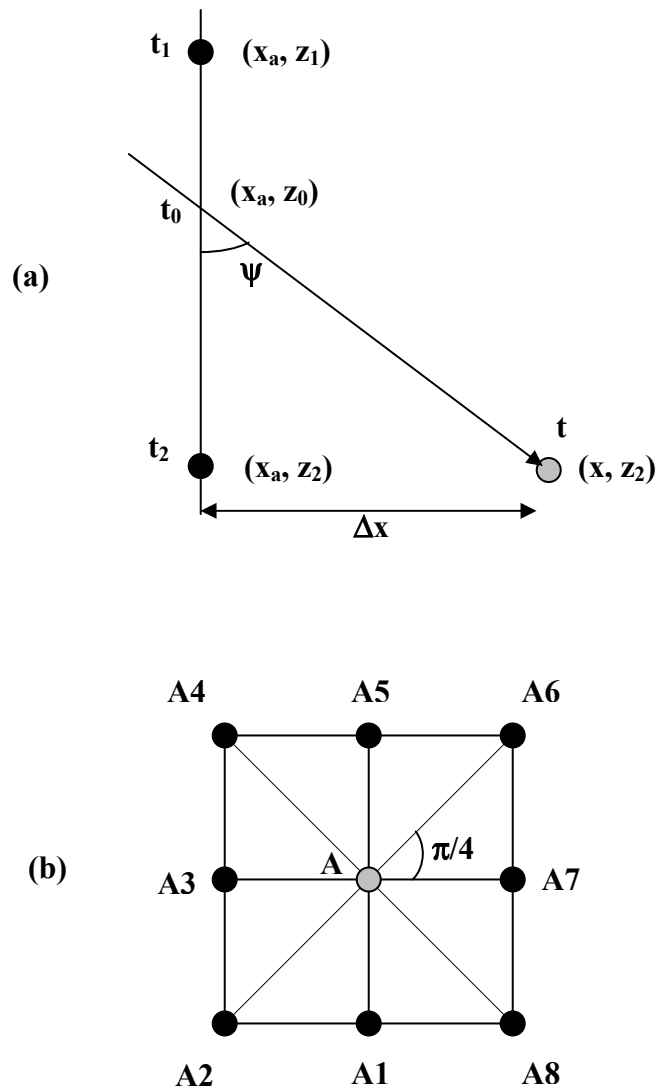
Figure 3.1. (a) Single traveltime calculation scheme, and (b) possible angles of wave propagation.

From appendix D, the traveltime t, at a point (x, z_2) in the subsurface (Figure 3.1a) is given by equation (D-6), i.e.,

$$t = t_0 + s(\phi)\Delta x \, \text{cosec}(\Psi), \tag{3.1}$$

where Ψ is the angle between a ray and the line connecting two neighboring points (Figure 3.1a), ϕ is the angle between a ray and the vertical axis (group angle), Δx is the grid spacing in x, t_0 is the known traveltime to a point adjacent to the point of interest, and $s(\phi)$ is the group slowness (inverse of group velocity). This traveltime equation (3.1) is approximate in the sense that an average slowness is used to compute the traveltime from the source location to the grid. Equation (3.1) is used to find the minimum traveltime t using Fermat's principle. To calculate the minimum traveltime, I equate the first derivative of t with respect to angle Ψ to be zero [equation (D-7)] and find the appropriate angle Ψ. To calculate t and its derivatives, anisotropic group velocity at angle ϕ need to be evaluated.

Angle Ψ can vary from 0 to 90 degrees in each individual calculation, and there are eight possible values of the group angle ϕ. The angle Ψ differs from ϕ by a constant, $\phi = k\dfrac{\pi}{4} + \Psi$, where k assumes a value from 0 to 7 depending on the quadrant in which it is being evaluated (Figure 3.1). The relation between ϕ and Ψ has been discussed in traveltime mapping scheme (section, 3.2.3).

54

3.2.2 Group velocity estimation in TTI media

In appendix D, for the traveltime calculation in TI with a tilted axis of symmetry, I modify the traveltime algorithm for estimating anisotropic group velocity. For anisotropic group velocity estimation, I implemented two methods; an exact method and an approximate method based on a cosine Fourier series. The exact method gives an analytic expression for the group velocity (Appendix B) and is valid for a general anisotropic medium; it is based on the anisotropic ray-tracing system described in Červený (1972). At each grid point, I generate the elastic coefficient matrix for a TTI medium by applying the Bond transformation (Auld, 1990) to the elastic coefficient matrix for the corresponding VTI media and then use Červený's formulation to compute group velocities.

The exact formulation of the anisotropic group velocity is not simple to implement, and the exact derivatives of the group velocity (required to find the minimum traveltime) with respect to the group angle (ϕ) need to be evaluated numerically (Červený, 2001). Therefore, here I prefer the approximate method for anisotropic group velocity calculation.

My approximate method is based on a series approximation of the quasi-P wave group velocities. Recall that the group velocity in VTI media can be approximated by a truncated Fourier-type cosine series (Byun et al., 1989) as,

$$v_g^{-2}(\phi) = a_1 + a_2 \cos^2 \phi - a_3 \cos^4 \phi, \tag{3.2}$$

where, the coefficients a_1, a_2, and a_3 are functions of the elastic parameters of the medium, and $v_g(\phi)$ is the P-wave group velocity at an angle ϕ. For a VTI

55

medium, a_1, a_2, and a_3 can be calculated simply by setting, $v_g(0)$, $v_g(90)$, and $v_g(45)$ in equation (3.2) as,

$$a_1 = \frac{1}{\alpha_0^2(1+2\varepsilon)},$$

$$a_3 = \frac{4}{v_g^2(45)} - 2a_1 - \frac{2}{\alpha_0^2}, \qquad (3.3)$$

$$a_2 = \frac{1}{\alpha_0^2} + a_3 - a_1,$$

where, α_0 is the vertical P-wave velocity, ε is the anisotropic parameter (Thomsen parameter), and $v_g(0)$, $v_g(90)$, and $v_g(45)$ are the group velocities at the corresponding group angles. In an isotropic medium, the coefficients reduce to $a_1 = 1/\alpha_0^2$, $a_3 = a_2 = 0$, In VTI media, horizontal and vertical group velocities are the same as the horizontal and vertical phase velocities respectively; $v_g(90)$ is evaluated using Thomsen's formulation for phase velocity (Thomsen, 1986). For $v_g(45)$, I first calculate the corresponding phase angle [equation (22a), Thomsen, 1986] and phase velocity [equation (16a), Thomsen, 1986] and then group velocity ($\mathbf{v}_g = \frac{\widehat{n}}{\mathbf{p}.\widehat{n}}$, where $\mathbf{v}_g$ is the group velocity vector, $\mathbf{p}$ is the slowness vector, and $\widehat{n}$ is the unit vector normal to the slowness surface). The advantage of this formulation [equation (3.2)] is that the coefficients a_1, a_2, and a_3 are calculated once for a VTI medium, and then it becomes easy to evaluate group velocity for a homogeneous TI medium. If the TI parameters change at grid points then coefficients a_1, a_2, and a_3 need to be re-calculated.

I evaluate the effectiveness of my approximate group velocity equation by comparing the numerically computed group velocities with those computed with the exact values for three different models: (1) a strong VTI (nearly elliptic) model (α_0 = 2870 m/s, β_0 = 1570 m/s, δ = 0.204, and ε = 0.223), (2) a VTI model with (α_0 = 2870 m/s, β_0 = 1570 m/s, δ = -0.204, and ε = 0.223), and (3) the Dog Creek Shale model (α_0 = 1875 m/s, β_0 = 826 m/s, δ = 0.1, and ε = 0.225; data from Thomsen, 1986). The comparison of the group velocity curves for the three models are displayed in Figures 3.2a, 3.2b and 3.2c respectively. Note the acceptable fits between the exact and approximate group velocity curves.

For the quasi-P wave group velocity calculation in TTI media, I make a simple modifications to equation (3.2) given by,

$$v_g^{-2}(\phi) = a_1 + a_2 \cos^2(\phi - \theta) - a_3 \cos^4(\phi - \theta),$$

(3.4)

where ϕ is the group angle, and θ is the rotation of the axis of symmetry with respect to the vertical (tilt angle of TTI). In equation (3.4), θ is positive if the rotation of the symmetry is anti-clockwise from the vertical, else θ is negative.

To demonstrate this method, I used the three TI models as in the previous example in which I introduce a tilt in the symmetry axis by $+30^0$ from the vertical. For all three TTI models, the comparison between exact and approximate group velocities is shown in Figures 3.2(a) through 3.2(c). Notice a good agreement between the two curves for all three models. Equation (3.4) is used for the evaluation of angle-dependent P-wave group velocities in all the examples shown in this chapter.
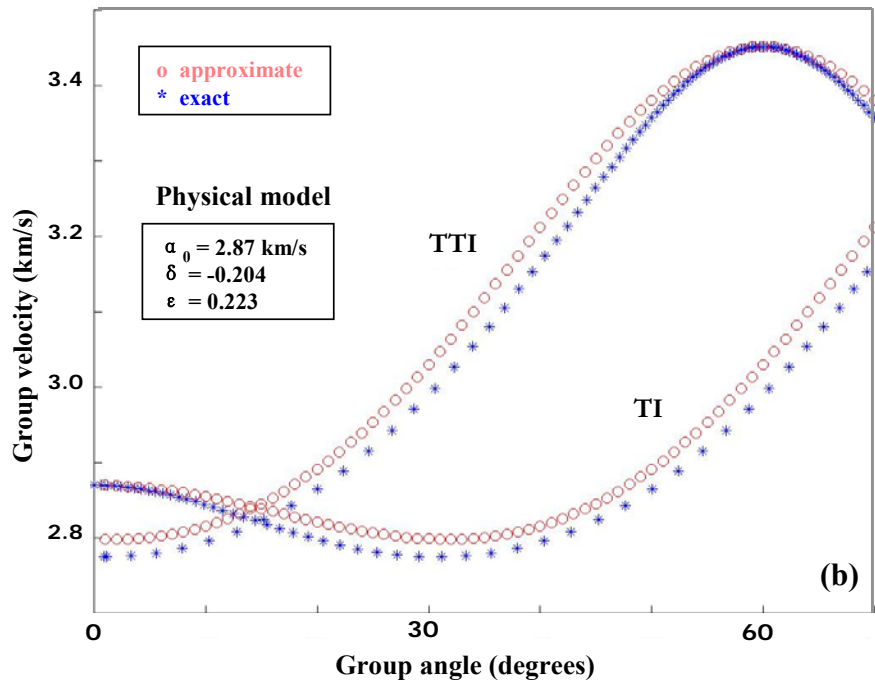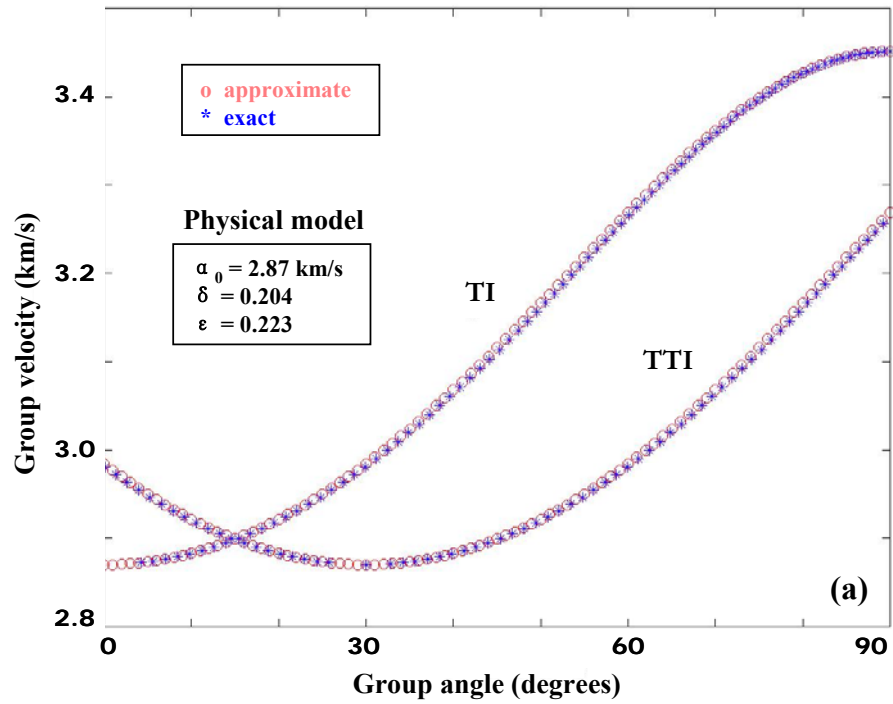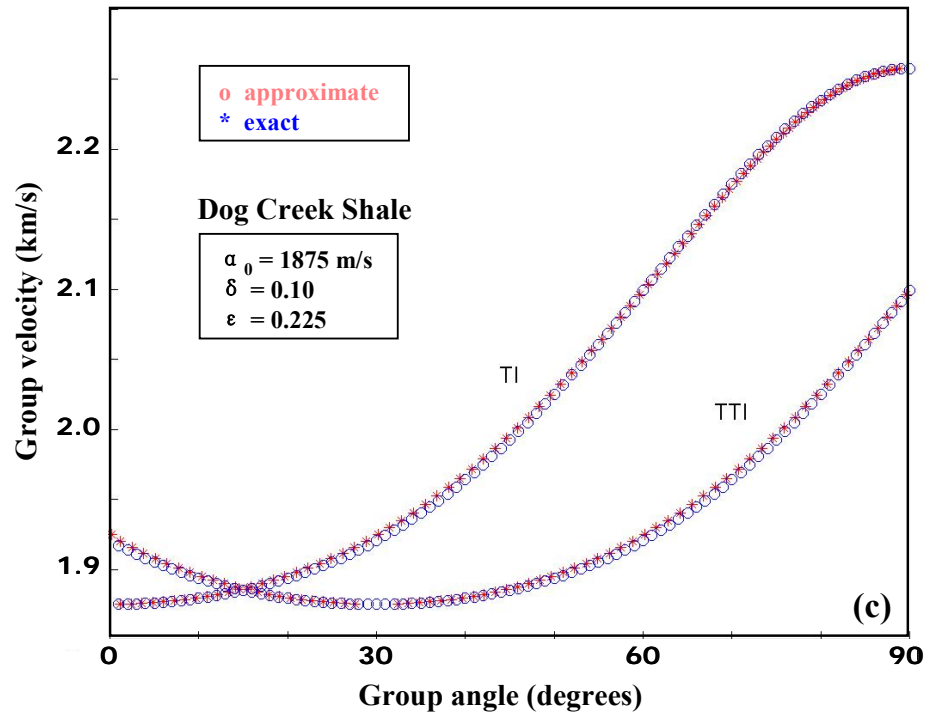
Figure 3.2. Comparison of group velocities in TI and TTI (TI with the axis of symmetry rotated by 30 degrees anti-clockwise) media computed with true and approximate method (equations 3.2 and 3.4): (a) for physical model, (b) for physical model with sign of δ reversed, and (c) for a Dog Creek Shale. The circles correspond to the approximate values and the asterisks represent exact values. Approximate curve follows closely with the exact curve of velocity. In Figure 2b, a little deviation is observed, but this is not a commonly observed anisotropy in sedimentary rocks.

3.2.3 Traveltime mapping scheme

Using the "brute force mapping" described in Faria and Stoffa (1994), I calculate traveltimes at all the grid points of the source column (grid column containing the source grid) using the vertical P-wave velocity, and at the six source neighboring points (A2, A3, A4 and A6, A7, A8 in Figure 3.1b) in the adjacent columns using straight ray paths from the source. This is the initial condition. Now, the traveltimes for points on the left side of the source are calculated column-by-column (Figure 3.3a) until the left edge of the grid is reached. Similarly for points on the right side of the source (Figure 3.3b), traveltimes are calculated until the right edge of the grid is reached. Apart from the initial condition, traveltimes at all other grid points are calculated by minimizing equation (D-6) (Appendix D). Of course, it is not guaranteed that the first-arrival traveltime is correct so a second process is initiated. In the second part, traveltimes are calculated using the schemes shown in Figures 3.3c and 3.3d. The traveltimes are calculated from left to right and from right to left for each grid point away from the source column, moving from the source level to the bottom of the model (Figure 3.3c) and from the source level to the top of the model (Figure 3.3d). After mapping all the grid points, the least traveltime (out of eight) for each grid point is selected and written to the output traveltime grid.

Figure 3.4 shows P-wave traveltime contours for the model used in Figure 3.2(a), using my traveltime computation approach for TI and TTI medium for a source placed at the center of the model (1000 m by 1000 m). The effect of the tilt of the symmetry axis is pronounced in Figure 3.4b.

60

$\phi = \psi + \theta$ t_1 ψ t t_2

t_1 $\phi = \psi - \theta$ ψ t_2 t

(a)   **(b)**

t t_2 ψ $\phi = \psi - \theta$ t_1

t_2 t ψ t_1 $\phi = \psi + \theta$
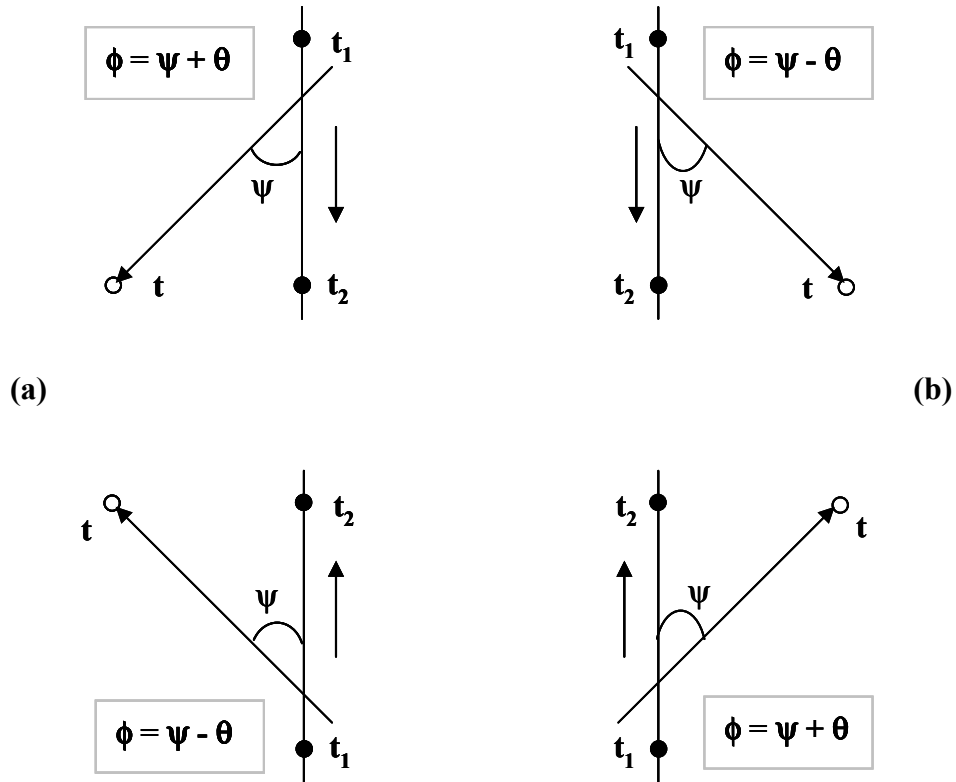
Figure 3.3 (a, b). Traveltime mapping scheme: traveltimes for grid points on the left side of the source (a) and on the right side of the source (b) are calculated column-by-column until the left and right edge of the grid, correspondingly, are reached.

(c)

$$\phi = \pi/2 - \psi - \theta$$

$$\phi = \pi/2 - \psi + \theta$$

(d)

$$\phi = \pi/2 - \psi + \theta$$

$$\phi = \pi/2 - \psi - \theta$$
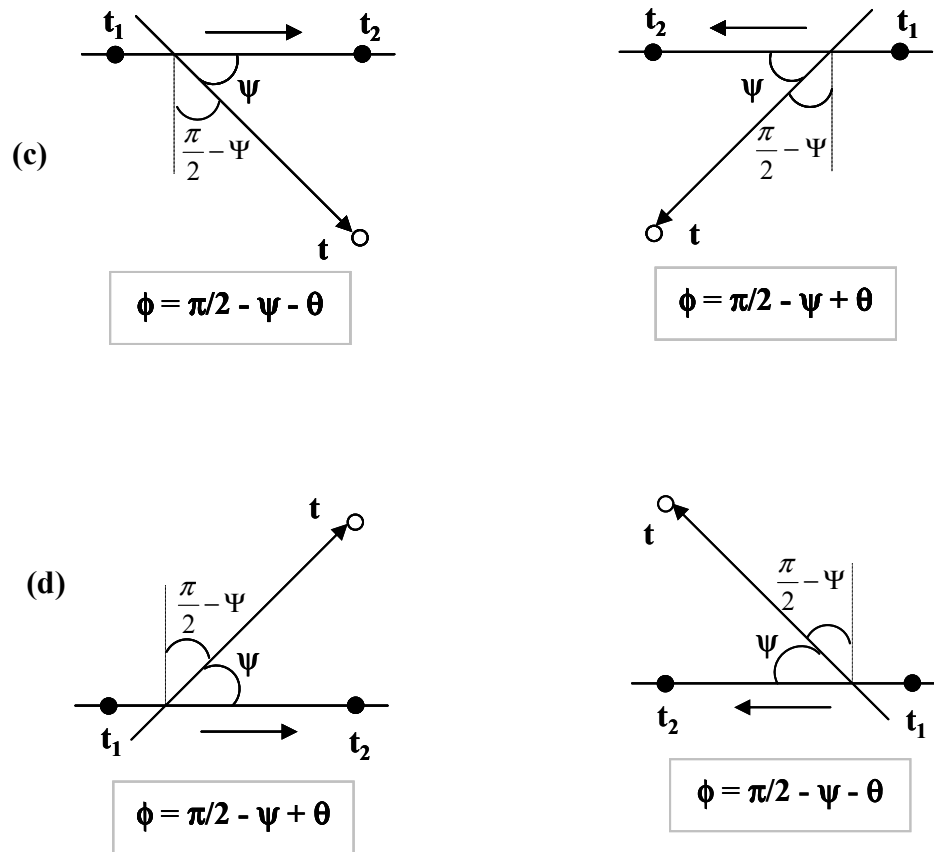
Figure 3.3 (c, d). Traveltime mapping scheme: from left to right and right to left away from the source column, moving from the source level to the bottom of the grid (c) and from the source level to the top of the grid (after Faria and Stoffa, 1994).

62
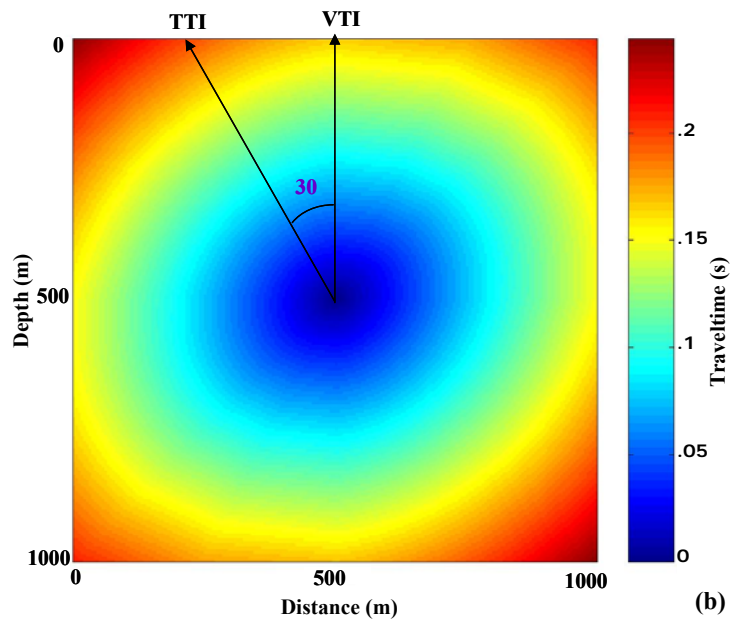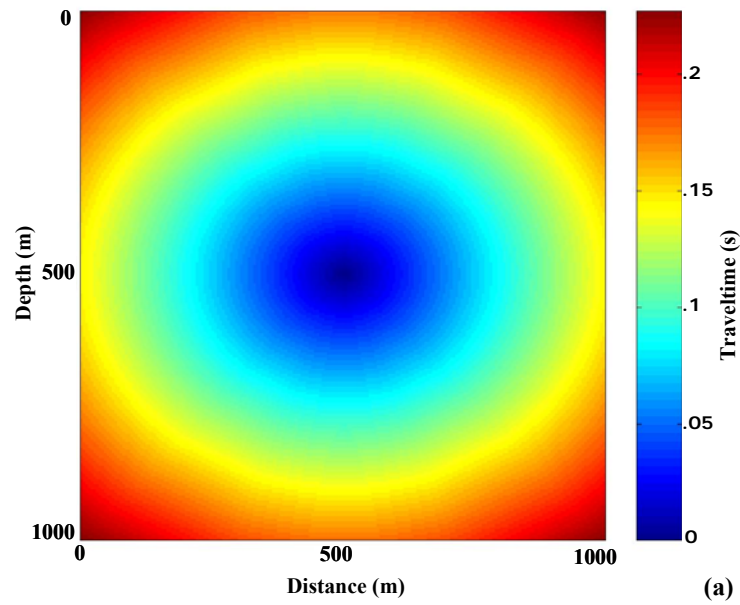
Figure 3.4. P-wave traveltime contours in a homogeneous medium (Table 2.1) with (a) TI and (b) TTI type of anisotropy. A point source is placed at the center of the model.

3.2.4 Extension to S-wave traveltime calculation in VTI media

The S-wave group velocity in VTI media (in the vertical plane of wave propagation) can be approximated by a truncated Fourier-type cosine series, similar to equation (3.2) for the P-wave as,

$$v_S^{-2}(\phi) = a_1 + a_2 \cos^2 \phi - a_3 \cos^4 \phi, \tag{3.5}$$

where $v_S(\phi)$ is the S-wave group velocity at an group angle ϕ, and a_1, a_2, and a_3 are the coefficients given as,

$$a_1 = \frac{1}{\beta_0^2},$$

$$a_2 = a_3 = 4\left(\frac{1}{v_S^2(45)} - a_1\right). \tag{3.6}$$

$v_S(45)$ is the S-wave group velocity at 45^0 of group angles, which can be calculated approximately (e.g., equation SV2, Fowler, 2003). Figures 3.5 and 3.6 compare the S-wave group velocity and S-wave traveltime contours, respectively, in Green River Shale (GRS) and a physical model (Table 2.1). Note the acceptable fit between exact and approximate S-wave group velocities, except near the 45^0 angle where S-wave exhibits triplication (Figure 3.5a). Note also that this method does not model the triplications. Anisotropic S-wave group velocity depends on the difference in the anisotropic parameters (ε-δ). For many models, this difference is small, and that's why the velocity variation is very smooth and weak, as can be seen in Figures 3.5b and 3.6b.
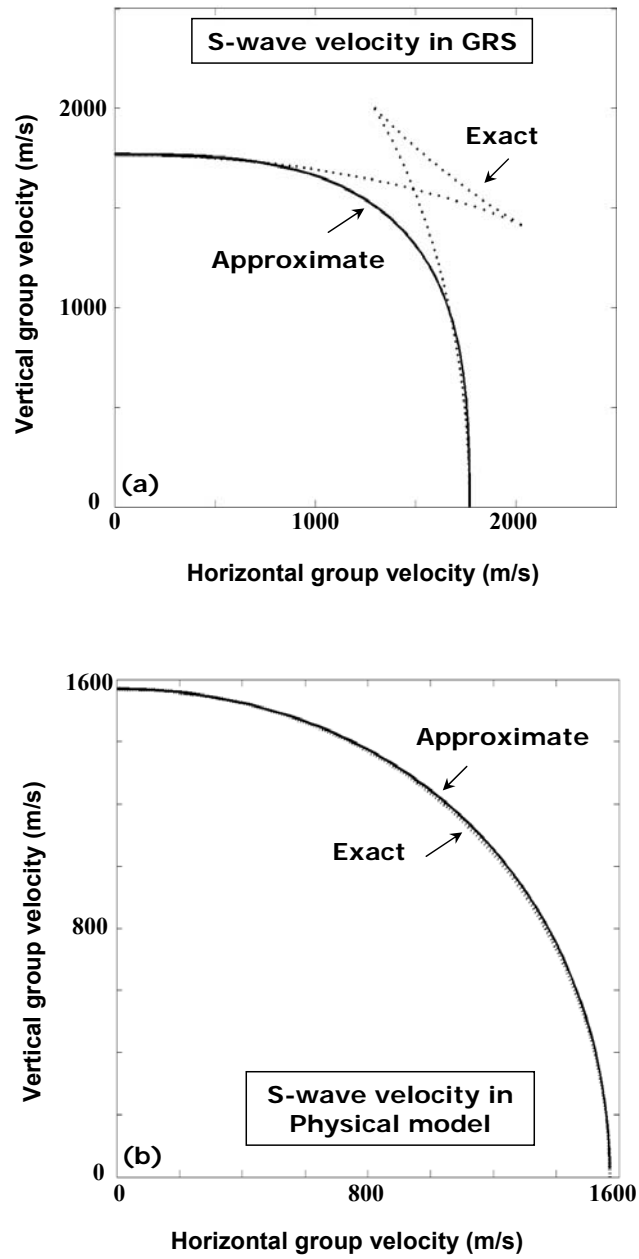
Figure 3.5. Comparison of S-wave group velocities computed with approximate method (equation 3.5) and exact method (section 3.2.2; Červený, 1972), in (a) Green River Shale, and (b) Physical model.
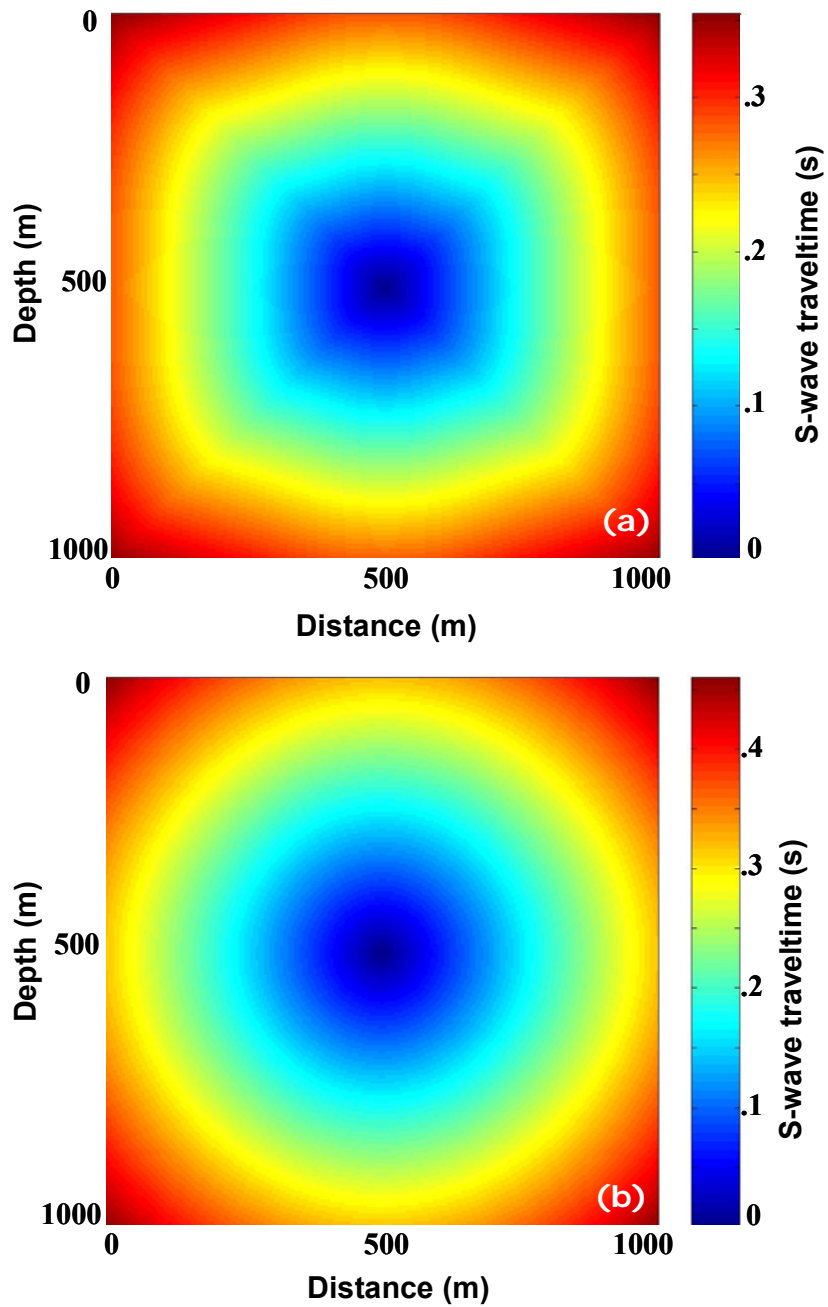
Figure 3.6. S-wave traveltime contours in homogeneous TI media, (a) Green River Shale, and (b) Physical model. A point source is placed at the center of the model.

66

3.3 ANISOTROPIC DEPTH MIGRATION: PRINCIPLE

Schneider (1978) posed migration as a boundary value problem, which led to an integral or summation algorithm, and is the basis of Kirchhoff migration. Kirchhoff migration assumes a diffraction model, and the image is constructed by the summation of these diffractions as a perturbation with respect to a reference medium. The image at a grid point can be estimated by,

$$u(\mathbf{x}, z) = \iint \frac{u(t, z_0)}{A g_{x-s} g_{x-r}} d\mathbf{s} d\mathbf{r} \,, \tag{3.7}$$

where $\mathbf{x}$, $\mathbf{s}$, and $\mathbf{r}$ represent the grid, source, and receiver locations, respectively, $u(t, z_0)$ is the recorded wavefield at the surface (z_0) with traveltime $t = t_{x-s} + t_{x-r}$, where t_{x-s} and t_{x-r} are the traveltimes from point $\mathbf{x}, z$ in the subsurface to source and receiver locations $\mathbf{s}$ and $\mathbf{r}$, g_{x-s} and g_{x-r} are the polarization vectors for source and receiver, and A is an amplitude factor. For a homogeneous reference medium, A can be approximated from the asymptotic form of the Green's tensor (Eaton and Stewart, 1994) as,

$$A = A_s A_r = \frac{1}{4\pi\rho v_s |x-s| \sqrt{K_s}} \frac{1}{4\pi\rho v_r |x-r| \sqrt{K_r}} \,, \tag{3.8}$$

where A_s and A_r are the amplitudes, v_s and v_r are P-wave group velocities, K_s and K_r are the Gaussian curvatures for the source and receiver side, respectively, ρ is the density of the medium, and $|x-s|$ and $|x-r|$ are the distances from source and receiver respectively to the grid point.

I have implemented an anisotropic Kirchhoff depth migration scheme based on equations (3.7) and (3.8) in which the traveltime calculation is done using the method described in the previous section.

3.3.1 Data example

The physical Modeling Facility at the University of Calgary, the Fold-Fault Research Project, collected data over an anisotropic thrust sheet embedded into an isotropic medium (Figure 3.7). Thomsen parameters for the thrust sheet are, α_0 = 2870 m/s, β_0 = 1570 m/s, δ = 0.204, and ε = 0.223; the fifth parameter γ is not considered as I am dealing with P-waves only. The isotropic background is Plexiglas with a P-wave velocity of 2740 m/s and density of 2.74 g/cm^3. The base of the model is a flat aluminum plate with a P-wave velocity of 5402 m/s. Sonic transducers were used as sources and receivers with a source spacing of 60 m and receiver spacing of 20 m. The data used here contain 86 shots and 256 receivers for each shot. The model is laterally heterogeneous, and the tilt (0^0, 30^0, 50^0, and 60^0) of the axis of symmetry for the TI thrust sheet is laterally variable. This is a 2D model with dimensions of 5100 m by 2200 m.

I display in Figure 3.8, the travel time contours for this model for a source placed at the center of the model. From the traveltime contour (Figure 3.8), the TI thrust sheet can be easily identified. Note that the aluminum plate has very high velocity resulting in a large contrast; this is evident in the traveltime contours. For use in migration of the physical model data set, traveltime tables are computed for all source and receiver locations on the recording surface.
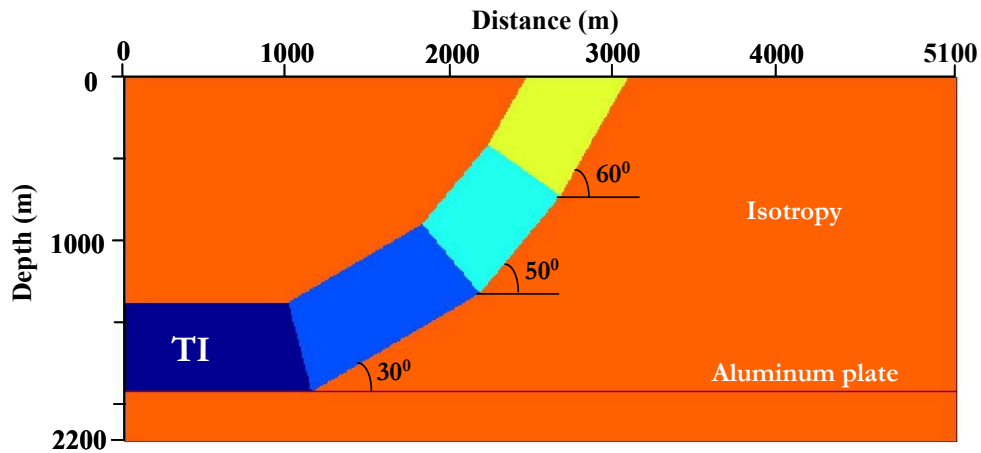
Figure 3.7. A physical model with a TI thrust sheet embedded into an isotropic background. A flat reflector (aluminum plate) has been placed at the base of the thrust sheet. The Thrust sheet has been divided into four TI blocks with varying angles of axis of symmetry with respect to the vertical axis.
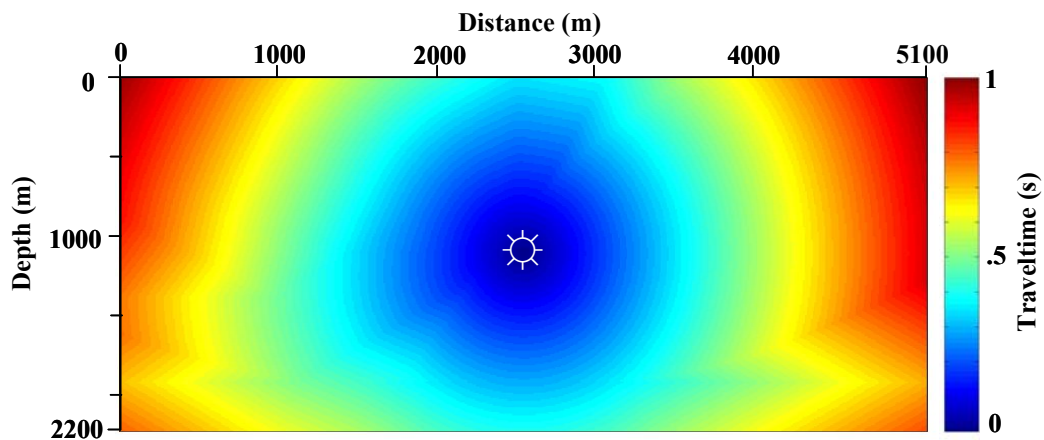
Figure 3.8. Traveltime contours for the model shown in Figure 3.7, with a point source placed at the center of the model. The presence of a flat reflector is clear from the contour plot, and it becomes more prominent away from the source position.

The primary motivation of this migration is to image the thrust sheet and the aluminum plate below the thrust sheet (Ferguson and Margrave 2002). Kirchhoff depth migration with the new traveltime scheme is performed for each shot gather. The reference medium is homogeneous and isotropic (Figure 3.7). Figure 3.9 displays the depth images obtained after stacking of shot-migrated gathers with TTI, TI and isotropic model assumptions. The isotropic model was built using the vertical velocities at every grid point. The differences in the three migrations are attributed to the type of model considered for the traveltime computation. The image of the upper part of the thrust is good in all three cases. However, the lower flank of the thrust sheet and the contacts between various TI blocks are better imaged with the TTI model. The reflector below the thrust sheet (near 2000 m distance in the image space) is correctly imaged with a TTI model as a flat reflector, while the TI and isotropic migrations introduce artifacts in the form of anticlinal structures (marked by circles).

To assess the quality of the prestack images, I examine the common image gathers (CIG) for a location (in x-direction) at 2000 m (Figure 3.10). The images are nearly flat with a TTI migration while there are significant residuals in the TI and isotropic images (as marked in the Figure 3.10).

Figure 3.11b shows a shot-migrated and stacked image using a symmetric non-stationary phase-shift (NSPS) migration method developed by Ferguson and Margrave (2002). It is evident by comparing this image with that (Figure 3.11a) obtained by my Kirchhoff method that my algorithm developed in this chapter images the lower flanks of the thrust sheet better than the NSPS method.
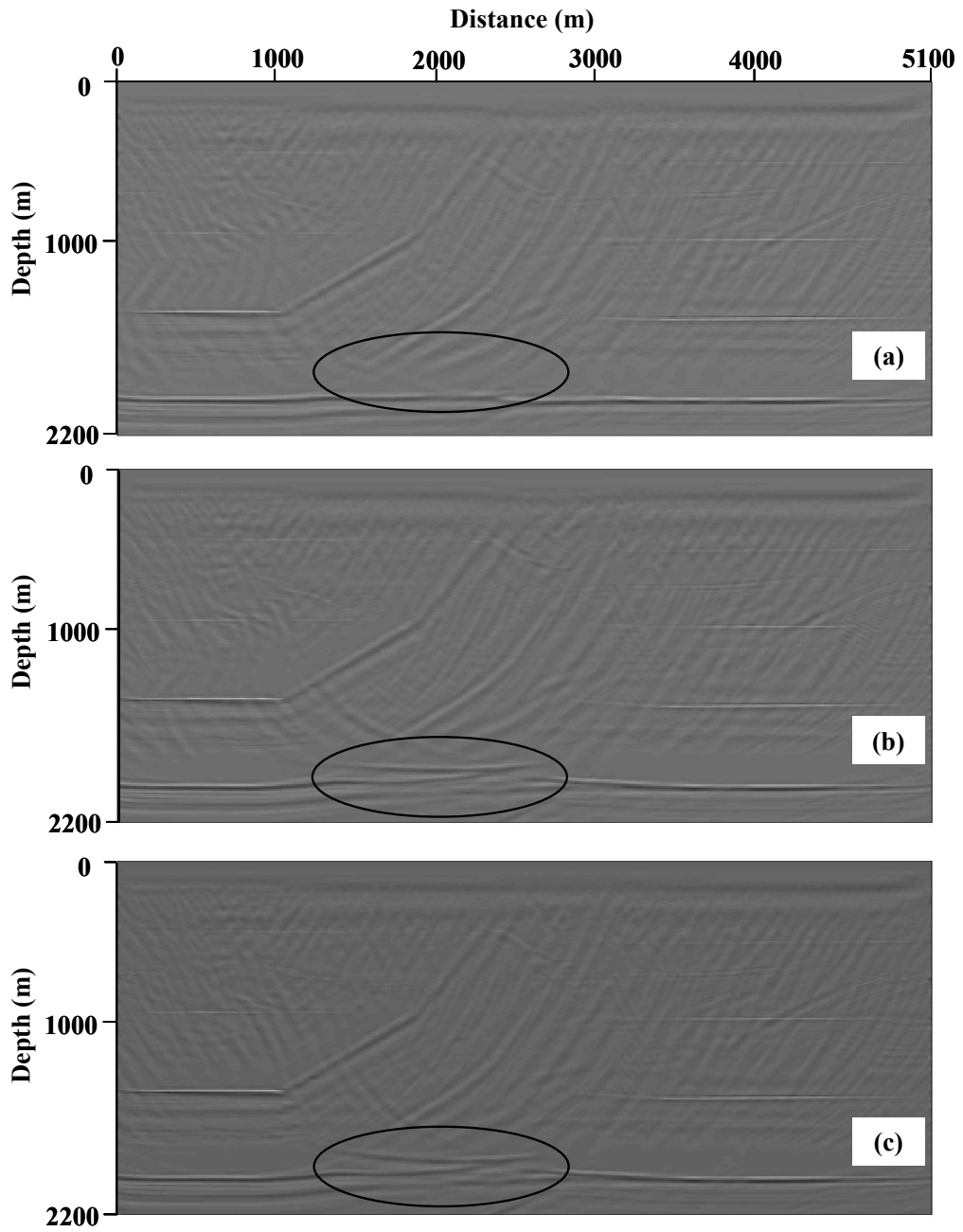
Figure 3.9. Migrated images (stack of shot-migrated gathers) of physical model using (a) TTI imaging, (b) TI imaging, and (c) Isotropic imaging.
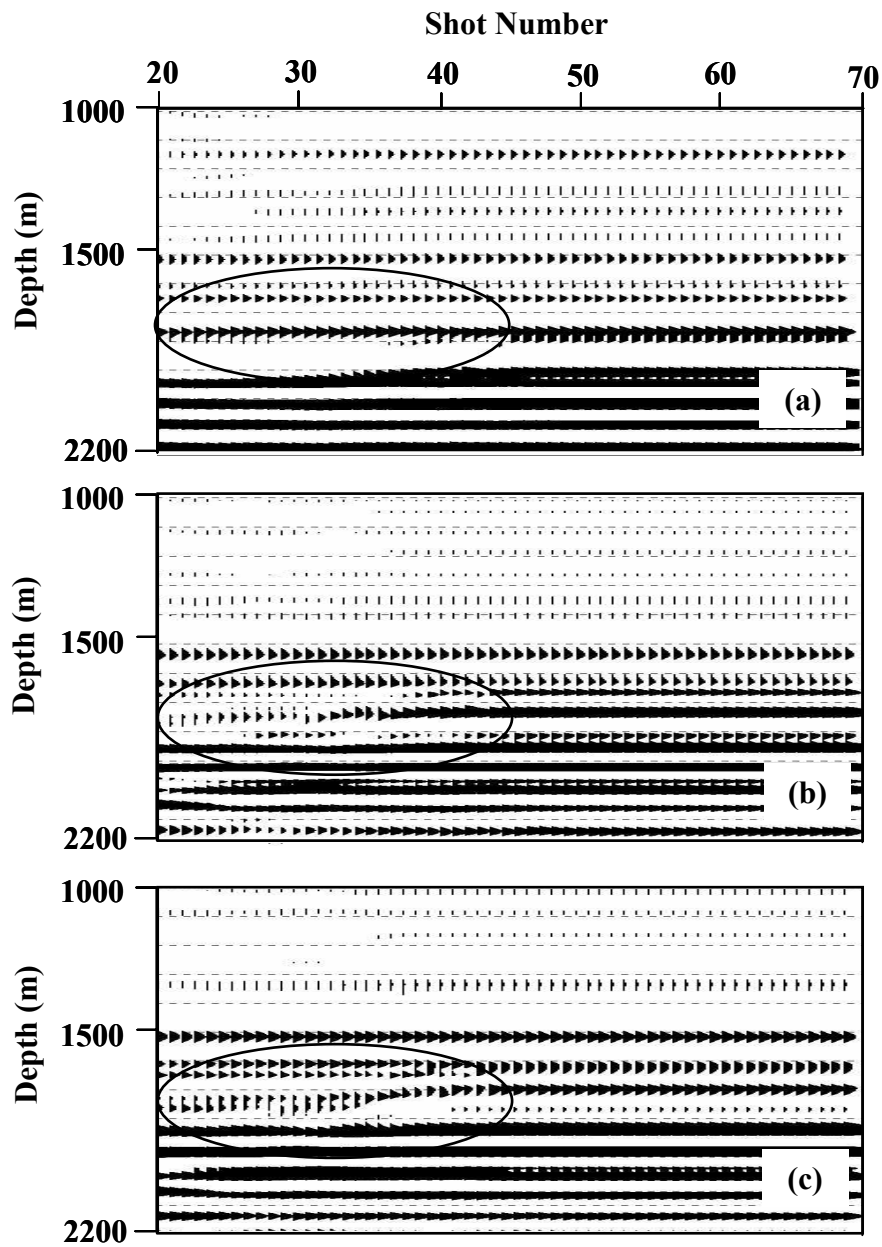
Figure 3.10. Common image gather for a surface location at 2000 m offset with (a) TTI imaging, (b) TI imaging, and (c) Isotropic imaging.

72
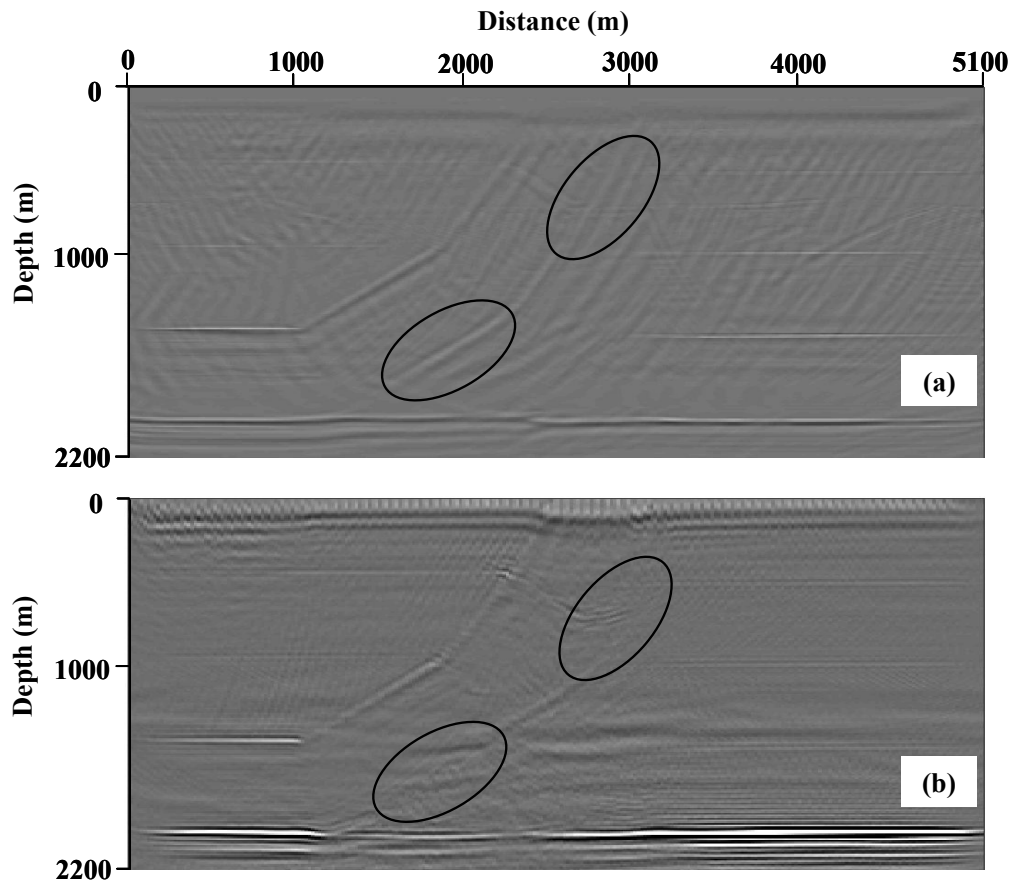
Figure 3.11. Comparison of the migrated image of physical model between (a) image from newly developed TTI imaging method (same as in Figure 9a for comparison), and (b) image from symmetric non-stationary phase-shift migration (reprocessed for display from Figure 11 in Ferguson and Margrave (2002)). Kirchhoff method images the lower flank better than the NSPS method (marked with circles). This is because the Kirchhoff method is fairly accurate for all angles of propagation as long as the travel times can be computed accurately.

3.4 SUMMARY

For subsurface imaging in anisotropic media, imaging algorithms must be modified to include anisotropic propagation effects. Most imaging algorithms can be easily modified simply by using a phase term (traveltime) approximation for anisotropic propagation. For Kirchhoff migration, the traveltime algorithms need to be modified to include anisotropic propagation. Here I have developed a direct method of traveltime computation in tilted transversely isotropic media for use in a Kirchhoff based anisotropic depth migration. Simple modification of a TI traveltime algorithm by using a parametric representation for the group velocities enables us to compute traveltimes in tilted TI media. Even though I compute only the first arrivals, this traveltime scheme is robust as it avoids the limitations of ray theory and finite-difference methods. To demonstrate this approach, I migrated a physical model data with TTI, TI, and isotropic traveltime tables and demonstrated that a TTI migration images the structure beneath the thrust sheet very well, while TI or isotropic migration introduces false anticlinal structures. I also compared my result of TTI migration with those obtained by a symmetric non-stationary phase shift migration method and found that my approach images the flanks of the thrust sheet better. The traveltime scheme proposed in this chapter is efficient in 2D, but computationally intensive in 3D, and I believe that wavenumber based migration methods such as NSPS may be preferable over a Kirchhoff migration in 3D for general anisotropic media unless more efficient traveltime calculation algorithms are developed.

74

Chapter 4: The Hydrate Ridge experiment:
Analysis of P-wave data

4.1 INTRODUCTION

A seismic experiment was conducted during the summer of 2002 at the Hydrate Ridge (HR) of the Cascadia convergent margin (Figure 1.4) using a seismic vessel (R/V Maurice Ewing) and a drilling vessel (JOIDES Resolution) in coordination with Ocean Drilling Program Leg 204. This experiment brought together multi-disciplinary scientists to understand the origin, formation, distribution, stability, saturation, physical and chemical properties (and proxies), cycle of formation and dissociation, and effects of gas hydrates in an accretionary ridge and adjacent slope basin at HR.

The seismic experiment at HR was aimed at estimating P- and S-wave velocity profiles in the gas-hydrate-bearing sediments, and calibration of gas-hydrate-bearing sediments with seismic velocities for remote quantification of gas hydrates. Special emphasis was given on S-wave analysis, as from previous studies at HR no S-wave velocity information was available. This is because the S-wave together with the P-wave velocity is useful in detecting and quantifying gas hydrate and free gas, and inferring paths of fluid migration.

In this chapter, I will describe the methods for and results from analysis of the P-wave data. I found convincing evidence of anisotropic effects in the data from the south ridge. Therefore a part of my analysis is aimed at estimation of anisotropic parameters and interpretation of these results.

4.2 GEOLOGICAL BACKGROUND AND DATA ACQUISITION

Hydrate Ridge is located offshore the northwestern United States, and is formed by the subduction of the Juan de Fuca plate beneath the North American plate at a rate of about 4.5cm/yr (Figure 4.1). Sediments on the subducting plate contain large volumes of sandy and silty turbidites. At present most of this sediment is accreted onto the continental margin either by off-scraping at the deformation front or by underplating beneath the accretionary complex (MacKay, 1995). Sediments on the ridge are Pliocene in age. The ridge is characterized by a northern peak having a minimum water depth of 600m and a southern peak with a water depth of 800m (Figure 1.4).

Subducting sediments and fluids will experience compressive force and as the ridge forms and sediments on the top of the ridge will move away from the ridge (extensional force) which will in turn create normal faults. Methane-rich fluids will migrate up towards the seafloor, and they form gas hydrates in favorable thermodynamic conditions (Figure 1.3a). Methane gas is primarily of biogenic origin (inferred from carbon-isotope composition, methane has δ^{13}C lighter than -60‰) (Kvenvolden, 1993) but higher order hydrocarbons of thermogenic origin are also present. If gas saturation is in excess compared to water saturation or if the water salinity is high (≈ 105gkg^{-1}) then free-gas can be present together with the gas-hydrate (e.g., Milkov et al., 2004). Gas hydrates and methane gas have been observed on the sea floor by submersible and deep-towed video surveys (Suess et al., 2001).

Various authors have studied the geological settings (Riddihough, 1984; Mackay, 1995; Trehu et al., 1999), bio-geo-chemical properties (Boetius et al., 2000), fluid migration (Suess et al., 2001; Riedel et al., 2001), heat flow variations (Ganguly et al., 2000) and carbon cycle (Dickens, 1999) of the gas hydrate system on the Cascadia margin at HR.

Figure 4.2 shows a model of the two-ship seismic experiment conducted at the HR. A W-E profile of streamer seismic data across south ridge through sites 1250 and 1251 is shown in Figure 4.3. A "bright" reflection, following the sea floor reflection marks the base of gas hydrate stability; it is known as the bottom simulating reflection (BSR). A BSR is a seismic attribute of gas hydrate in seismic data which is caused by a strong negative velocity contrast (due to higher velocity in the hydrate layer above the BSR and the lower velocity in the free gas below the BSR). Some characteristic features of the BSR seen in the Figure 4.3 are: 1) it mimics the relief of the seafloor (maintaining thermodynamic stability), 2) reflection polarity reversal with respect to the seafloor reflection polarity, and 3) a bright reflection (Shipley et al., 1979). The BSR is very strong in the summit side but not present (or very weak) in the slope basin (towards east in Figure 4.3) which may indicate that free gas is not available in the slope basin side. It demonstrates that the presence of the BSR is not compulsory for the presence of gas hydrate. Gas hydrate is stable from the BSR to the seafloor level which can be referred to as the gas hydrate stability zone (HSZ). Free gas is normally found below the hydrate layer (Bangs et al., 1993), and it may be overpressured and creates hydrofractures to move through the hydrate layer up to the seafloor.
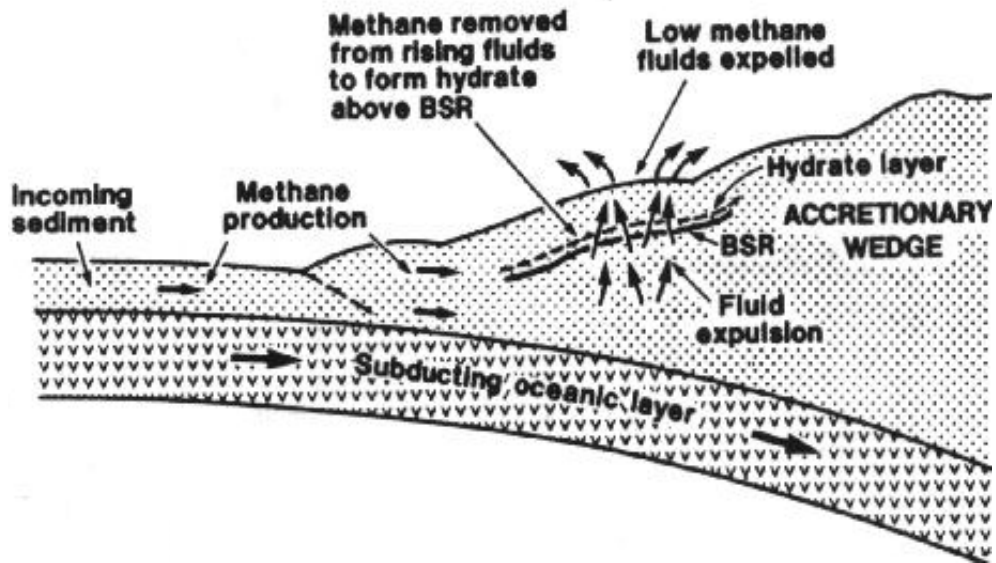
Figure 4.1. Subduction of Juan de Fuca plate beneath North American plate (Riedel et al., 2001).
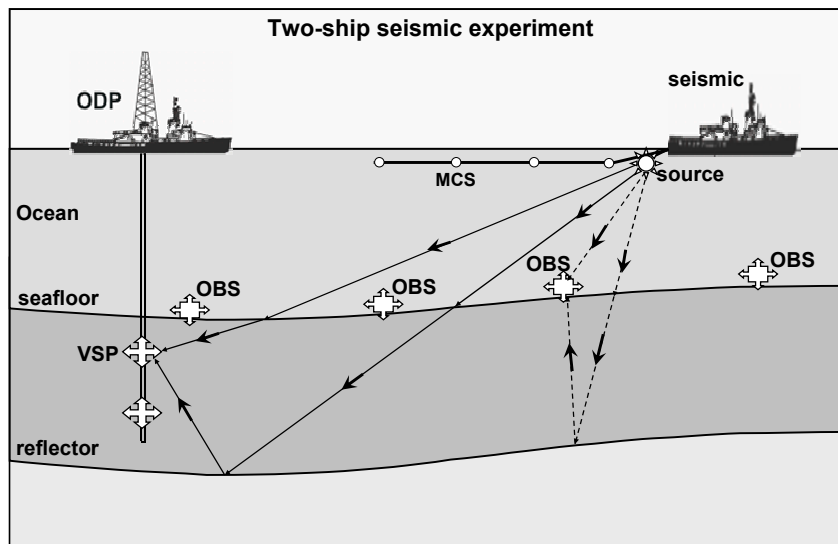
Figure 4.2. Two-ship seismic experiment: acquisition geometry for multicomponent (VSP and OBS) data and streamer data (MCS) recording are shown. Arrows show the ray paths of direct and reflected waves to VSP and OBS receivers.
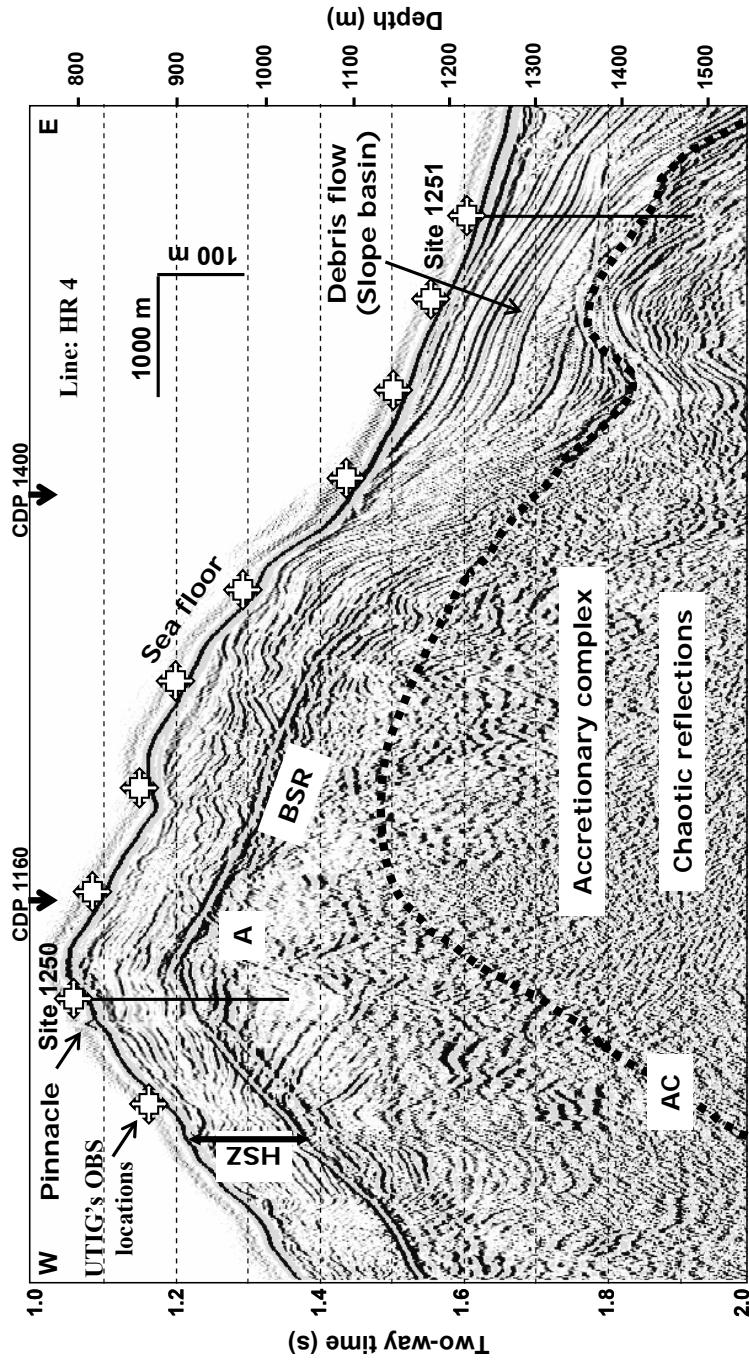
Figure 4.3. An east-west 2D (streamer) seismic data across south ridge through sites 1250 and 1251 (Figure 1.4) shows stratigraphy and structural settings. A strong reflection, following the sea floor reflection marks the bottom of gas hydrate stability, is known as bottom simulating reflection (BSR) (Figure 4.3b). Bright reflection 'A' has been speculated as a major source for methane-rich fluid to the south summit and is also the cause of Pinnacle (a carbonate mound). AC marks the top of the seismically incoherent reflection. Figure is vertically exaggerated 8 times. Average dips of the seafloor are 6^0 and 5^0 in the west and east side of summit, respectively.
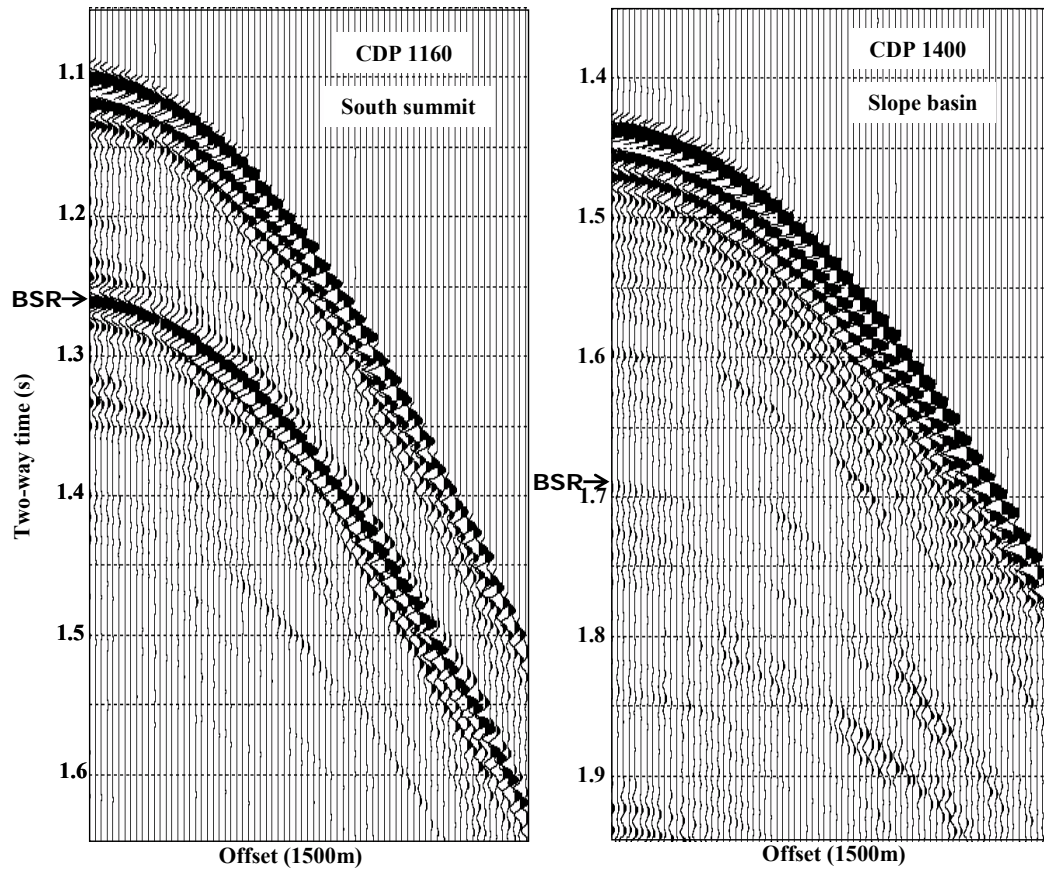
Figure 4.3a. BSR amplitudes: Comparing BSR amplitudes at the two locations 1) south summit (CDP 1160) and 2) slope basin (CDP 1400) marked in Figure 4.3. It is evident that BSR reflection response is very weak at the slope basin compared to the south summit, which supports the similar amplitude response in the stacked section (Figure 4.3). Note that the seismograms are plotted with a constant gain.

Three types of seismic data were simultaneously acquired in this experiment (Figure 4.2): 1) multichannel seismic (MCS) data, where a streamer (carrying hydrophones) is towed behind the seismic ship, 2) walkaway vertical seismic profile (VSP) data, in which the receivers are placed at a single fixed positions in a borehole, and 3) ocean-bottom seismmometer (OBS) data, by placing an individual group of receivers on the sea floor. Shooting is done with a seismic ship. A walkaway VSP records the three components of the particle motion and an OBS records pressure on the hydrophone along with three components of the particle motion on three mutually orthogonal geophones.

The MCS profiles were recorded across the south ridge using a 1500m long streamer with 120 receiver arrays spaced 12.5m apart. The recording sampling interval was 1ms with a record length of 6s. 2-GI air-guns were used as a source (shot spacing is 20m) with an air pressure of 2000psi.

The VSP recording includes zero-offset (z-VSP), constant-offset (c-VSP), and walkaway-VSP (w-VSP) at the selected sites. A Schlumberger instrument was used for recording with a sampling interval of 1ms within a frequency band of 10Hz to 250Hz. I used 3-C w-VSP data recorded at two drill sites 1250 (two depth locations) and 1251 (one depth location) (Figure 1.4) in my analysis.

Fourteen OBS instruments from UTIG and fifteen OBS instruments from Woods Hole Oceanographic Institution (WHOI) were used in the 3D survey. I analyzed the data from the OBS receivers placed on the south ridge to slope basin (about 1km spacing as marked in Figure 4.3). Four-component data were recorded with a sampling interval of 3ms (5ms for WHOI) and a cut-off frequency of 50Hz

for geophones and 80Hz for hydrophones. See Nakamura et al. (1987) for a detail description of the UTIG instrument and basic data processing (also discussed in Chapter 5).

4.3 INTERACTIVE INTERVAL P-WAVE VELOCITY ANALYSIS

Traditionally, a root mean square (rms) P-wave velocity is estimated from the normal moveout analysis of hydrophone common mid-point (CMP) gathers in offset-time domain (Yilmaz, 2001). The output is the P-wave rms velocity versus two-way zero-offset traveltime and then Dix's (1955) equation is used to estimate interval velocity. In the case of VSP and OBS recording, the data are the receiver gathers (CMP gathers are not feasible), and the objective here is to find the interval velocity in depth. For this purpose velocity analysis in the τ-p domain (intercept time – ray parameters) is preferred. I performed the interval velocity analysis in the τ-p domain assuming a locally 1D earth model resulting in interval layer velocities as a function of depth.

The τ-p trajectory of a reflected P-wave (PP-wave) in an isotropic medium (Bessonova et al., 1974) is given by

$$\tau_{PP}(p) = 2\tau_P^0 \sqrt{1 - p^2 v_P^2} , \qquad (4.1)$$

where τ_P^0 is one-way vertical (zero-offset) delay time for P-wave and v_P is the interval P-wave velocity for a layer. This formulation requires the data in the τ-p domain. The steps for the interactive interval P-wave velocity analysis assuming locally 1D isotropic media are as follows:

1. Convert the P-wave data (hydrophone or vertical component data) from offset-time to τ-p domain using plane wave decomposition (Stoffa et al., 1981; Treitel, et al., 1982).

2. Identify the P-wave reflection events between which velocity is desired.

3. Interactively pick a velocity (v_P) for a reflection event (τ_P^0 is known) for which a modeled τ-p trajectory (equation 4.1) matches the data.

4. In starting, the event picked (in step 3) is the first event, which in the case of OBS data will be the one-way direct arrival response. The output from step 3 is the interval velocity for that layer. Depth of this layer is estimated with the known velocity (v_P) and vertical traveltime (τ_P^0).

5. Repeat steps 3 and 4 for each reflection event in a top-down fashion.

6. Final output is a 1D interval velocity model in depth.

7. For the OBS data, double the depth of first layer, and in the case of VSP data double the depth of each layer up to the receiver level.

In our experiment, very few w-VSP data were recorded, therefore I used the hydrophone OBS data and performed the steps mentioned above to individual receiver gathers and estimated the 1D interval P-wave velocity at the OBS locations. The 1D velocity models estimated at each OBS location were interpolated to produce a smooth 2D P-wave velocity profile (W-E) across south ridge from summit to the slope basin side (Figure 4.4). The P-wave velocity profile has been superimposed on the stack section derived from the streamer data (Figure 4.4).
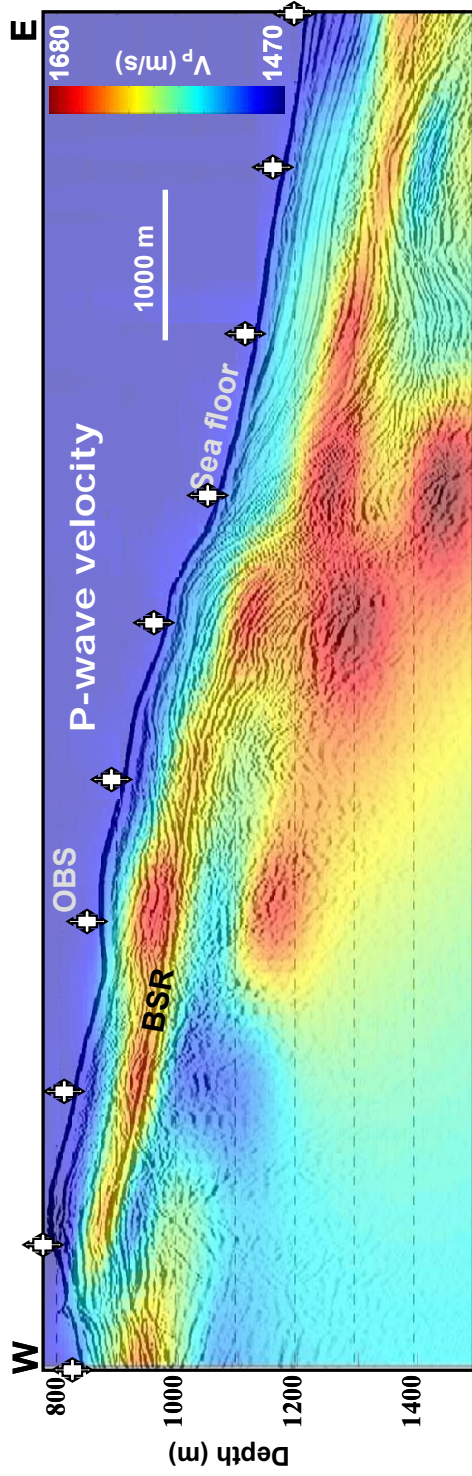
Figure 4.4. The P-wave velocity profile derived from a velocity analysis using OBS data (about 1km spacing) across south ridge from the south summit (W) to the slope basin side (E). Velocity data have been superimposed on the streamer data (Line HR4) along OBS locations. Seafloor and BSR reflections are marked on the section. Note the higher velocity above BSR level suggesting the presence of gas hydrates, and lower velocity below BSR towards ridge due to the presence of free gas. There is no lowering of velocity below BSR level towards slope basin (covering four rightmost OBSs) suggesting an absence of free gas, which is also evident due to discontinuous (or absence of a strong) BSR reflection. However, BSR is locally present in the basin (east) near anticlinal structures suggesting presence of free gas.

4.4 VSP (P-WAVE) DATA ANALYSIS: EVIDENCE OF ANISOTROPY

From the velocity analysis, a general trend in the isotropic P-wave velocity distribution is estimated (Figure 4.4). However, a closer look at VSP data near the south summit reveals that these data cannot be modeled using an isotropic velocity model. This is not surprising since sedimentary formations are known to exhibit anisotropy in the presence of fine layering (VTI anisotropy) and/or vertical fractures (HTI anisotropy). In this section I attempt to incorporate anisotropy in the velocity estimation. Seismic P-wave reflection data recorded on the surface are not sufficient to estimate seismic anisotropy parameters uniquely as vertical velocity and the anisotropic parameter δ cannot be uniquely determined (Tsvankin and Thomsen, 1995; Alkhalifah and Tsvankin, 1995). I will use the VSP data from site 1250 at the south summit (Figures 1.4 and 4.3) for anisotropic parameter estimation. In the VSP geometry, the depth of the layer is known so the vertical velocity can be determined with known vertical traveltime and depth information thereby avoiding the ambiguity between vertical velocity and depth.

I consider a three-layer (2D homogeneous) model. The first layer is the water layer, the second layer is defined by VSP (from the water bottom to the borehole receiver) depth, and the third layer is a half space below the receiver position. The P-wave velocity in water has been considered as constant (Figure 4.5). In this simple model the depth of the second layer is known and only the elastic parameters (velocity anisotropy) need to be determined. Figure 4.6 shows an isotropic ray-tracing with a trial velocity model. The model depicts the VSP traverse at site 1250 towards north. It is evident that near-offset and far-offset rays

85

on the surface are propagating almost vertically and horizontally with vertical and horizontal velocities within the second layer, respectively. If the second layer is isotropic then the velocity will be invariant (i.e., horizontal velocity equals vertical velocity).

To estimate the velocity variations in the second layer, I performed a traveltime-error-contour analysis (Figure 4.7). Traveltime-error is the traveltime difference between real data (picked from the vertical component of the w-VSP at 1250 north traverse) and synthetic data (using the traveltime computation method discussed in chapter 3). A total of 3km of source-receiver offset data have been used to calculate the rms traveltime-error contour for a range of realistic values for the parameters of the second layer (velocity and depth) as shown in Figure 4.7a (contour value is rms error). The optimum model will correspond to a minimum error value which is not unique and we observe a range of model parameters. However, the depth of the second layer (VSP depth) is known which gives a range of possible values for the P-wave velocity corresponding to a minimum traveltime error (Figure 4.7a). Now I examine the match of the near-offset (Figure 4.7b) and far-offset (Figure 4.7c) traveltime data to approximately estimate the vertical velocity (α_0) and horizontal velocity (α_{90}), respectively. For this layer I find that P-wave velocity of 1700m/s fits the near-offset traveltime well while I require a slower (1550m/s) P-wave velocity to model the far-offset traveltime data. Such an effect can be explained either by HTI anisotropy or lateral heterogeneity. I examine both of these possibilities first in succession and then in a formal combined analysis. I will discuss (2D) homogeneous parameters

86

estimation in this section and heterogeneous parameters estimation in the next section by seismic inversion using VSP and OBS data.

Once the velocity variations are approximated, in a weak VTI assumption P-wave anisotropy parameter epsilon (ε) can be estimated by equation (1.3) as

$$\varepsilon = \frac{\alpha_{90} - \alpha_0}{\alpha_0} = \frac{1550 - 1700}{1700} = -0.09 . \tag{4.2}$$

This suggests a 9% P-wave anisotropy in the second layer (Figure 4.6) at the south summit. For a better estimation of anisotropic parameters (ε and δ) and uncertainty ranges, I performed another traveltime-error-contour analysis with a spectrum of epsilon (ε) and delta (δ) values keeping the vertical velocity fixed (Figure 4.8).

My error-contour reveals that the parameter ε is well constrained but δ (estimated with P-wave analysis) is very poorly constrained (Figure 4.8a). For effectiveness of these parameters, I matched the near-offset and far-offset transmitted traveltime data (north traverse at VSP site 1250) for isotropic and anisotropic models. The isotropic model (using vertical velocity) fits the near-offset data well (Figure 4.8b) but is unable to match the far-offset traveltime observations (Figure 4.8c). On the other hand the anisotropic model matches the data at all ranges of offsets. The homogeneous P-wave anisotropic model parameters for the second layer are estimated to be $\{\alpha_0 = 1700m/s$, $\varepsilon = -0.09 \pm 0.01$, and $\delta = 0.05 \pm 0.1\}$. It predicts an HTI model (since ε is negative). This model will be used to build an initial model for inversion in the next section.
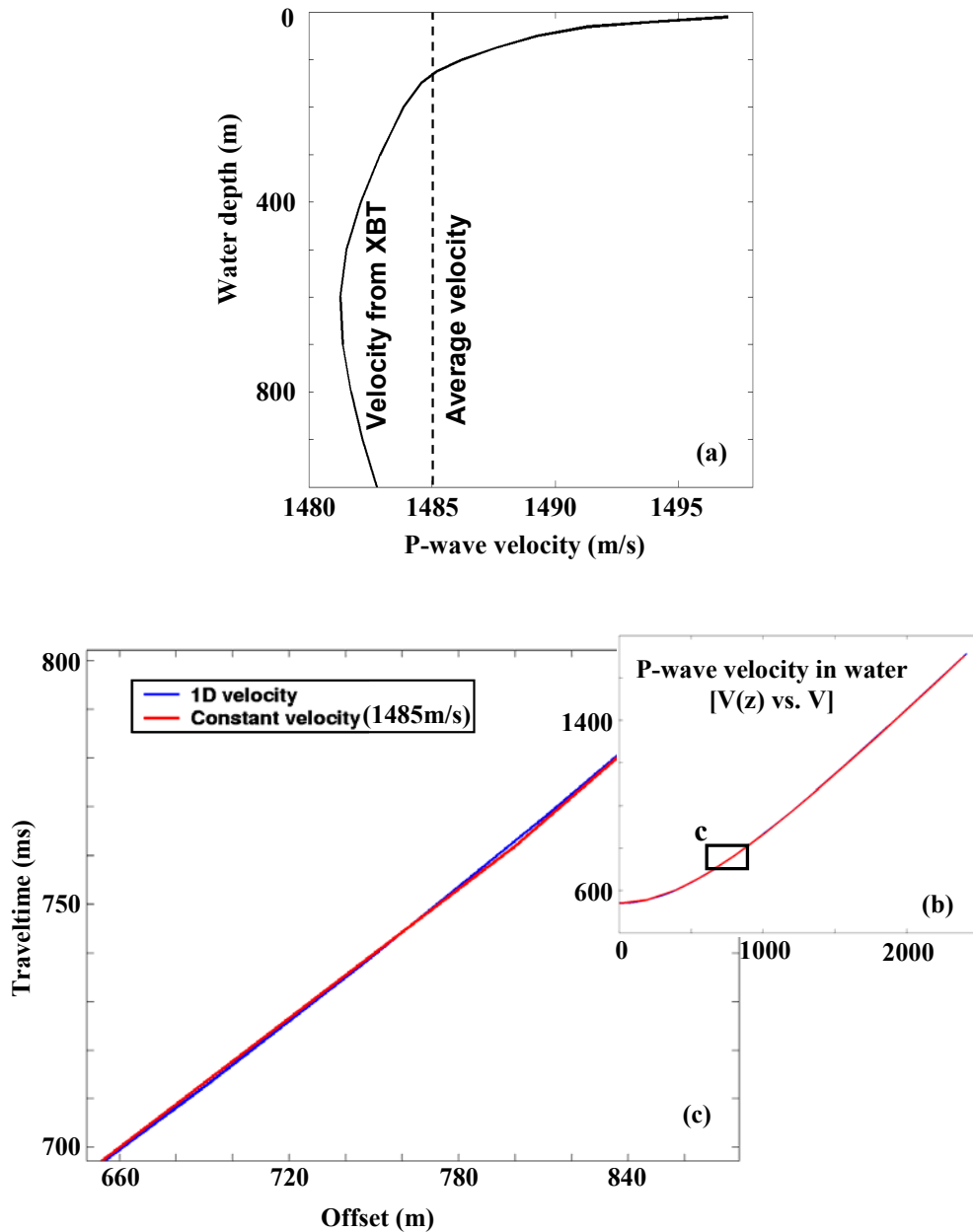
Figure 4.5. P-wave velocity in sea-water: (a) velocity from XBT (Expendable bathythermograph), (b) comparison of direct wave traveltimes computed with 1D and constant velocity for an OBS receiver placed at the water depth of 800m, and (c) is a zoom plot of area "c" marked in (b). The result indicates that the water layer can be modeled as a homogeneous layer with a constant velocity of 1485m/s.
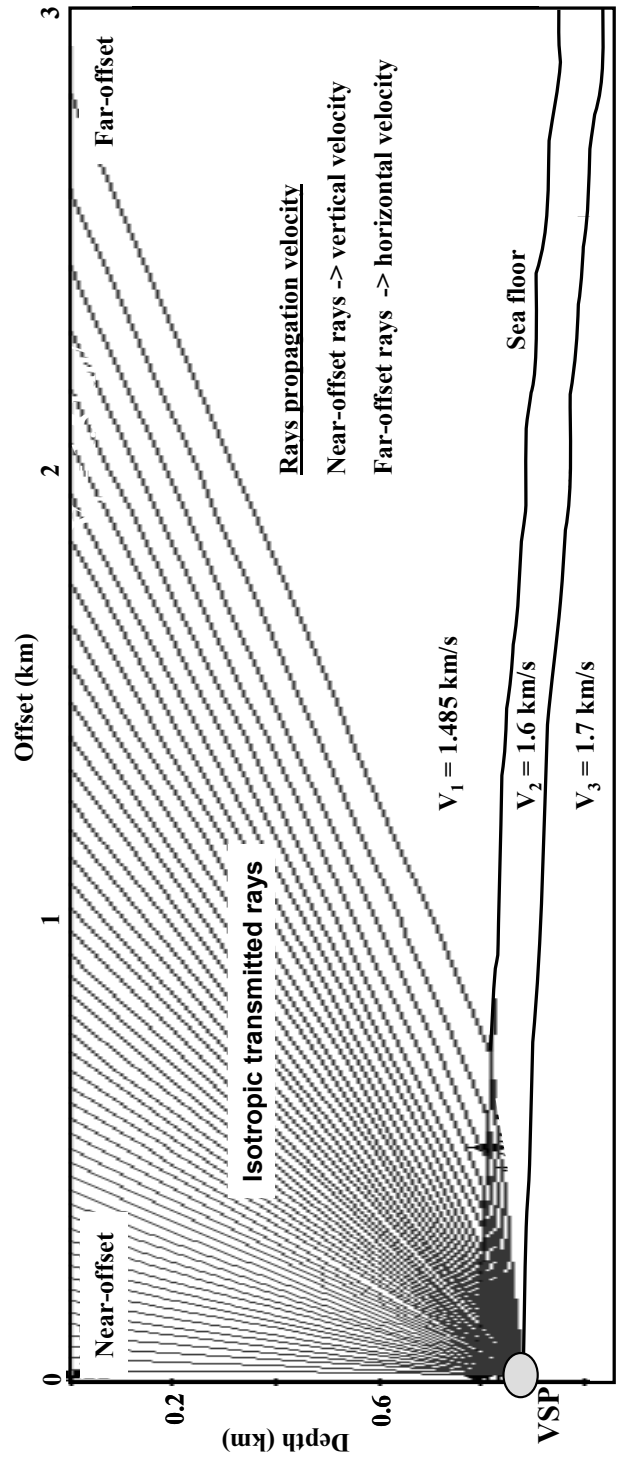
Figure 4.6. Isotropic ray tracing for the VSP (#1250) geometry in a homogeneous (2D) three-layer model, where the first (thicker) layer is the water layer, the second layer is defined by VSP depth, and the third layer is below the VSP depth. First layer interface (sea floor) follows the bathymetry of S-N traverse of w-VSP at site 1250 and the second layer follows the seafloor. Increasing offset is from the VSP site towards north at the south summit. Note that near-offset and far-offset rays on surface are propagating with vertical and horizontal velocities in the second layer, respectively. Velocity will be invariant if the second layer is an isotropic medium.
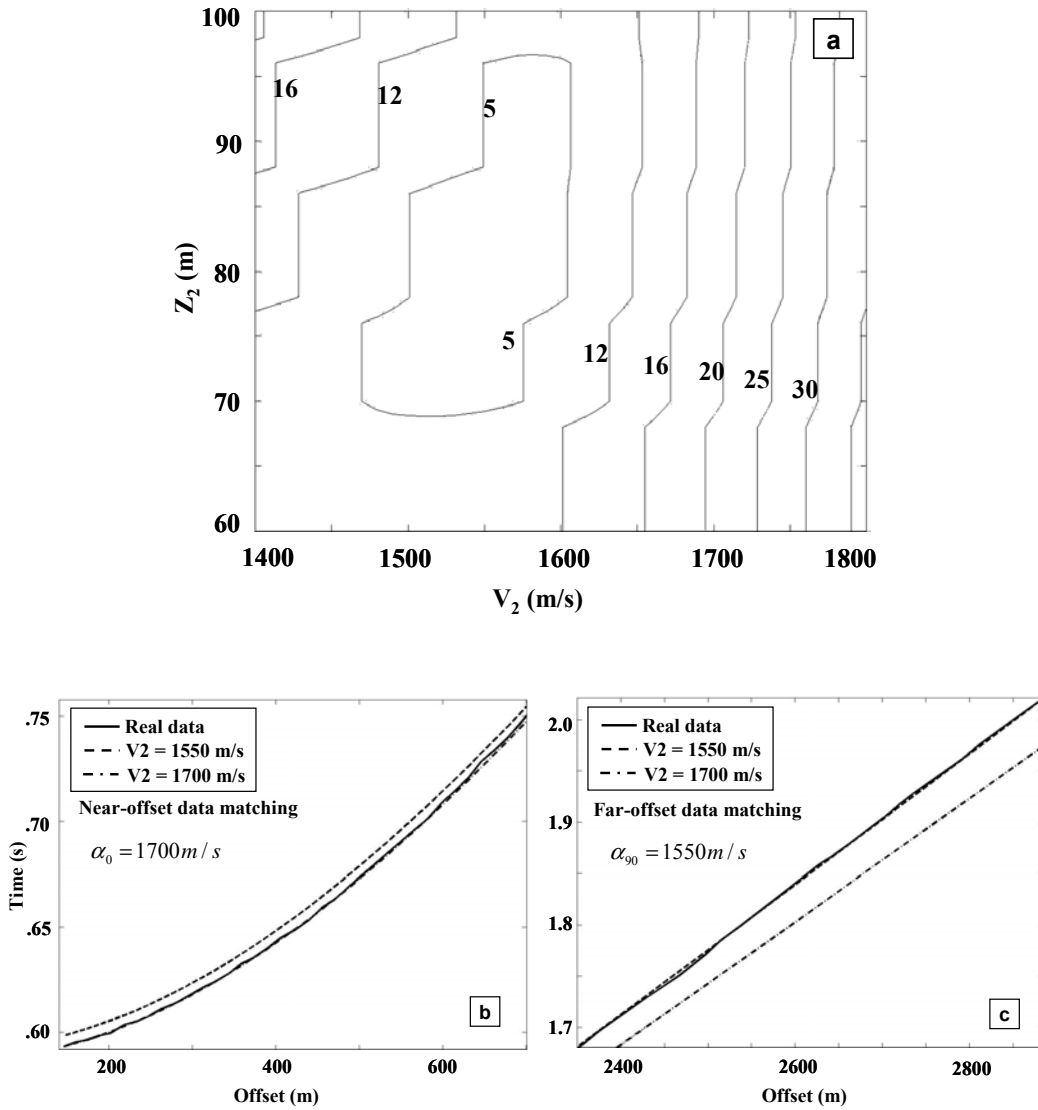
Figure 4.7. Traveltime-error-contour analysis for the estimation of velocity in the second layer (Figure 4.6). Traveltime error is the difference between the real data and modeled data for a spectrum of interval P-wave velocity and depth of the second layer. The minimum rms error (contour values) will give the optimum model. Depth of the layer (VSP receiver depth, 91m) is known, which gives a range of possible velocity values (a). By matching near-offset (b) and far-offset (c) data, approximate vertical and horizontal velocities, respectively, are estimated. Maximum offset of 3km was used.

90
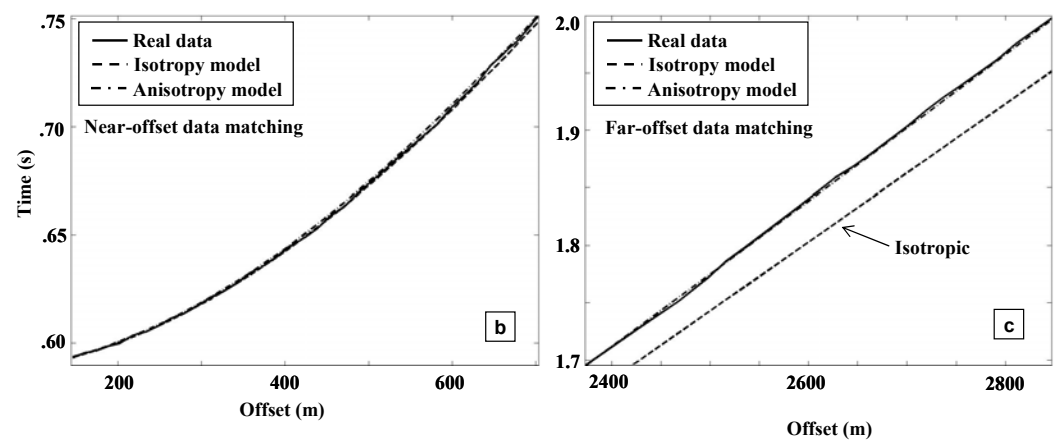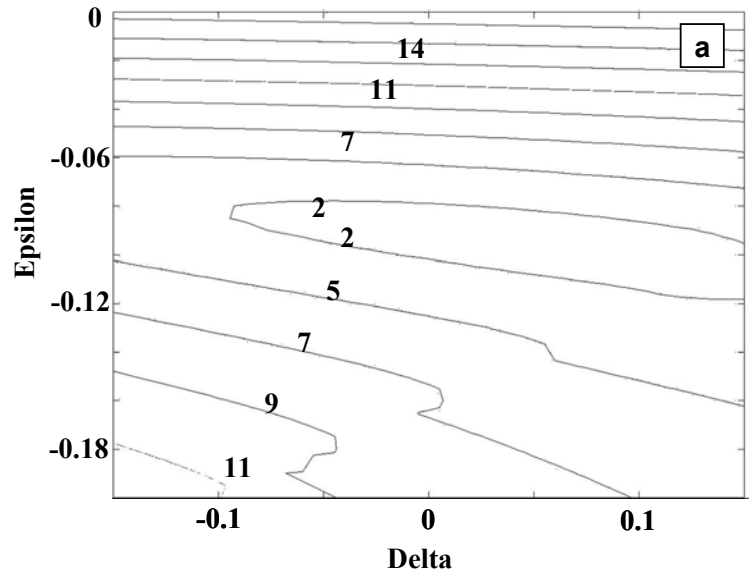
Figure 4.8. Traveltime-error-contour analysis for the estimation of anisotropic parameters in the second layer (Figure 4.6). Traveltime error is the difference between the real data and modeled data for the spectrum of anisotropic parameters of the second layer. The minimum rms error (contour values) will give the optimum model. Epsilon parameter is well constrained but delta is poorly resolved in this experiment (a). Isotropic model (using vertical velocity) data match the near-offset data well (b) but deviates from the real data at far-offsets (c). This analysis estimates homogeneous anisotropic parameters.

4.5 ESTIMATION OF ANISOTROPIC PARAMETERS BY INVERSION

Parameter estimation is an inverse problem where the model parameters are inferred from the measured data using a set of mathematical techniques. Various textbooks (Menke, 1984; Tarantola, 1987; Sen and Stoffa, 1995) discuss inverse theory. There are essentially two problems to be solved: a forward problem, which predicts the data using a mathematical model for a given set of model parameters, and an inverse problem, which predicts the model parameters using an inversion model for a given dataset.

Forward modeling is a method to predict the synthetic data for a given set of model parameters (Chapter 2). Data can be traveltimes, amplitudes, and/or full waveforms. My data are traveltimes and I am using the "Direct Method" of traveltime computation (Chapter 3) for the forward modeling. This method computes traveltimes in a heterogeneous and anisotropic medium. Six model parameters are required in a transverse isotropic medium: P- and S-waves vertical velocity (α_0 and β_0), three anisotropic parameters (ε, δ, and γ), and the rotation angle (θ) of the axis of symmetry with respect to the vertical axis. The rotation angles are zero (0) degree and 90 degrees in VTI and HTI media, respectively. For P-wave anisotropic forward modeling β_0 and γ parameters are not required. The method discussed in Chapter 3 gives only transmitted (or direct) arrival data; for reflection traveltimes I used Fermat's principle to find a minimum traveltime from source to reflector and then to the receivers.

One goal of seismic inversion is to find model parameters by minimizing the difference between synthetic data (calculated with forward modeling) and real (measured) data. The result is a set of optimum parameters. Since in general, many sets of model parameters can match the real data nearly equally well, prior constraints are imposed to estimate solutions that are geologically meaningful, from a large set of non-unique answers.

The inversion process starts with an initial guess of model parameters. Synthetic data are generated using these model parameters and an error between the synthetic data and real data is calculated. An inversion scheme defines a method to change the model parameters in accordance with the error value (data fitting) by optimizing a suitably defined misfit function (or error function or objective function), and generates a new set of parameters such that the error value reduces. Once a new set of parameters are known forward modeling is performed to generate new synthetic data followed by the inversion process. These processes continue until a satisfactory data fit is achieved and the output is a set of optimum model parameters. Various model constraints are imposed to derive model parameters that are realistic. The inversion scheme can be linear, quasi-linear or non-linear, depending on the complexity of the earth model. Linear inversion is simple to perform but unfortunately, the earth's subsurface, in general, is complicated and the linear approximation may fail.

Similar to linear inversion, in non-linear inversion we look for a model (or models) for which the objective function has a minimum. Two kinds of non-linear optimization methods can be identified: 1) local optimization methods, which

search for a local minimum in the vicinity of a starting or a trial solution using properties such as the first or second derivatives of the objective function, and 2) global optimization methods, which are generally stochastic algorithms which attempt to reach the global minimum (Sen and Stoffa, 1995). Most local optimization schemes (i.e., steepest-descent and conjugate-gradient algorithms) are iterative algorithms and the principal goal is to ensure a reduction in the objective function at each iteration. In many situations, the objective function can have multiple minimum values and a local optimization method might fall into a local minimum close to the starting solution and this may not be the correct solution.

Unlike local optimization methods, global optimization methods attempt to find a global minimum of the objective (or misfit) function. They are less greedy than the well known local optimization methods in that during iterative optimization worse solutions are occasionally accepted which allow these algorithms to avoid minima. Sen and Stoffa (1995) outline various global optimization methods. Two commonly used global optimization methods are the Simulated Annealing (SA) and the Genetic Algorithms (GA). I used a variant of SA, called Very Fast Simulated Annealing (VFSA) proposed by Ingber (1989) which is faster than SA in convergence (Sen and Stoffa, 1995). The algorithm for VFSA is given in Sen and Stoffa (1995) (P. 109). Here I list the steps for the VFSA traveltime inversion scheme used in this project to estimate the heterogeneous P-wave anisotropic parameters on the Hydrate Ridge using traveltime data from VSP and OBS recording.

94

Work flow for the P-wave parameter estimation scheme is as follows:

1) Data preparation: includes filtering, trace editing, and correcting for delay times if any (there is 53 ms time-delay in these w-VSP data from HR).

2) Pick the P-wave traveltime data for about 3km (sufficient) offsets (transmitted first arrival data from vertical component of w-VSP and BSR reflection data from hydrophone component of OBS).

3) Build a 2D anisotropic model (derived from section 4.4) of α_0, ε, and δ (a coarse grid model) with lower and upper limits of these parameters (an HTI model).

4) Calculate the error between real data and synthetic data.

5) Termination condition: if error from step 4 is less than predefined error value (or if iteration number has reached a predefined value) parameter estimation is compete and therefore exit the loop.

6) Inversion scheme perturbs the model parameters according to the error value from step 4 and returns a new set of (coarse grid) model parameters.

7) Go to step 4.

Traveltime-error-contour analysis (section 4.4) gives 2D homogeneous model. I used this model to build an initial model and search rays (step 3) for traveltime inversion using VSP and OBS data. Inversions of the azimuthal data (north (N), south (S), east (E), and west (W)) are performed separately and for display two profiles are merged to show N-S and W-E profiles.

95

In this section, I will first show the isotropic inversion result at the south summit (VSP site 1250 and OBS site 3); if isotropic model can't predict the data well (within geologically consistent velocity variations) then I will show the anisotropic inversion result at the summit. After that I will show the inversion result at the slope basin side (VSP site 1251 and OBS site 19).

In isotropic inversion, only one parameter (α_0) is used (step 3 in inversion work flow) since other anisotropic parameters values are zero. In the inversion process a range of feasible velocities is given as constraints. Figure 4.9 shows isotropic P-wave velocity for N-S profile at the VSP site 1250 (south summit) derived from the P-wave arrival time (transmitted arrival) data recorded at two VSP depth locations. Isotropic model data match the near offset data well but deviate in the far-offsets (Figures 4.9b and 4.9c). If there is no bound in velocity variations then it is possible that data at all offsets can be matched with an isotropic model data, but it may not be geologically realistic. Isotropic models at this site do not predict the seismic traveltime data well, indicating that an anisotropic model is needed. For better description of the subsurface and data-fitting anisotropy model is considered at the south summit, however, there remains some ambiguity between heterogeneity and anisotropy.

Anisotropic traveltime-error contour analysis (section 4.4) predicted an HTI model at south summit. Anisotropic inversion in HTI medium is performed by rotating the axis of symmetry of the VTI model by 90^0. I present the subsurface anisotropic model parameters of un-rotated VTI media.

Figure 4.10 shows vertical P-wave velocity and epsilon model for N-S profile at south summit derived from transmitted data recorded at two VSP depths and BSR reflected data recorded at an OBS site. Figures 4.10c and 4.10d show the far-offset data matching for anisotropic model which can be compared to the isotropic data matching shown in Figures 4.9b and 4.9c, respectively. Figure 4.11 shows data fitting at all offsets of two VSP and one OBS data and a convergence curve. Convergence curve shows the reduction of error between synthetic and real data with respect to iterations in VFSA inversion process. After about forty iterations the error value is acceptable. Similarly, Figure 4.12 shows anisotropic model parameters (vertical P-wave velocity and epsilon) for W-E profile at south summit using VSP and OBS data. In all the estimated models shown, seafloor and BSR level have been marked for a reference.

Next I carried out a similar analysis on the slope basin side. Figure 4.13 shows S-N profile of an isotropic P-wave velocity model and a match for VSP and OBS data. At this location, w-VSP data at only one receiver depth are available. Unlike the south summit, the isotropic model matches the real data at the basin side well. This means that this region (slope basin) is isotropic and heterogeneous. Interpretations of these results are discussed in detail in the next section.
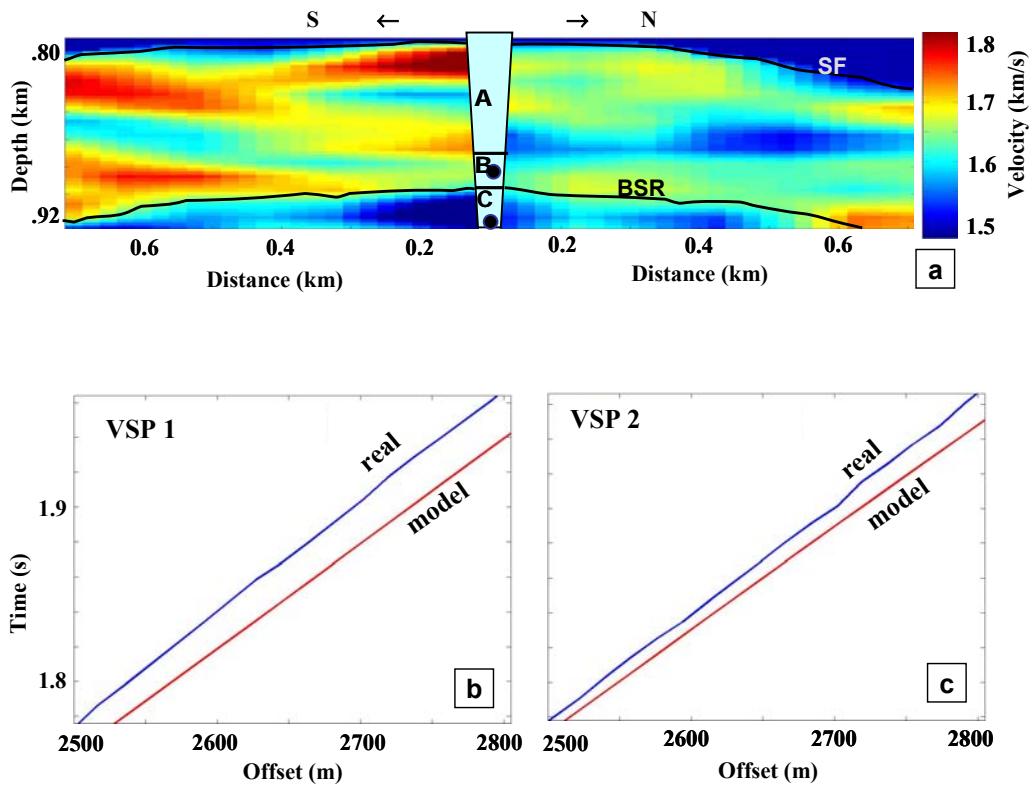
Figure 4.9. Isotropic and heterogeneous (a) P-wave velocity for S-N profile along w-VSP (#1250) traverse. VSP data at two receiver depth locations (91 and 138 meters below seafloor) have been used in VSFA based traveltime inversion. Seafloor (SF) and BSR reflectors are marked on the velocity model. Data match is good at near-offsets but poor at far-offsets. Far-offset data matching for the north traverse is shown for (b) VSP 1 and (c) VSP 2. In figure (a), VSP receiver locations are marked with dots and depth profile is divided in three zones A, B, and C.
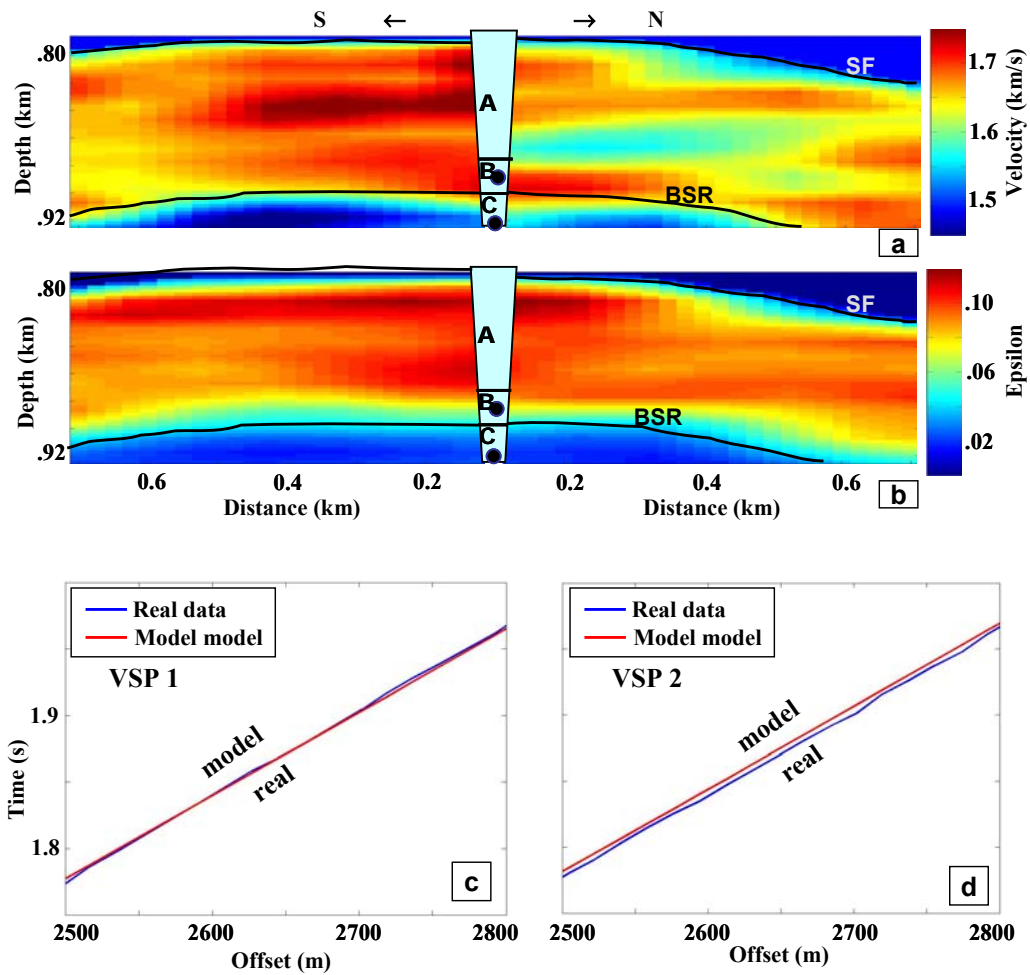
Figure 4.10. Anisotropic and heterogeneous (a) vertical P-wave velocity and (b) epsilon model (for un-rotated VTI medium) for S-N profile along w-VSP (#1250) traverse. VSP data at two depth locations (91 and 138 meters below seafloor) and an OBS (#3) data close to VSP site have been used in a VSFA based traveltime inversion. Seafloor (SF) and BSR reflectors are marked on the models. Data matching is good at all the offsets. For comparison with previous figure (Figure 4.9), far-offset data match for the north traverse are shown for (c) VSP 1 and (d) VSP 2. In figures (a and b), VSP receiver locations are marked with dots and depth profile is divided in three zones A, B, and C.
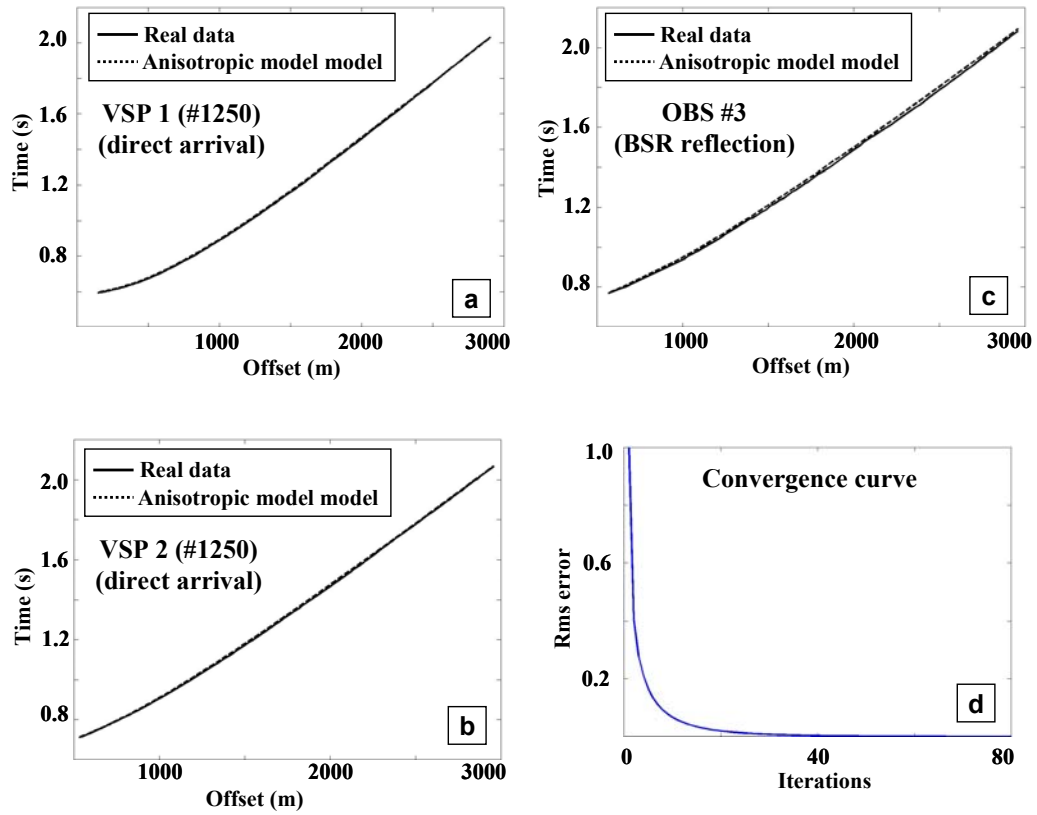
Figure 4.11. Data fitting at all offsets for the north profile from the VSP location for (a) VSP 1, (b) VSP 2, and (c) BSR (#3) recording. Convergence of the VFSA algorithm (d) shows the reduction of rms error values with respect to iterations.
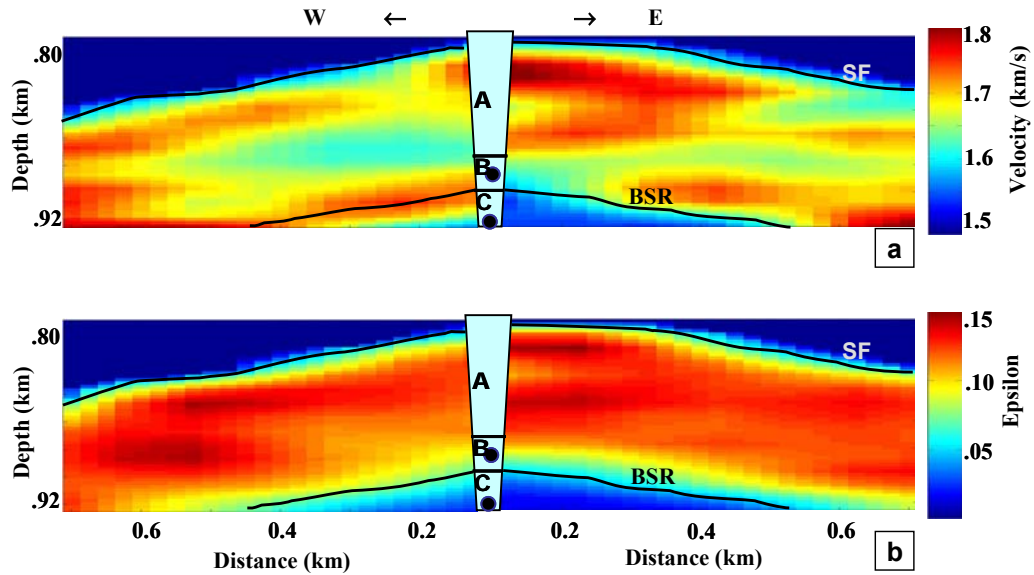
Figure 4.12. Anisotropic and heterogeneous (a) vertical P-wave velocity and (b) epsilon model (for un-rotated VTI medium) for W-E profile along w-VSP (#1250) traverse. VSP data at two depth locations (91 and 138 meters below seafloor) and an OBS (#3) data close to VSP site have been used in VSFA based traveltime inversion. Seafloor (SF) and BSR reflectors are marked on the models. Clearly the W-E profile is more heterogeneous than the S-N profile (Figure 4.11) at south summit. In figure, VSP receiver locations are marked with dots and depth profile is divided in three zones A, B, and C.
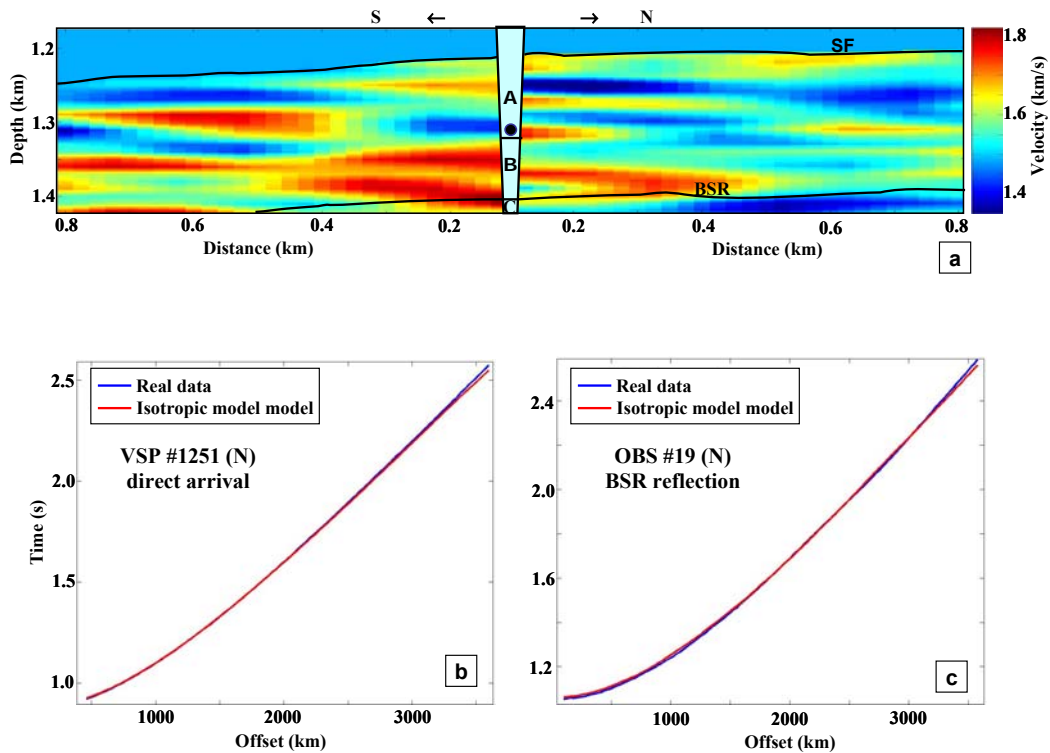
Figure 4.13. Isotropic and heterogeneous (a) P-wave velocity for S-N profile along w-VSP (#1251) traverse. Only one depth location for w-VSP at this site is available. VSP data at a depth location (98 meters below seafloor) and an OBS (#19) data close to VSP site have been used in VSFA based traveltime inversion. Seafloor (SF) and BSR reflectors are marked on the model. Data match is good at all offsets. It means slope basin side is isotropic and heterogeneous. Data matching at all offsets for north traverse from VSP location are shown for (b) VSP and (c) OBS. In figure (a), VSP receiver location is marked with dot and depth profile is divided in three zones A, B, and C.

4.6 INTERPRETATION OF THE RESULTS

We observed from the P-wave velocity profile (Figure 4.4) that the velocity is generally higher above the BSR which indicates the presence of gas hydrates. We also observe significantly lower velocity below BSR closer to the south summit which indicates the presence of free gas. However, towards the slope basin (E) we do not notice any decrease in P-wave velocity indicating an absence of free gas which is also suggested by the absence of strong BSR. Presence or absence of free gas will be established after S-wave analysis since S-waves are less affected by the presence of free gas.

Figure 4.4 shows lower P-wave velocity (lower than in water) near the south summit from seafloor down to a depth of about 50m which is possible if there is free-gas present along with gas-hydrate and/or due to the presence of unconsolidated sediments. Free gas can be present below the BSR (as inferred from the seismic data) and they can move along the fractures up to the seafloor and even leak into sea water (Suess et al., 2001; Riedel et al., 2001; Wang, 2003). If the gas saturation is high (and/or water salinity is high), free gas can be present with gas hydrates (Milkov et al., 2004). Thus, this velocity model is consistent with the interpretation of fluid flow through the fractures, and presence of shallow free-gas at the south summit.

The occurrence of anisotropy at the south summit is evident from the VSP data analysis, where the value of ε (P-wave anisotropy parameter) is negative because the vertical velocity is higher than the horizontal velocity. Negative values of ε are not observed for a VTI model (e.g., Thomsen, 1986; Vernik and

Liu, 1997; Wang, 2002). I therefore interpret that this represents an HTI model caused by the near vertically aligned fractures. The fracture (or small cracks) model is justified on the south summit of the Hydrate Ridge (section 4.1). Figure 4.14 shows fluid migration along fractures in a W-E seismic profile through south summit (Wang, 2003). The faults extend through the accreted sediments to the gas hydrate phase transition and may serve as pathways for methane to the sea floor (Suess et al., 2001). The fracture system in this environment is the result of tectonic activities (extensional force near summit) and hydrofractures created by the overpressured free gas present below the impermeable gas hydrate layers (that is below BSR). As methane gas (with other fluids) migrates up through fractures, gas hydrate can form in the shallow sediments in favorable thermodynamics condition resulting as hydrate veins (Figure 4.15).

Anisotropy study (HTI model) supports the presence of vertically aligned fractures, and hydrate veins are likely to be present at the south summit. Pecher et al. (2003) observed vertical transverse isotropy in the gas-hydrate bearing sediments on the Blake Ridge (BR), offshore South Carolina, and interpreted that the anisotropy is caused by partial alignment of clay particles and not hydrate (Jakobsen et al., 2000). BR (passive margin) and HR (active margin) belong to two different geological settings. I estimated a negative value of ε which can be explained by an HTI model likely caused by the vertical fractures. In the over saturation of free gas, fractures will contain free gas along with gas hydrates. Seismic anisotropy has been used to delineate fractures pattern with amplitude variation with offsets and azimuths analysis (Rüger, 1998).
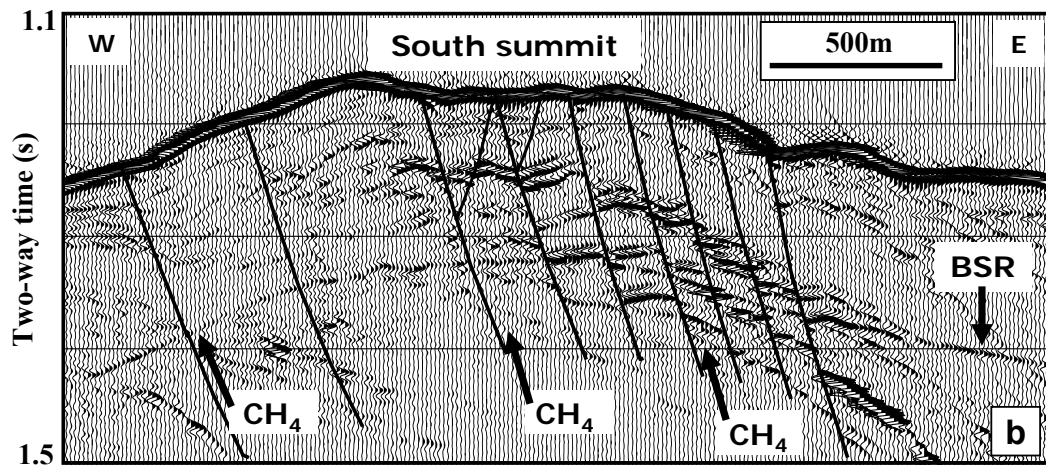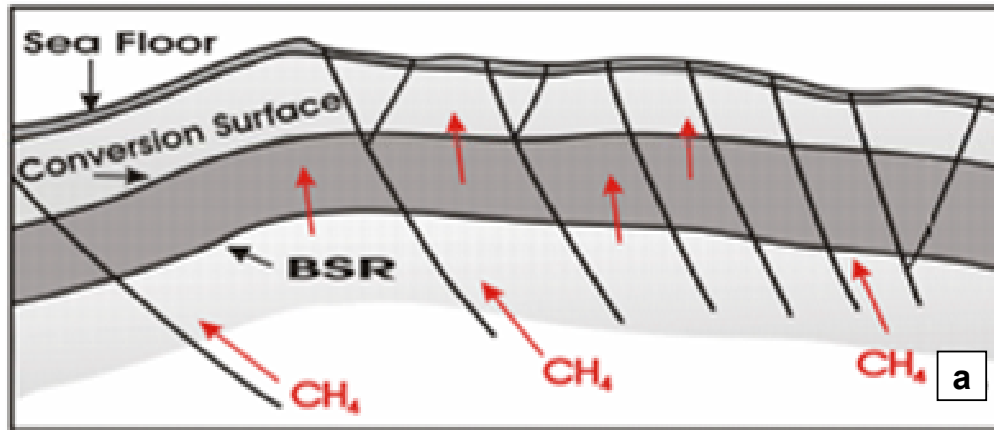
Figure 4.14. A fracture model on the south summit. A model shows major fractures and migration of methane gas (with other fluid) through fractures up to seafloor (a). This model is supported by a seismic section (b). Migrating gas will (partly) form gas hydrate in fractures in the gas hydrate stability zone (from seafloor to BSR). The hydrate forming in the fractures can be called hydrate veins and is possibly responsible for the HTI model (anisotropy). (Figures taken from Wang, 2003).
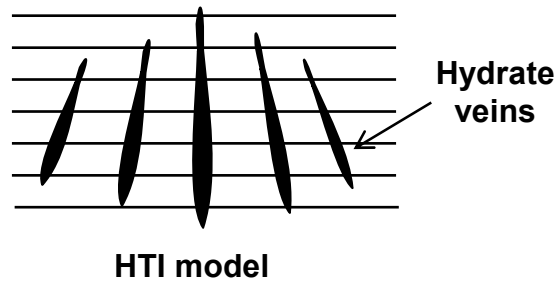
Figure 4.15. Hydrate vein model. Hydrates forming in vertical fractures will become hydrate veins. Vertical fractures (hydrate veins) may be causing the medium to be an HTI.

Profiles of anisotropic parameters across the summit will provide the spatial distribution of fractures. It is hard to quantify the fracture properties (density, size, shape and width) from the seismic data, but qualitative analysis is possible. The anisotropic parameter (epsilon) can be correlated to the fracture density (Kumar et al., 2004b), since anisotropy at this site is caused by the vertical fractures.

The anisotropic parameter estimation in section 4.4 was performed by observing the anomalies in traveltimes assuming homogeneous layers. Since lateral heterogeneity is one of the principal causes of the traveltime anomaly, it is generally difficult to isolate the effects of heterogeneity and anisotropy in the traveltime anomalies. This ambiguity has been reduced by parameter estimation for heterogeneous and isotropic model first, followed by a heterogeneous and anisotropic model. It is indeed true that my data can be modeled using a 2D isotropic model. However, such a model requires unrealistic velocity distribution.

The resulting subsurface model is divided into three zones (Figures 4.9, 4.10, 4.12, and 4.13): very shallow (layer A), above BSR (layer B) and below BSR (layer C). In general, the layer B represents relatively higher concentration of gas hydrates and layer C represents a free gas zone which is not well constrained with the available data. The P-wave velocity increases in the presence of gas hydrates and decreases in the free gas. Therefore relatively higher velocity is related to higher gas hydrate saturation and lower velocity is related to free gas (quantitative description in Chapter 5). P-wave anisotropic parameter (ε) is correlated to fracture density. Higher ε value can be related to higher fracture density.

In the S-N anisotropic model at the south summit (Figure 4.10), the velocity is relatively higher in the south than in the north similar to the isotropic model (Figure 4.9) signifying higher hydrate saturation in the south. Note that only 700m wide model at both sides of the VSP locations are shown because only these areas are covered by the ray propagation for about 3km of offsets covered on the surface (Figure 4.6). The P-wave anisotropy (ε) is smoothly varying in general; it is about 11% in layer A and 7% in layer B. It means anisotropy is stronger where hydrates are heterogeneously distributed (layer A) and lower in homogeneously distributed hydrate (layer B). In terms of fracture density (with correlation to ε), more fractures are present in the shallow part of the southern side. In the shallow fractured zone (layer A) hydrate concentration follows the fracture density.

The W-E velocity model (Figure 4.12) reveals that the W-E geology is more heterogeneous. Velocity is relatively higher in the east than in the west of the summit. P-wave anisotropy in layer A is about 15% and is about 10% in layer B.

Overall, at the south summit I observed weak anisotropy probably caused by the vertical fractures (caused by tectonic activities and hydrofractures developed by free gas trapped below the BSR). However, detailed quantification of the fracture parameters is not feasible with these seismic datasets.

Using a similar analysis on the slope basin side, the isotropic model matches the real data well which means this region is isotropic. This interpretation is consistent with the geological model, as there are not many fractures present in this region indicating little fluid migration. Hydrate concentration is relatively higher on the south than on the north side at this location.

4.6 SUMMARY

Interval P-wave velocity analysis is performed in the τ-p domain from south summit to slope basin side at the Hydrate Ridge. Velocity is higher above BSR and lower below the BSR, indicating the presence of gas hydrates and free gas, respectively. Free gas is concentrated towards the summit and is absent towards basin, which is also evident from the presence or absence of a continuous BSR. Near the summit from sea floor down to about 50m, lower P-wave velocity is observed which is interpreted to be caused by the presence of free gas along with gas hydrates.

Traveltime-error-contour analysis is performed for the estimation of 2D homogeneous P-wave anisotropic parameters. At the south summit, vertical velocity is found to be higher than the horizontal velocity which indicates an HTI model. Heterogeneity can also explain the observed velocity (or traveltime) anomaly; however for geologically consistent description of the subsurface and data-fitting anisotropy model is more valid. The HTI model is interpreted to be caused by the hydrate veins. Hydrate veins form when methane gas (with other fluids) migrates along vertically aligned fractures into the hydrate stability zone. In other words anisotropy is possibly caused by the vertical fractures. Vertical fractures are caused by tectonic activities and hydrofractures created by free gas trapped below the BSR to migrate up to the seafloor.

I developed a non-linear anisotropic traveltime inversion scheme for estimation of heterogeneous model using VSP and OBS data. In this scheme, forward modeling is performed with a traveltime computation method discussed in chapter 3 and inversion uses a VFSA algorithm. Initial model parameter is derived from the traveltime-error-contour analysis. Velocity and ε parameters are correlated with hydrate saturation and fracture density, respectively. South summit is found to be weakly anisotropic but slope basin side is isotropic.

Chapter 5: The Hydrate Ridge experiment:
Analysis of multicomponent data

5.1 INTRODUCTION

The Hydrate Ridge (HR) experiment during the summer of 2002 was focused on shear wave studies with the ultimate goal of estimating the distribution and saturation of gas hydrates and free gas. S-wave data in a marine environment are recorded with multicomponent receivers placed on the seafloor (OBS or OBC) and in a borehole (VSP); they record converted S-waves (PS-wave). Various possible applications of converted S-waves have been identified (e.g., Behle and Dohr, 1985; Garotta, 2000; Stewart et al., 2003) which include, structural imaging, subsurface fluid description, lithology estimation, anisotropy (fracture) analysis, and reservoir monitoring.

The two most common wave-conversion types are (Figure 5.1): 1) P-wave converts to S-wave during transmission at an interface (say, at the seafloor) and then propagates as S-wave (PSS- or SS-wave type), and 2) P-wave converts to S-wave at a reflector (reflected wave) and then propagates back as S-wave to the receiver (PS-wave type). There may be many more conversions from P- to S-wave (and vice-versa) during reflection and transmission at intermediate interfaces, but they are actually too weak to be significant (Stewart et al., 2002). For a layered earth model, SS-wave data can be analyzed in the same manner as the P-wave data (due to its symmetrical ray path). However, P- to S-wave conversion as a transmitted wave at the seafloor (or any other layer interface)

depends on the S-wave velocity below the conversion surface (compared to the P-wave velocity above interface). In the shallow subsurface, S-wave velocity at (or near) the seafloor is very low (100 to 300 m/s) unless there are some high velocity layers (e.g., carbonates and gas hydrates). In such a situation, P- to S-wave conversion during transmission is very weak. The PS-wave is better recorded than the SS-wave since it suffers less attenuation and is faster than the SS-wave. From now on, I will call PS-wave the S-wave unless otherwise specified.

The S-wave data analysis is complicated due to its mix wavetypes (P-wave from the source to the reflector and a converted S-wave from the reflector to the receiver). Unlike the PP- or SS-wave reflection paths, the S-wave reflection point (or conversion point) is not the midpoint between the source and the receiver at a level (Figure 5.1); it is closer to the receiver, and according to Snell's law, resulting in an asymmetric ray path. For closely spaced receiver data (like in OBC), they may be sorted as common conversion point (CCP) gathers for S-wave analysis (Tessmer and Behle, 1988). However, for sparse receivers (like in OBS), CCP sorting is not practical and common receiver gathers will be used in the analysis, where each trace corresponds to a different shot.

In this chapter, I discuss various steps for processing of multicomponent seismic data (OBS and VSP) for S-wave interval velocity analysis (Figure 5.2). Then, I estimate gas hydrate saturation using P- and S-wave velocity profiles by matching the theoretical velocities (appendix E) to the estimated velocities.
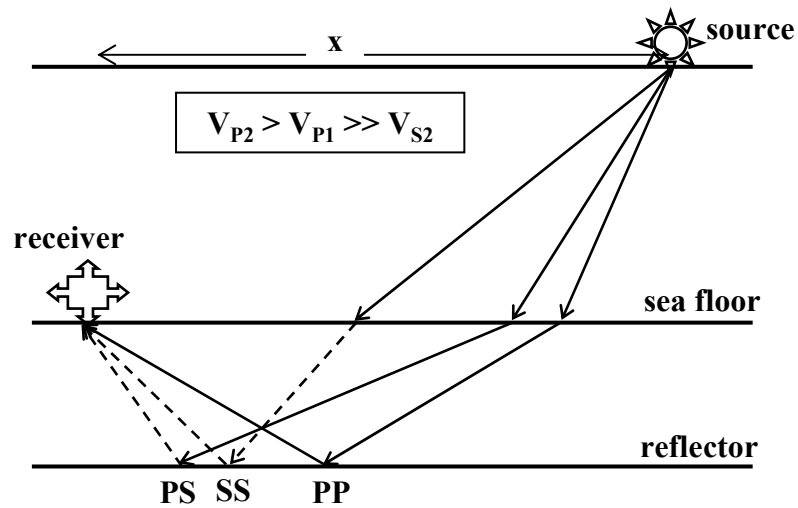
Figure 5.1. Ray paths of PP-, SS- and PS-waves (following Snell's law) for an OBS (or VSP) geometry. PP- and SS-waves have symmetric ray paths in the second layer but it is asymmetric for PS-wave. The P- and S-wave paths are shown with solid and dashed lines, respectively.

Preprocessing

(Figure 5.3)

↓

P-wave velocity analysis

(section 4.3)

↓

PP- to PS-wave data correlation

(section 5.3.1)

↓

S-wave velocity analysis

(section 5.3)
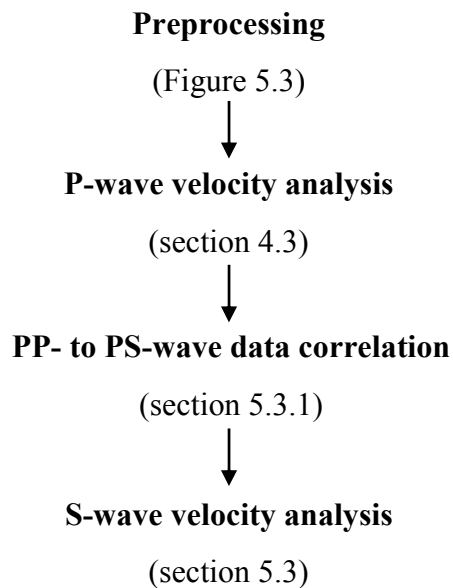
Figure 5.2. Steps for S-wave velocity analysis using multicomponent data.

5.2 PROCESSING OF MULTICOMPONENT SEISMIC DATA

Seismic data processing starts with quality control of the recorded data. Over the years, the technology for recording of multicomponent data has greatly improved (Caldwell, 1999). In multicomponent seismic data processing (Zhu et al., 1999), it is assumed that the seafloor coupling (borehole coupling in the VSP) is good so that the geophones respond to the true wave motion (Garmany, 1984), resulting in good vector fidelity; i.e., geophones respond isotropically to an incoming seismic energy (Dellinger et al., 2001). Recorded raw data are corrected for various recording effects and converted to a standard (segy) format which can be called preprocessed data. Figure 5.3 shows the preprocessing steps of OBS data recorded on an UTIG instrument. During the Hydrate Ridge experiment, preprocessing for UTIG OBS data was performed mostly on-board the seismic ship. Nakamura et al. (1987) provide detailed discussion of OBS instruments and the inversion process to locate and orient the instrument. Preprocessing of the VSP data was performed on-board the drilling ship. There is a 53 ms time delay in the w-VSP data. After preprocessing these data are ready for further processing.

In multicomponent data recording, hydrophones record P-waves (pressure sensitive) and three geophones record both P- and S-waves. However, the vertical component geophones primarily record P-waves while the horizontal components record S-waves. During data recording the orientation of horizontal receivers are not known and both the receivers record S-waves. They are trigonometrically rotated to radial and transverse components to maximize the S-wave energy on the radial component.

113

Raw data

(anti-alias frequency is 50Hz for
geophones and 80Hz for hydrophone)

↓

Apply navigation data

(Bathymetry and ship's position and heading)

↓

Raw shot files

(Shot times, shot coordinates, and navigation)

↓

Clock correction and convert to segy file

↓

Locate and orient horizontal components of the OBS instrument

(by inversion of arrival time and relative amplitude)

↓

Final 4-C segy file

(4C: first is vertical, fourth is hydrophone,
second and third are two horizontals)

Figure 5.3. Preprocessing of OBS data recorded on UTIG instruments. Processing
was done using in-house software named "OBSTOOL". Final data
are in segy format. Two horizontal components are rotated as radial
and transverse components for S-wave analysis with radial data.

5.2.1   ROTATION OF 2-C HORIZONTAL DATA

After preprocessing, the data from two horizontal-component geophones (2-C) are numerically rotated into radial and transverse components. There are two conventions for rotation of the horizontal components: 1) source-centered vector coordinates (Gaiser, 1999) which measure positive signal pointing away from the source, and 2) acquisition rectangular coordinates (Brown et al., 2002) which follow a reference frame such as the shooting line. The first method is more general and the rotated data are radial and transverse components; a radial component does not show any polarity reversal on two sides of receivers. The second method is good for 2D recording geometry and rotated data are inline (oriented in source-receiver plane) and crossline components (perpendicular to inline), where inline component shows polarity reversal on the two sides of receivers. In the second method, the polarity of traces on one side is reversed to make the first arrival on inline component invariant. Both the methods are equivalent in 2D recording. It is worthwhile to note that my data (OBS and w-VSP) are recorded with a 2D geometry (Figure 4.2).

For the rotation of horizontal component data, orientations of the horizontal receivers are required which can be estimated either with an inversion analysis on the direct arrival data (e.g., Nakamura et al., 1987) or with a more commonly used process called polarization diagram (Hodogram plot) analysis (Winterstein and Meadows, 1991). A polarization diagram (Hodogram) is a plot of 3D particle motion projected onto the horizontal plane. It gives the orientations

of the horizontal components, which are used to rotate the horizontal components (H_1 and H_2) to a radial and a transverse component perpendicular to radial.

Hodogram plot analysis assumes that the P- and S-waves are linearly polarized. It can be plotted using 2-C OBS or VSP data. Here I use an OBS data (S-N profile over OBS #19) to explain the analysis. Figure 5.4 shows a Hodogram plot, where the first arrival waveforms (say, 10 time samples) of corresponding H_1- and H_2-component traces are plotted on a 2D plane. I plot two traces, one from each side of the receiver (a negative and a positive offset trace) to derive a better trend. It results into a linear trend (Figure 5.4) which suggests good vector fidelity in the data. This trend gives the polarization direction of direct P-wave and is approximately the shot direction with respect to horizontal receivers. In this example, the shooting direction makes an angle of 33^0 with H_1-receiver; therefore the inline and crossline components are found by rotation of H_1- towards H_2- component (counter-clockwise) by 33^0 angles using a simple matrix relation

$$\begin{bmatrix} inline \\ crosline \end{bmatrix} = \begin{bmatrix} \cos\theta & \sin\theta \\ -\sin\theta & \cos\theta \end{bmatrix} \begin{bmatrix} H_1 \\ H_2 \end{bmatrix}, \tag{5.1}$$

where θ (33^0) is the rotation angle (DiSiena et al., 1984).

Figure 5.5 shows the result of 2-C rotation of an OBS dataset. In an isotropic layered medium, inline (or radial) component contains maximum shear-wave energy, and crossline (or transverse) component has minimum shear energy (Zhu et al., 1999). Abnormal energy left in the transverse component is an indication of heterogeneity and anisotropy.

116
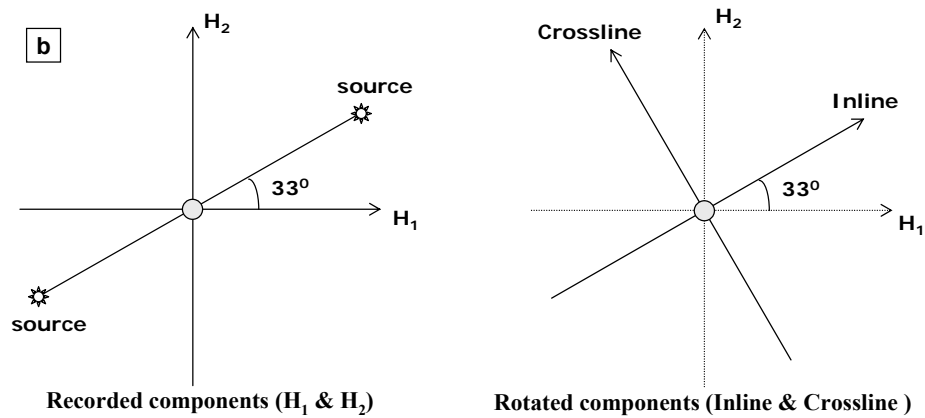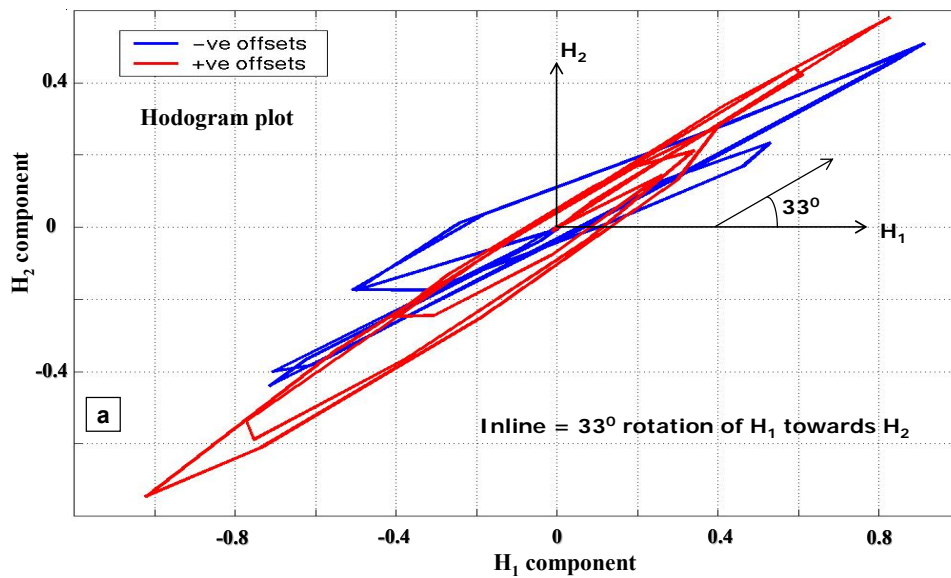
Figure 5.4. Hodogram plot: Relative amplitudes of direct arrival waveforms of two horizontal components (H_1 and H_2) are plotted on a 2D plane (a). A linear trend gives the shot direction. Here, the shooting direction makes an angle of 33^0 with respect to the H_1-component receiver (b), which is the rotation angle. The Inline and crossline components are found (Figures 5.5 b and c) by rotating H_1 towards H_2 by 33^0.

117
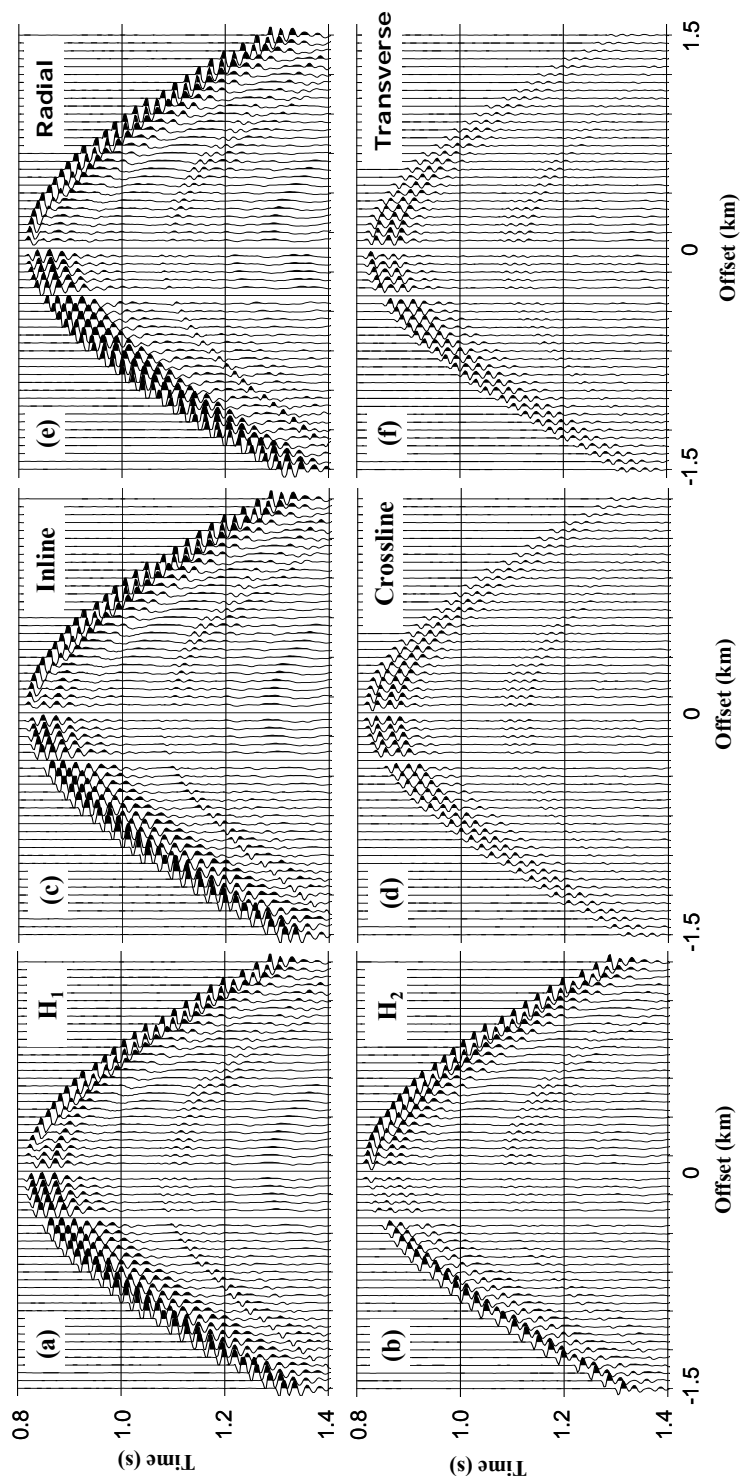
Figure 5.5. Rotation of the horizontal components of OBS #19 for an S-N profile. Recorded horizontal components (a and b) are rotated as inline (c) and crossline (d) components using hodogram analysis (Figure 5.4) and they (a and b) are also rotated as radial (e) and transverse (f) components using OBSTOOL (source-centered vector coordinates). Note the polarity reversal on inline component (c) but the same polarity on radial component (e).

118

5.3 SHEAR WAVE VELOCITY ESTIMATION: THE $\tau - p$ APPROACH

Similar to P-wave velocity analysis (section 4.3), I performed S-wave velocity analysis in the τ-p domain. The τ-p trajectory of a converted S-wave (PS-wave) in an isotropic medium (Figure 5.1) is given by

$$\tau_{PS}(p) = \tau_P^0 \sqrt{1 - p^2 v_P^2} + \tau_S^0 \sqrt{1 - p^2 v_S^2} , \qquad (5.2)$$

where τ_P^0 and τ_S^0 are one-way vertical traveltimes, and v_P and v_S are the velocities of P- and S-waves, respectively. It is evident from equation (5.2) that for S-wave, incident and reflected times correspond to a P- and an S-wave traveltimes, respectively. Mukherjee (2002) (equation 2.24) presents an extension of this equation to an anisotropic medium. Examples of τ-p analysis for converted waves can be found in Wang (2003). In an ocean-bottom recording (OBS), the first arrival is a direct P-wave (one-way P-wave traveltime) and it must be taken care of when using the above equation (5.2) in data analysis. The steps for the interactive interval S-wave velocity analysis assuming locally 1D isotropic media are as follows:

1. Input data are radial component data in τ-p domain, and P-wave interval velocity (v_P) from previous chapter (4).

2. Correlation of PP- and PS-wave events on hydrophone (or vertical) and radial component data, respectively (section 5.3.1).

3. Select a reflection event, then τ_P^0 and τ_S^0 are known for this reflector and the only unknown is now v_S (equation 5.2).

119

4. Interactively pick an S-wave velocity (v_S) for the selected PS-wave event for which τ-p traveltime trajectory (equation 5.2) matches the data.

5. An output from step 4 is the S-wave interval velocity for a selected reflection event. Depth of this layer can be estimated using the known velocity (v_S) and vertical traveltime (τ_S^0).

6. Repeat steps 3 to 5 for each reflection event in a top-down fashion.

7. Final output is a 1D S-wave interval velocity model in depth.

8. Reflector depth from S-wave analysis shall match depth values from P-wave analysis, if not then change the PP- and PS-wave event correlation and/or velocities and repeat the process.

The picked velocity is used in the NMO application to check the correctness of velocity (for correct velocity the reflection event should be flat after NMO). The velocity analysis outline here assumes a 1D isotropic medium, and therefore NMO application may not be perfect for the far offset data (Yilmaz, 2001). Most of the steps in the above velocity analysis work flow are trivial except step 2 comprising the correlation of P- to S-wave reflection events which I describe next.

5.3.1 CORRELATION OF PP- AND PS-WAVE DATA

There is no rule of thumb for PP- to PS-wave reflection event correlation which is a crucial step in converted S-wave velocity analysis. I use synthetic seismograms and traveltime tables for PP- and PS-waves event correlation. The task in P- to S-wave reflection event correlation is to find an S-wave reflection event on the radial component corresponding to a P-wave reflection event on the hydrophone (or vertical geophone) data. The reflection events for P- and S-waves will appear on seismic time sections at different arrival times since they propagate with different velocities. They should, however, be at the same location in depth. I perform the correlation with the help of seismic modeling in three steps. The first step is to make a velocity model in depth and calculate the arrival times for different wavetypes for the given acquisition geometry, the second step is to generate synthetic seismograms and identify different wavetypes at the estimated arrival times, and the third step is to match the synthetic data with the real data and identify a PS-wave arrival corresponding to a PP-wave arrival.

As shown in Figure 5.1 for OBS (or VSP) geometry, different wavetypes follow different wave paths for a given source-receiver offset. For a known velocity model in depth, it is possible to estimate the arrival times of various wavetypes (Figure 5.6). The velocity model can be built either from sonic logs or from a P-wave velocity profile and guess values for S-wave velocity from other sources. Figure 5.6 highlights the arrival times of different wavetypes for a reflector (BSR) for a VSP geometry using the velocity model derived from sonic logs. These traveltime tables help identify different arrivals on the seismograms.

A traveltime table for various wavetypes (Figure 5.1)

Depth (m)	Vp (km/s)	Vs (km/s)	PP-time (s)	PS-time (s)	SS-time (s)
796.0000	1.5000000	1.50000000	0.5280000	0.5280000	0.5280000
845.9699	1.5274768	0.27312305	0.5633327	0.5633327	0.7256028
853.8947	1.5524693	0.27312305	0.5684964	0.5684964	0.7546184
859.8383	1.5504305	0.27312305	0.5723575	0.5723575	0.7763800
861.8195	1.5986460	0.27379230	0.5735968	0.5735968	0.7836162
863.8007	1.5896308	0.28461540	0.5748431	0.5748431	0.7905771
865.7819	1.5550538	0.27643847	0.5761171	0.5761171	0.7977440
867.7631	1.5571153	0.27639234	0.5773895	0.5773895	0.8049120
869.7443	1.5626462	0.28827694	0.5786574	0.5786574	0.8117845
873.7066	1.5615770	0.28516152	0.5812117	0.5812117	0.8257035
875.6878	1.5411770	0.28563848	0.5824972	0.5824972	0.8326396
883.6127	1.5322230	0.34226924	0.5889205	0.5934158	0.8630076
885.5939	1.5216153	0.32674616	0.5915245	0.6007813	0.8751345
893.5187	1.5986463	0.31489230	0.6015602	0.6288516	0.9212394
895.4999	1.6014308	0.32779231	0.6040345	0.6361329	0.9333275
897.4811	1.6379384	0.31942307	0.6064536	0.6435449	0.9457324
899.4623	1.5985768	0.35723072	0.6089324	0.6503302	0.9568244
901.4435	**1.5069155**	**0.32556152**	**0.6115618**	**0.6577305**	**0.9689954**
903.4247	1.5428771	0.32549226	0.6141300	0.6651014	0.9811690
905.4059	1.5305307	0.33209994	0.6167189	0.6723615	0.9931003
907.3871	1.5581152	0.35369232	0.6192620	0.6792345	1.0043033
913.3307	1.5143846	0.32865384	0.6270675	0.7016620	1.0413529
919.2743	1.5267462	0.37236154	0.6348546	0.7222591	1.0747601
927.1991	1.5266691	0.34083077	0.6452170	0.7499209	1.1197212

Figure 5.6. A traveltime table for VSP (#1250) geometry with a velocity model derived from sonic logs. The traveltimes of various wavetypes for a reflector (at a depth of 901m) are highlighted. This table helps identify different wavetypes in a seismogram.

The PP- to PS-wave event correlation can be performed in the offset-time (x-t) domain and/or the τ-p domain. I will show two examples of correlation with real data from the Hydrate Ridge (Figure 1.4), one from the south summit (VSP 1250 and OBS 3) and one from the slope basin side (VSP 1251 and OBS 19). The synthetic seismograms required in this analysis are generated using a reflectivity method (Kennett, 1983). The direct arrival response in the synthetic seismogram has been excluded to boost (isolate) the energy of the reflection events.

I generated VSP synthetic seismogram (Figure 5.7) and identified a reflection event (BSR) using the traveltime table (Figure 5.6). Figure 5.8 shows matching of PP- to PS-wave event on the VSP data from the summit at site 1250. An OBS station is available near by this VSP site, so for OBS geometry I created a traveltime table and identified an S-wave reflection event on the radial component corresponding to a P-wave reflection event on the hydrophone. Figure 5.9 shows the matching of events and moveout on the radial component between real and synthetic data, and Figure 5.10 shows the final correlation of P- to S-wave reflection events on the OBS data from the south summit.

I follow similar steps on the slope basin side. Figure 5.11 shows the identification of PS-wave events on the radial component OBS data and matching of events and moveout between real and synthetic data. Finally, Figure 5.12 shows the correlation of P- and S-wave reflection events on hydrophone and radial component geophone data from S-N profile over OBS (#19). It is possible that the S-wave response is weak for some events if P- to S-wave conversion is weak in which case interpretation with modeling helps with phase identification.

123
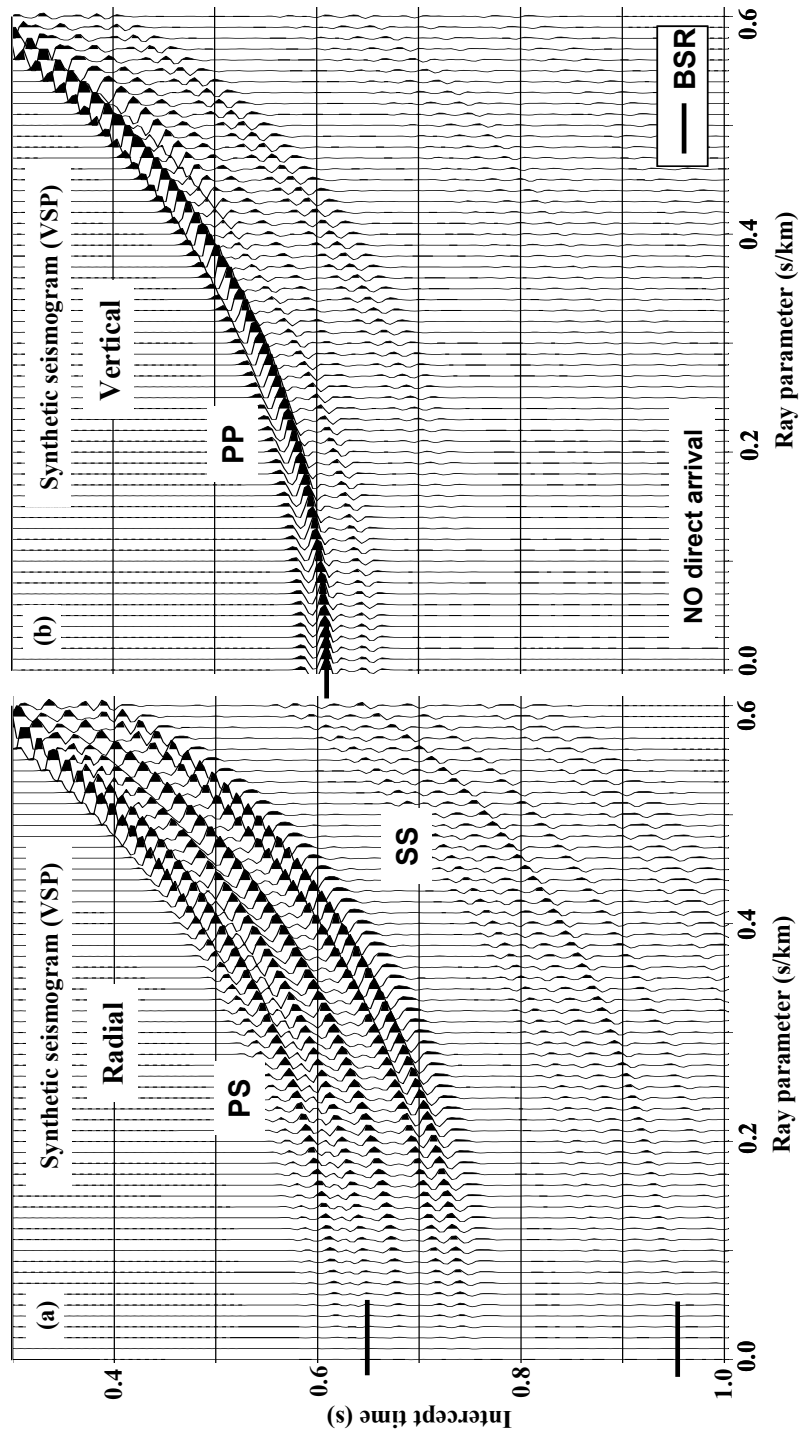
Figure 5.7. VSP synthetic seismograms in τ-p domain, and correlation of PP-to PS-wave event for a reflection (BSR) on the vertical (b) and the radial (a) component data, respectively, using a traveltime table shown in Figure 5.6. Direct arrivals are excluded from the data to boost the normalized amplitudes of the reflection events.
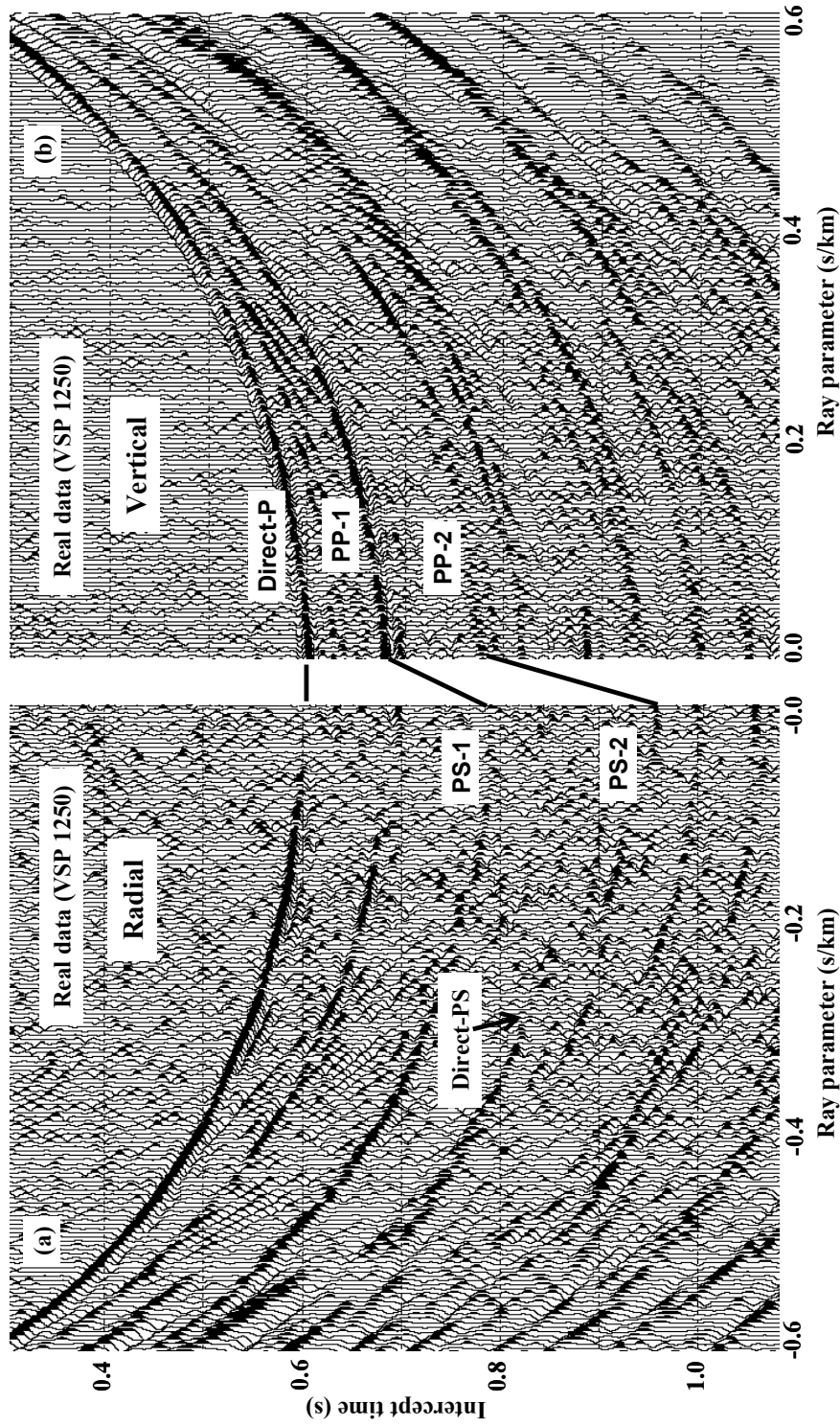
Figure 5.8. VSP data in τ-p domain from N-S profile at site 1250 with a receiver at a depth of 91m below sea floor. The P- to S-wave event correlations for two reflections are shown using the traveltime table and also correlating real data with synthetic seismogram. A direct arrival PS-wave event is also marked.
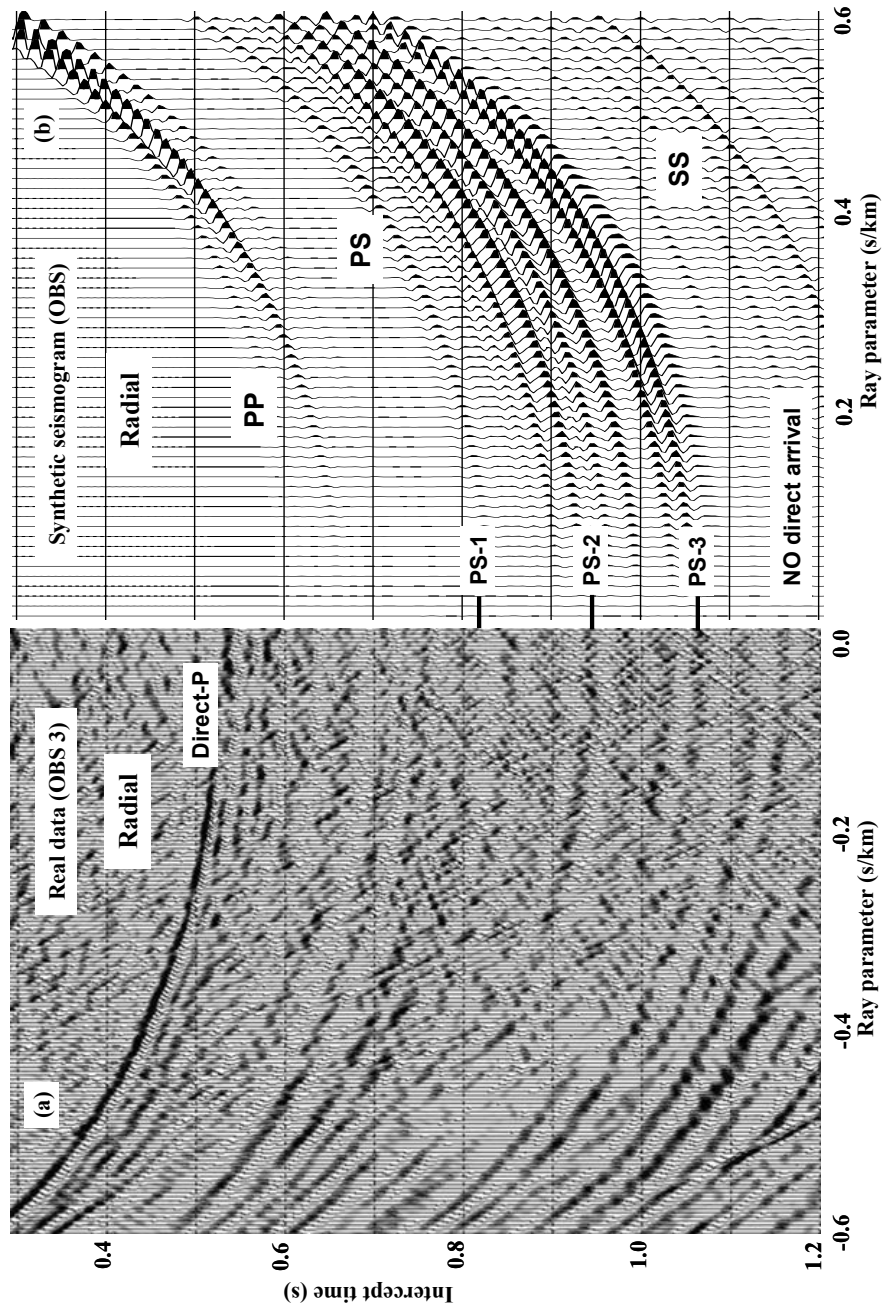
Figure 5.9. Matching events and moveout on the radial component synthetic and real data in the τ-p domain for an S-N profile over OBS station 3. Three PS-wave events shown here correspond to three P-wave events on the hydrophone data.

126
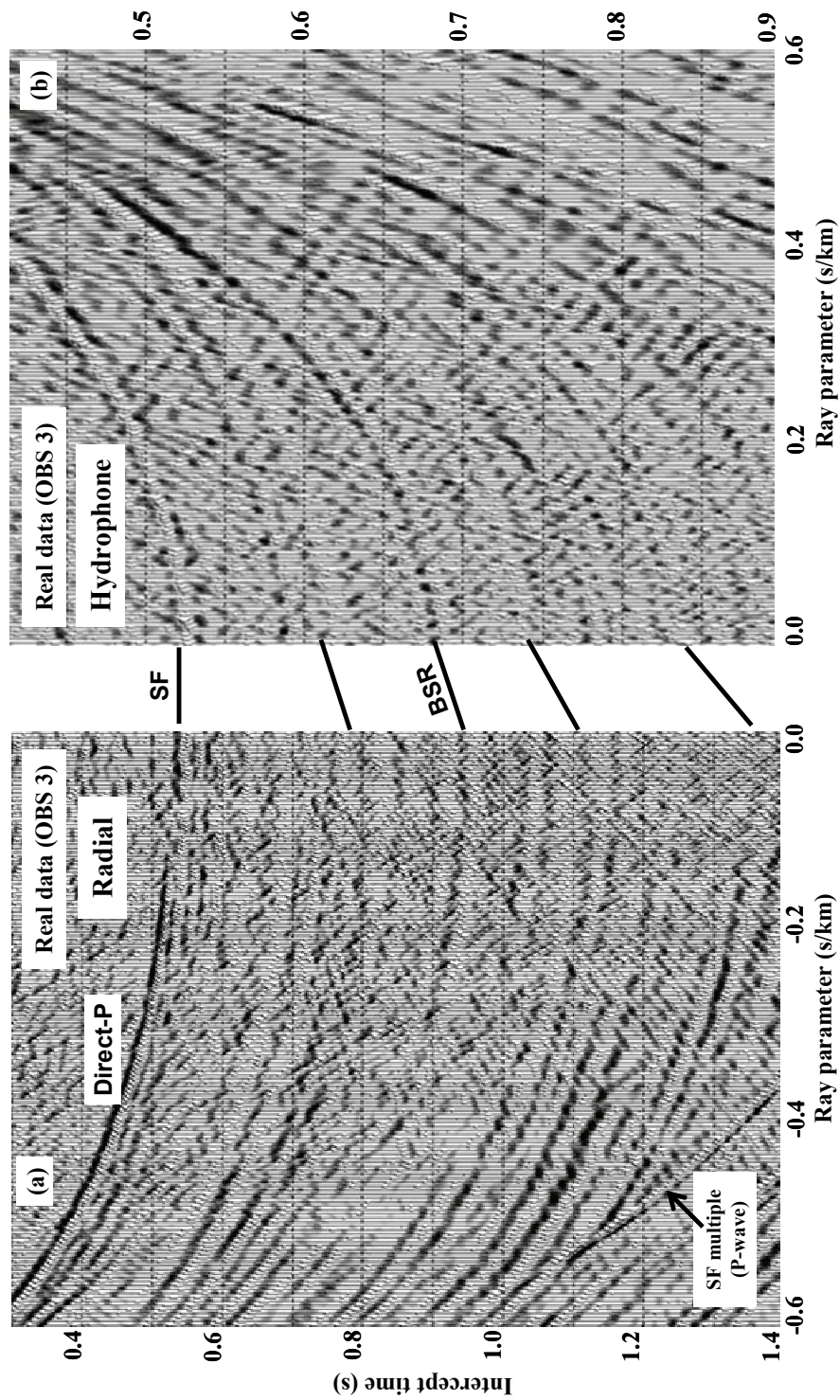
Figure 5.10. PP- to PS-wave events correlation on an S-N profile OBS (#3) data at the south summit. Five events are correlated including direct arrival marked as SF (seafloor). The ratio of P- and S-wave velocities varies from 5 near the SF to 4.2 near the fourth reflector.

127
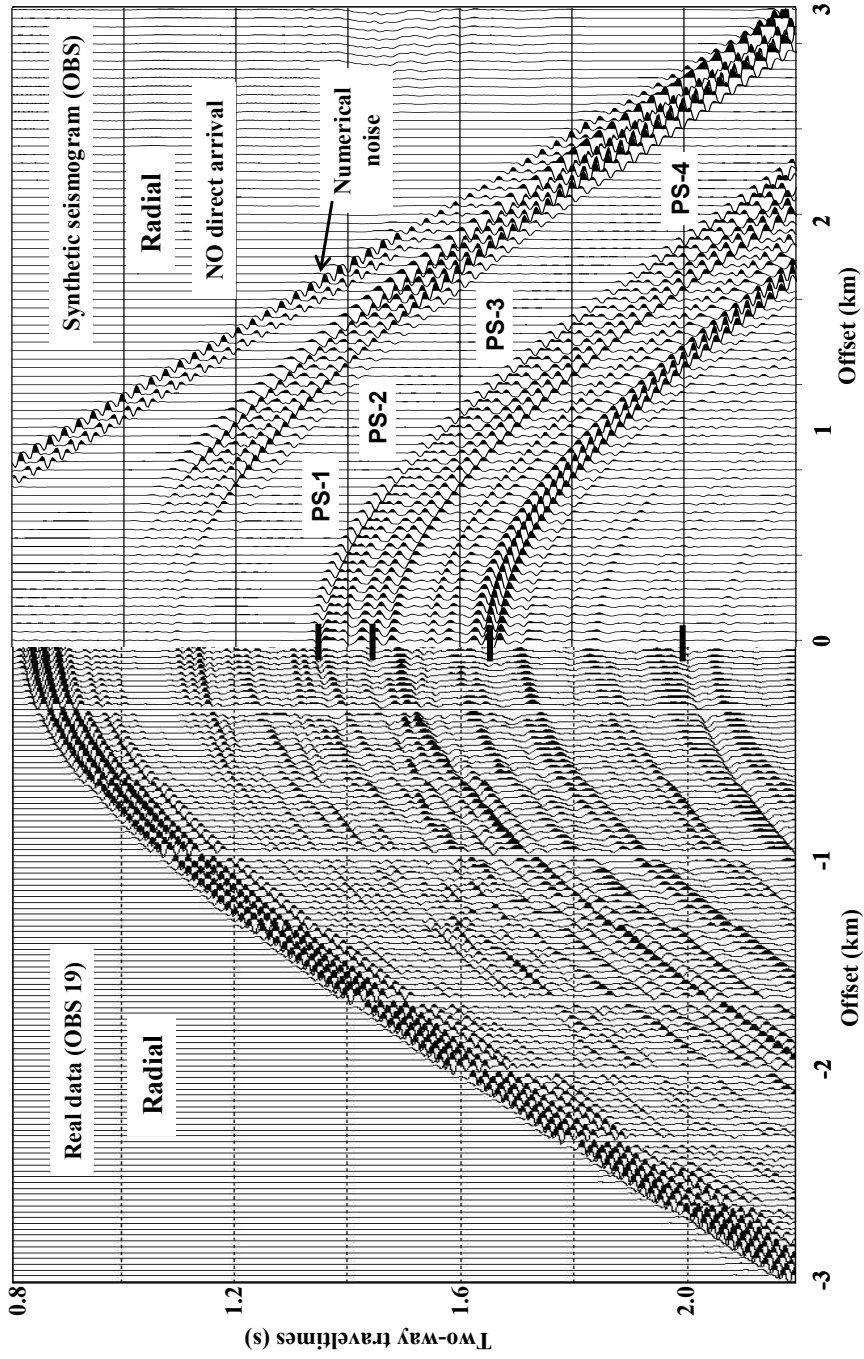
Figure 5.11. Matching events and moveout on the radial component synthetic and real data in the x-t domain for a S-N profile over OBS station 19. Four PS-wave events shown here correspond to four P-wave events on the hydrophone data. Direct arrival data are not included in synthetic data, and numerical noise is due to leakage in τ-p to x-t conversion.

128
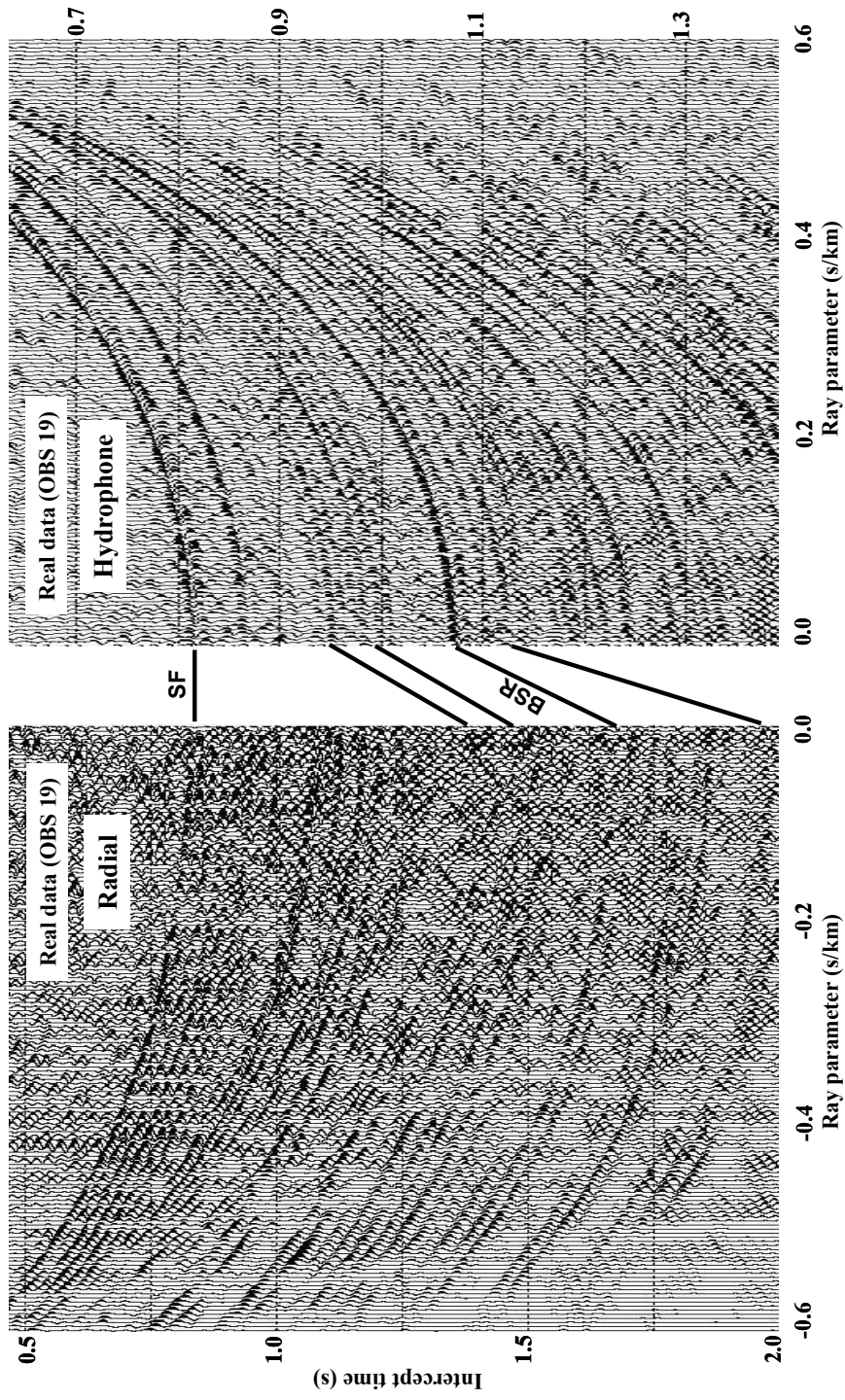
Figure 5.12. PP- to PS-wave events correlation on an S-N profile OBS (#19) data at the slope basin side. Five events are correlated including direct arrival marked as SF (seafloor). The ratio of P- and S-wave velocities varies from 6.8 near the SF to 4.8 near the fourth reflector

5.4 SHEAR WAVE SECTION AND VELOCITY STRUCTURE

The S-wave velocities are estimated first at the south summit and the slope basin sites where VSP, OBS, and sonic logs are available. The S-wave velocity analysis at these two locations is constrained by the available sonic logs. First PP- and PS-wave events are identified on the hydrophone and the radial component (OBS) data, respectively, and then S-wave velocity is estimated as explained in section 5.3. Once velocity analysis at these two locations (south summit, OBS 3; and slope basin, OBS 19) are complete, analysis at the intermediate (and neighbor) locations are performed where only the OBS data are available (Figures 1.4 and 4.3). Estimated interval P- and S-wave velocities are used for NMO correction and conversion of OBS data from time to depth to match the reflectors on P- and S-wave sections in depth domain.

Figures 5.13 and 5.14 compare the P- and S-wave depth sections derived from the OBS data from the south summit and the slope basin side, respectively. OBS data (receiver gathers) were first corrected for normal moveout (i.e., NMO correction) in the τ-p domain using estimated velocity and then converted to depth. The velocity profiles derived from velocity analysis (in red) and dipole sonic logs (in blue) have been superimposed on the OBS data. Note that sonic logs are not available up to the horizon 'A' at the south summit (Figure 5.13) for which lower P-wave velocity is estimated and up to the BSR level at the slope basin site (Figure 5.14) for which higher velocities for both P- and S-wave are estimated. Also rms velocities in two horizons are estimated from the interval

velocity for sonic logs and plotted as constant velocity (in blue) to compare with the calculated velocity (in red) (Figures 5.13 and 5.14).

To match the reflectors identified on the OBS data with the reflectors on the streamer data, I superimposed the P- and S-wave OBS data (from Figures 5.13 and 5.14) on the streamer data (Figure 5.15) in depth domain. BSR reflection event is marked on the streamer data to match with that on OBS data. Similarly, S-wave velocity analysis at other OBS stations are performed which gives the S-wave section (radial component data) and the 1D S-wave velocity models in depth at the corresponding OBS sites. Figure 5.16 shows the S-wave section in depth (radial component data after NMO correction and converted to depth) superimposed on the streamer data. Five reflection events (including seafloor) are interpreted on OBSs data and streamer data sections in depth (Figure 5.16). Once 1D velocity at the respective OBS locations is known, they are interpolated and smoothed (vertically and horizontally) to produce a 2D velocity profile. Figure 5.17 shows the W-E profiles (from summit to slope basin) of P- and S-wave velocity. OBS stations are marked on the seafloor (of P-wave velocity section) where velocity analysis is performed. Since seafloor tomography is not horizontal the dip of the topography is considered during lateral smoothing. Next I will discuss the correlation of these seismic velocities to the gas hydrate saturation.
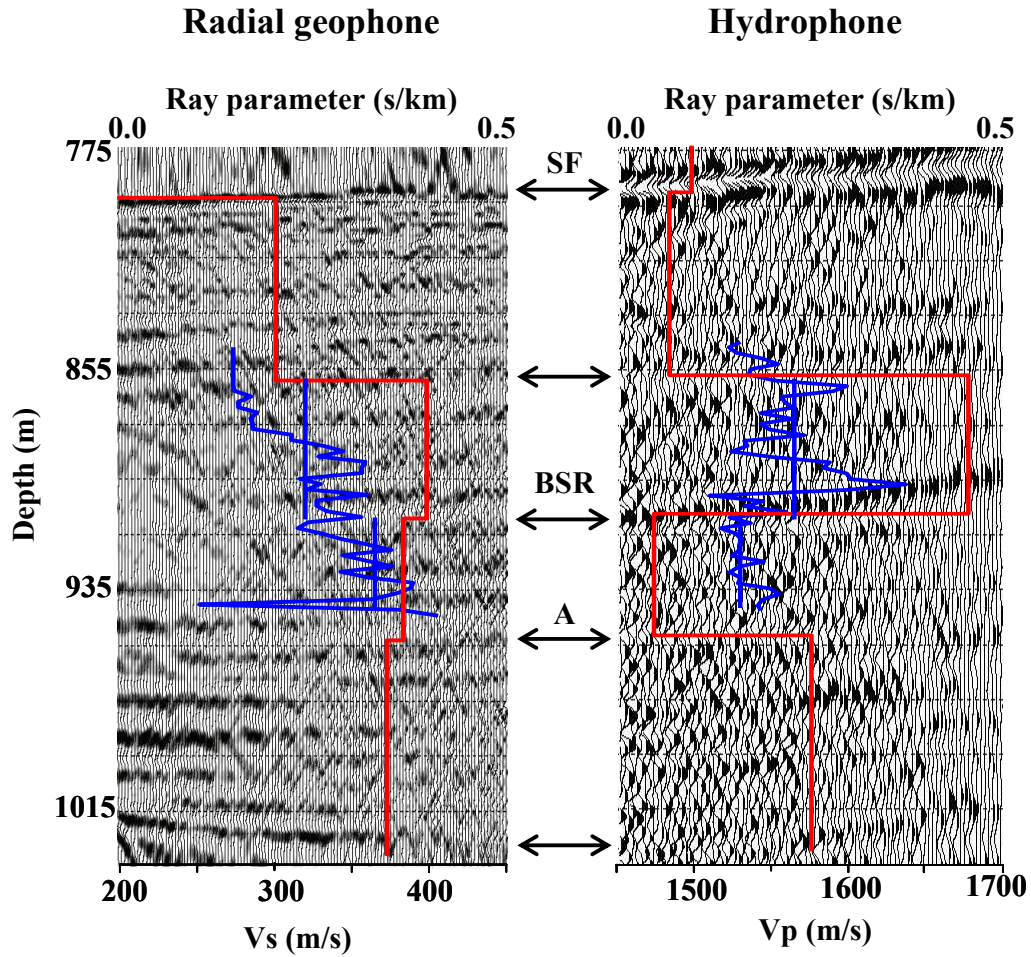
Figure 5.13. Radial geophone (left) and hydrophone (right) data (in the τ-p domain) from OBS (#3) after NMO correction in time and converted to depth. Seismic velocities are overlaid on the seismic section (V_S on radial geophone and V_P on hydrophone data). Seismic velocities estimated from velocity analysis (in red) are compared with velocities derived from sonic (V_P) and dipole sonic (V_S) logs (in blue). Vertical blue lines represent rms velocity from sonic logs (marked in two depth layers). All the reflectors (marked with arrows) are matching well in depth.
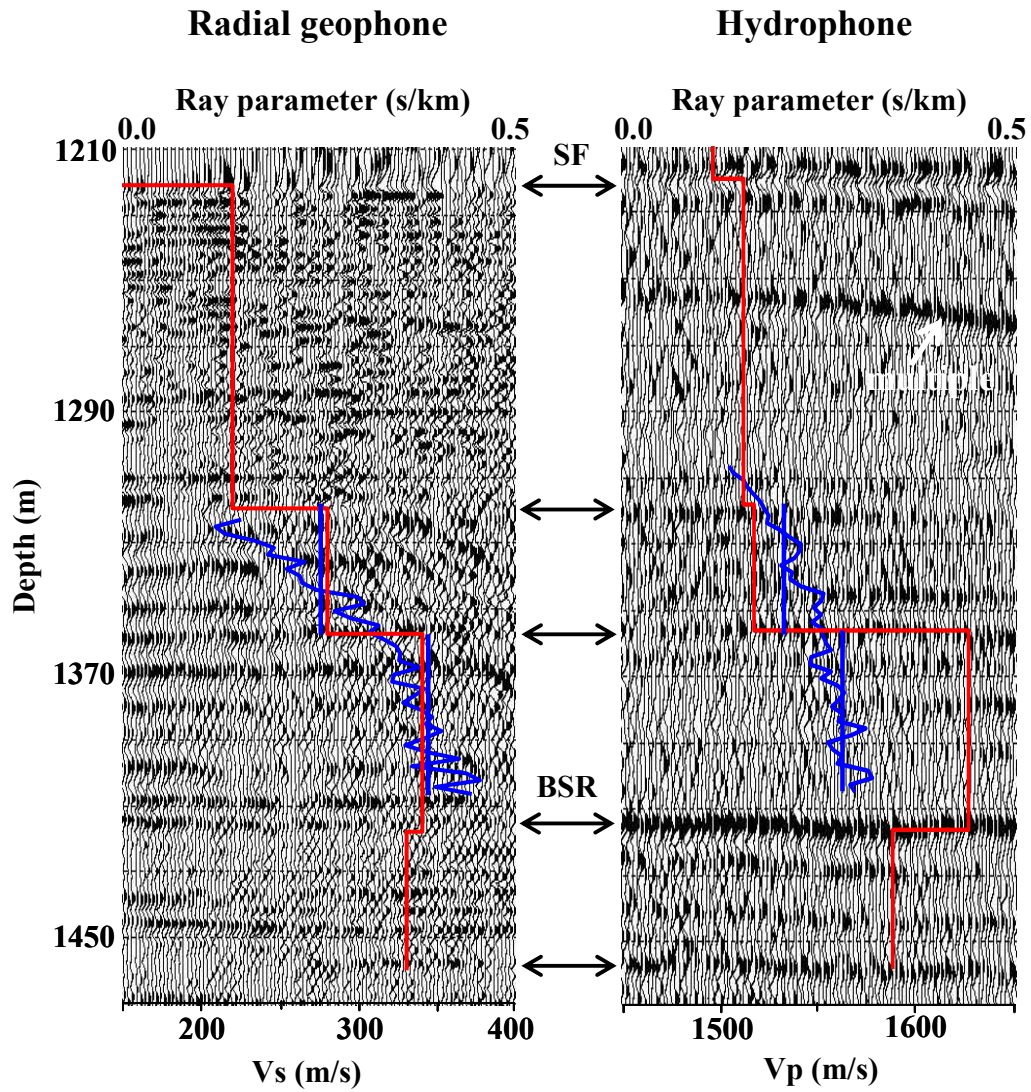
Figure 5.14. Radial geophone (left) and hydrophone (right) data (in the τ-p domain) from OBS (#19) after NMO correction in time and converted to depth. Seismic velocities are overlaid on the seismic section (V_S on radial and V_P on hydrophone data). Seismic velocities estimated from velocity analysis (in red) are compared with velocities derived from sonic (V_P) and dipole sonic (V_S) logs (in blue). Vertical blue lines represent rms velocity from sonic logs (marked in two depth layers). All the reflectors (marked with arrows) are matching well in depth. "Multiple" event on the hydrophone is caused probably by bubbles.

133
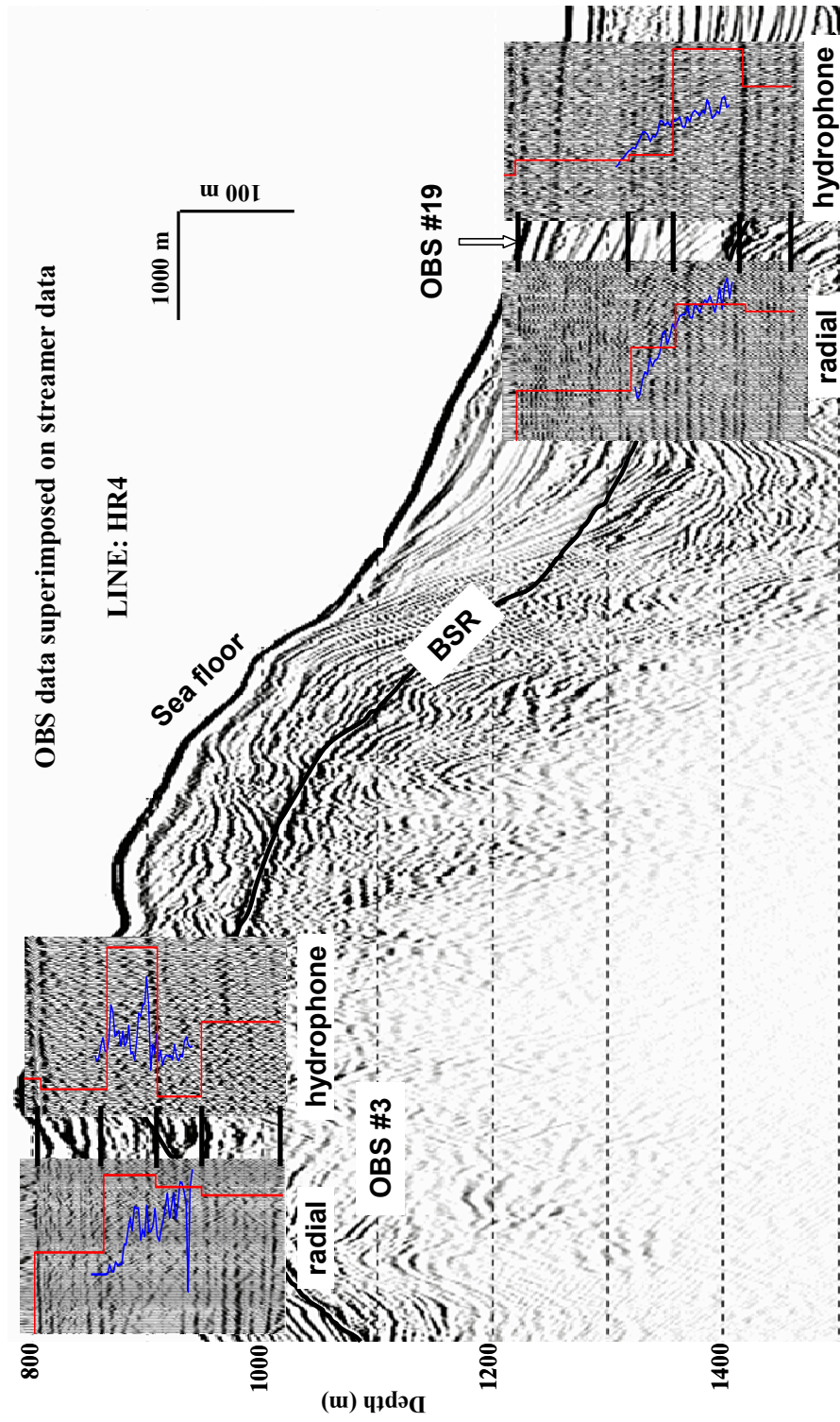
Figure 5.15. NMO corrected OBS data (in the τ-p domain with p ranging from 0 to 0.5 s/km) in depth, along with the velocity profiles derived at the south summit and at the slope basin side, are superimposed on the depth converted streamer seismic data for correlation of reflector depths.

134
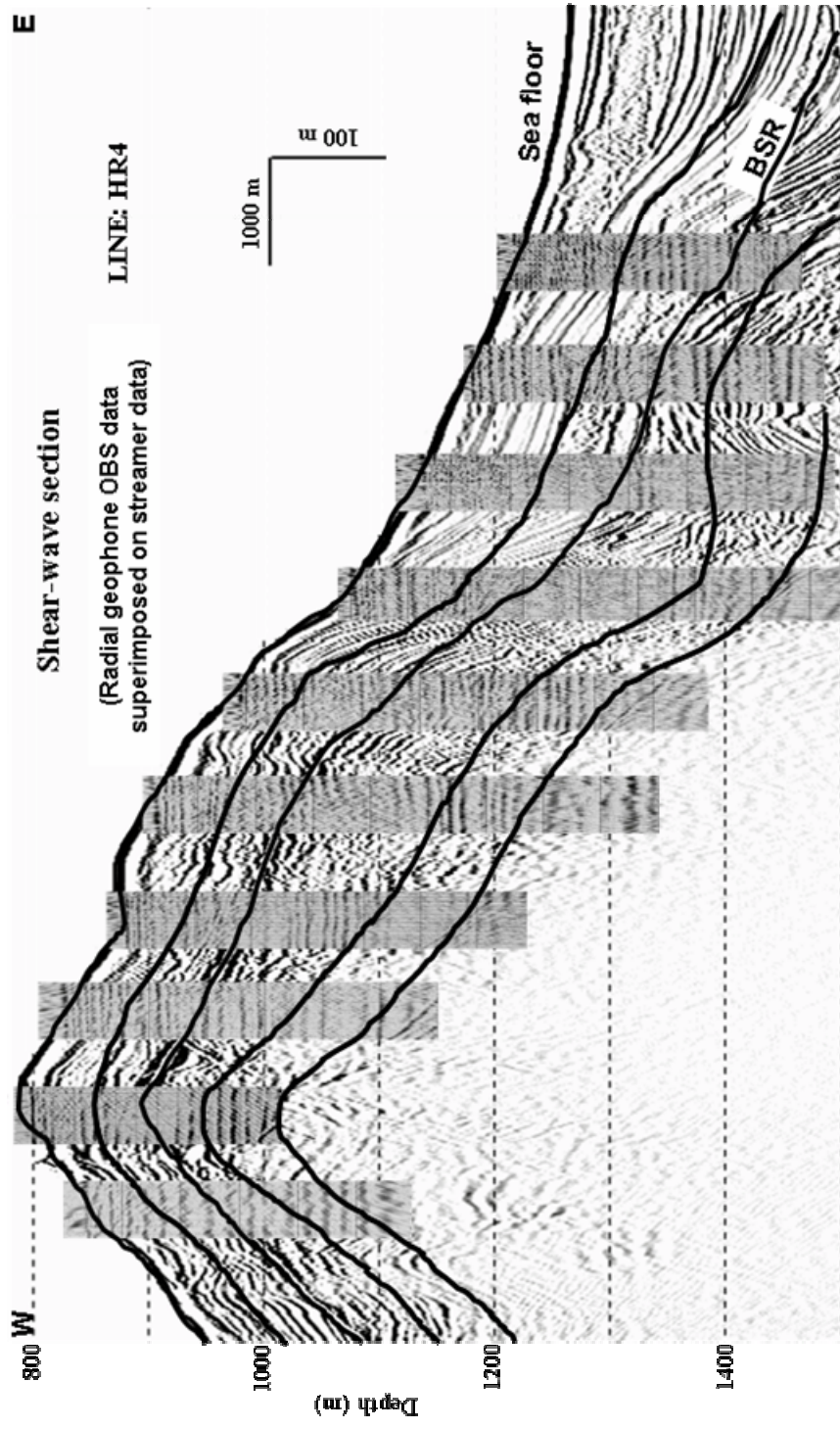
Figure 5.16. A W-E shear-wave section. Radial component geophone data (in the τ-p domain with p ranging from 0 to 0.5 s/km) from all the OBS stations (corresponding to shear reflection panels in the figure) are NMO corrected and converted to depth, and they are superimposed on the depth converted streamer data at their respective locations.

135
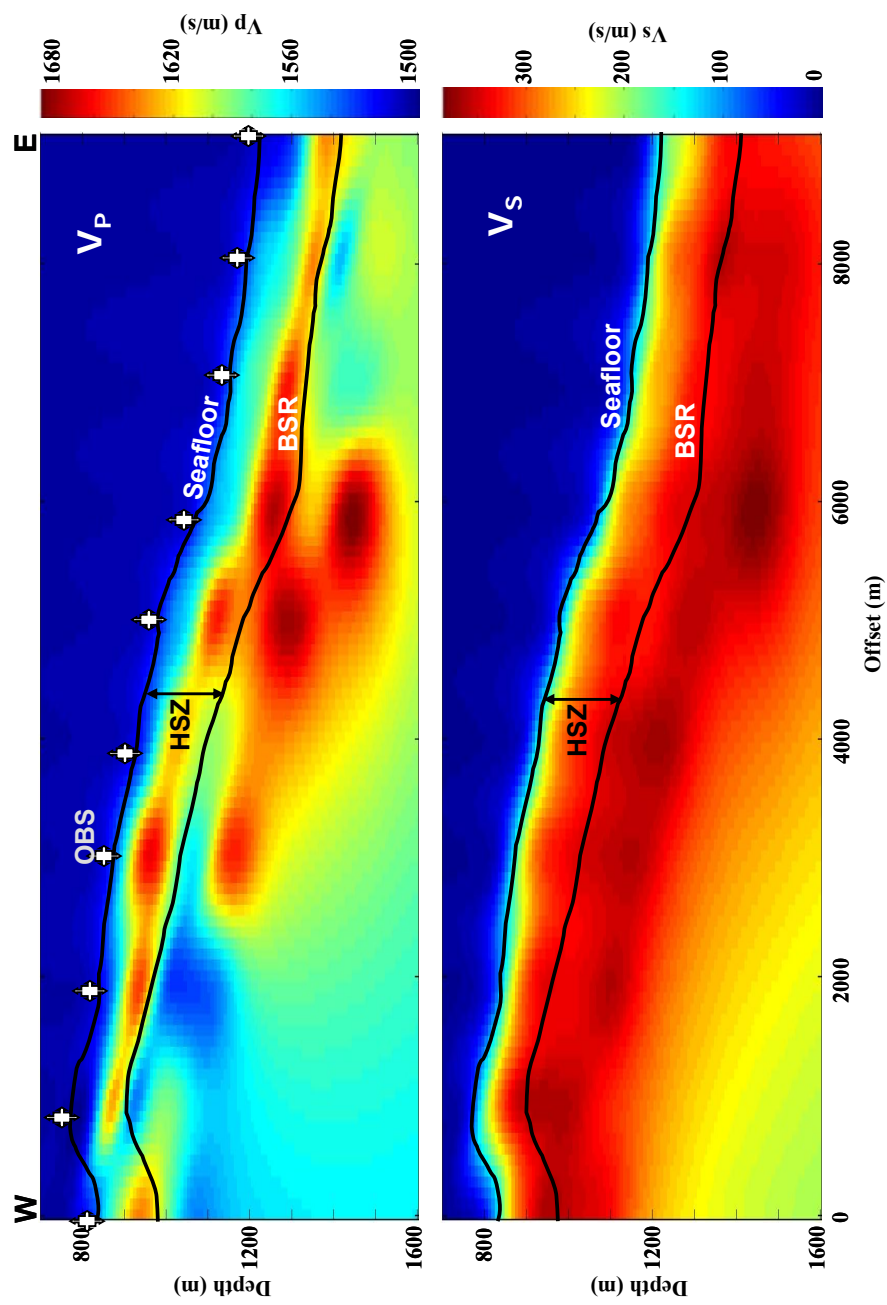
Figure 5.17. The W-E profiles of P- and S-wave interval velocities estimated from multicomponent data analysis. 1D velocity profiles are interpolated to derive a smooth 2D profile.

5.5 GAS HYDRATE SATURATION ESTIMATION

Seismic wave velocities are greatly influenced by the presence of gas hydrate and free gas in the sediments (e.g., Yuan, et al., 1996). In the presence of gas hydrate, P- and S-wave velocities increase; while in the presence of free gas, P-wave velocity decreases significantly but the S-wave velocity remains almost unchanged (Domenico, 1976). Also the velocity increases if the hydrate saturation in the pore space increases (Hyndman and Spence, 1992). It means that the P- and S-wave velocity information (anomalous with respect to a background medium velocity) can be used to estimate the gas hydrate and free gas distribution and saturation. This requires a relationship between the hydrate (and/or free gas) fraction in the sediments and the elastic properties (Vp and Vs). In this example, I use water-saturated unconsolidated sediments as the background medium.

Several authors have presented relationships between seismic velocities and gas hydrate saturation, which can be broadly classified into two categories: 1) Wyllie's (1958) time average or Wood's (1941) relation (e.g., Lee et al., 1996), and 2) rock physics based effective medium modeling (e.g., Helgerud et al., 1999). The first relation is empirical and simple, and the second method is more physical but difficult to implement. Rock physics based methods require information on the type of hydrate model (cement, part of matrix frame, or floating in the pore spaces), critical porosity of the matrix, effective pressure, and coordination number (of hydrate crystal); which are again not trivial. In this chapter, I present a simple and meaningful formulation for estimation of gas hydrate saturation specially suited to Hydrate Ridge.

137

The Wood equation is a better representation of P-wave velocity if the hydrates are suspended in pore spaces (all physical identities are independent), and the time average equation is applicable if the hydrate selectively cements grain contacts (Lee et al., 1996). At Hydrate Ridge, the sediments are unconsolidated with a high porosity ($\approx 60\%$) (Trehu et al., 2003). S-wave velocity is very low (250-350 m/s), suggesting very low rigidity, and does not increase much with the presence of hydrates (Figure 5.17), suggesting that hydrates do not bind sediment grains enough to increase the shear properties (rigidity). Therefore, the Wyllie time average equation is not appropriate for the HR region. Also at the HR, the hydrates are found in sediments (massive hydrates) and not just in pore space (see reports from drilling program in Trehu et al., 2003). These hydrates can be modeled with a rock physics effective medium model for the gas hydrates (Helgerud et al., 1999) which states that hydrate formation reduces the porosity and becomes a part of the solid matrix. For these reasons, I modify the Wood equation with a rock physics model for calculation of P-wave velocity in hydrate-bearing sediments on the HR, and I call it a "Modified Wood equation" (appendix E). This method uses volumetric averaging of compliances. An empirical relation is given for S-wave velocity (appendix E).

Table 5.1 lists all the parameters and its values used in the seismic velocity estimation. Clay (80%) and Quartz (20%) constitute the mineral grains, and their elastic moduli are much higher than that of gas hydrate. Therefore, when hydrate becomes part of the solid matrix (according to this rock physics model) the effective modulus of the solid matrix (given by equation E.6) will decrease

138

(Figure 5.18a). Figures 5.18b and 5.18c show plots of P- and S-wave velocities (using equations E.3 and E.8) with respect to the gas saturation for two different saturations of hydrate and with respect to the hydrate saturation (volume fraction of rock) for four different saturations (up to 5%) of free gas (volume fraction of fluid), respectively. Low free gas saturation has been considered in the analysis (e.g., Figure 5.18c) because very low saturation of free gas (up to 2%) is present on the HR. It is evident from the plot of velocities and saturations of free gas and gas hydrate (Figure 5.18) that the P-wave velocity variations are more prominent compared to the S-wave velocity variations, which is also observed in the velocities estimated from multicomponent data (Figure 5.17). This means that the new formulation for velocity calculation is appropriate for this geologic setting; the P-wave velocity will dominate over the S-wave velocity in the estimation of hydrate saturation at the HR.

For the estimation of gas hydrates and free gas saturation in a layer, I match theoretical and observed velocities. For example, Figure 5.19a shows the rms (root mean squares) error contours calculated by matching theoretical and observed (P- and S-wave) velocities for different saturation of hydrates and free gas. The minimum error will correspond to the correct value of saturations, which are about 11% (of rock) and 0.4% (of fluid saturation) for hydrate and free gas, respectively (Figure 5.19a). Figure 5.19b shows a comparison of gas hydrate saturation, where the P-wave velocity is computed by two different methods, the Wood equation (equation E.1) and the Modified Wood equation (equation E.3). Note that the Wood equation overestimates (compare to value estimated from the

Modified Wood equation) the hydrate saturation for a given velocity (when compared with the hydrate saturation estimated from the drilling data, Figures 5.19b). Note that hydrate saturation values are presented as volumetric fraction of the total rock; to convert this value as volumetric fraction of the solid phase and as volumetric fraction of the pore space, divide the given hydrate saturation by the solid fraction of rock (after addition of hydrate) and porosity (before addition of hydrates), respectively (equation E.9, appendix E).

Once correlation of seismic velocities and gas hydrate saturations are established (Figures 5.18 and 5.19), I calculated gas hydrate saturation using this new formulation across south summit (Figure 5.20) where interval P- and S-wave velocities are known (Figure 5.17). I interpolated and smoothed the 1D saturation values at OBS sites to produce a 2D profile of hydrate saturation, where maximum hydrate saturation is about 7% of the rocks (which is 12% of the pore space and 15% of solid phase). This hydrate saturation estimation agrees with the saturation derived from cores and log data (Trehu et al., 2004). Figure 5.21 compares hydrate saturation derived from the chloride anomaly and from the seismic data (my estimation) at the south summit (site 1250). My saturation estimation deviates from the saturation derived from core and log data at the south summit in the first 10m below seafloor (Trehu et al., 2004), as my estimation is comparatively lower. This discrepancy is possibly due to the presence of free gas at that position (10m below seafloor) which affects the P-wave velocity significantly (e.g., Figure 5.18b) and therefore reduces hydrate saturation estimation; also from velocity analysis such a fine resolution is not available.

Constituents	Volume (%)	K (GPa)	G (GPa)	ρ (g/cm^3)
Clay	80	20.9	6.85	2.58
Quartz	20	36.6	45.0	2.65
Gas hydrate	S_h	7.9	3.3	0.90
Water[*]	S_w	2.25	0	1.0
Methane gas	S_g	0.11	0	0.23

Table 5.1. Parameters used in the estimation of gas hydrate and free gas saturation: S_h is the volumetric fraction of hydrates in the rock, and water (S_w) and methane gas (S_g) making the fluid (i.e., $S_w + S_g = 1$). Data are from Helgerud et al. (1999) and Lee et al. (1996) (*).
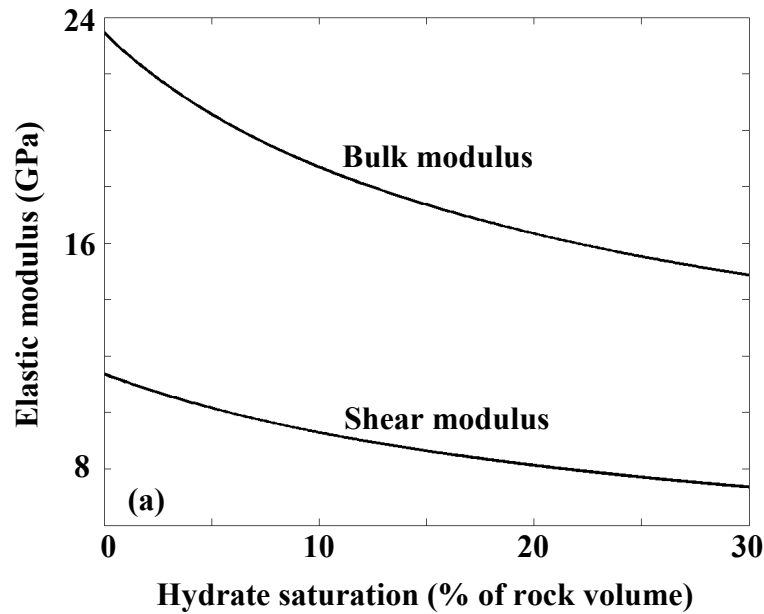
Figure 5.18a. Elastic modulus of the solid matrix in the presence of gas hydrates. Since modulus of gas hydrates is lower than that of quartz and clay, effective modulus of the solid matrix decreases with hydrate saturation. However, modulus (or velocity) of the total rock volume increases with hydrate saturation (see Figure 5.18c)

141
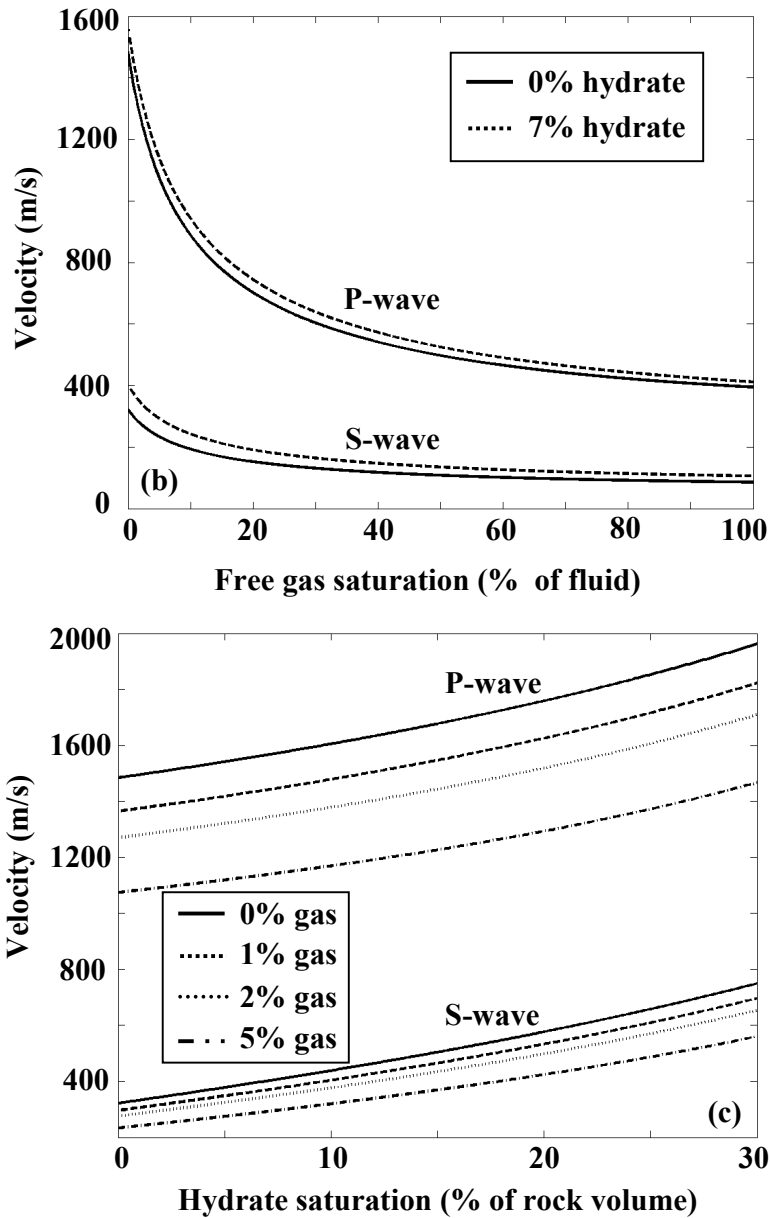
Figure 5.18 b&c. Variation of P- and S-wave velocities with respect to free gas saturation as fraction of fluid (b) and hydrate saturation as fraction of total rock volume (c). P-wave velocity decreases exponentially for first 10% addition of free gas (a). Both P- and S-wave velocities increase with hydrate saturation and decrease with gas saturation, however effect is more pronounced for the P-wave.

142
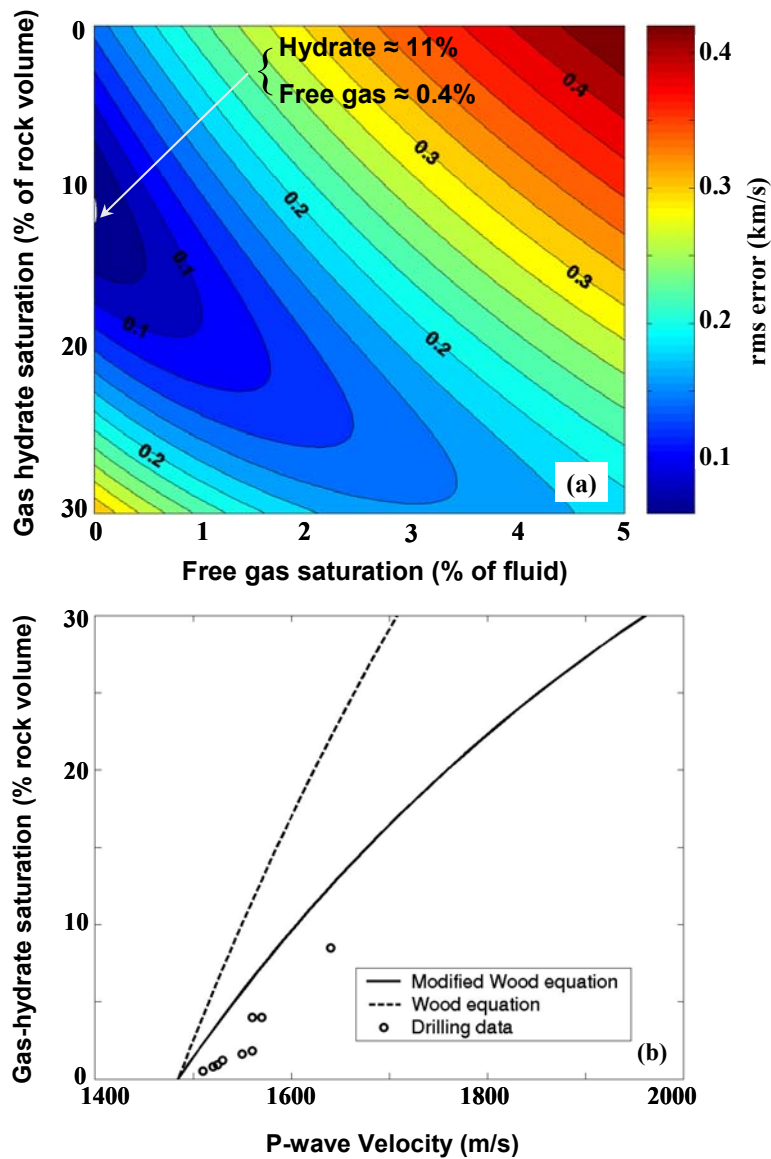
Figure 5.19. Gas hydrate saturation (as volumetric fraction of total rock) and free gas saturation (as fraction of fluid) estimation by matching a theoretical and an observed P- and S-wave velocities. The matching is shown as an error value contours (a), and (b) shows the difference in hydrate saturation estimated using P-wave velocity calculated with two methods. Note that the hydrate saturation estimated with the Modified Wood equation follows the drilling data (Trehu et al., 2003) better than that estimated with the Wood equation.

143
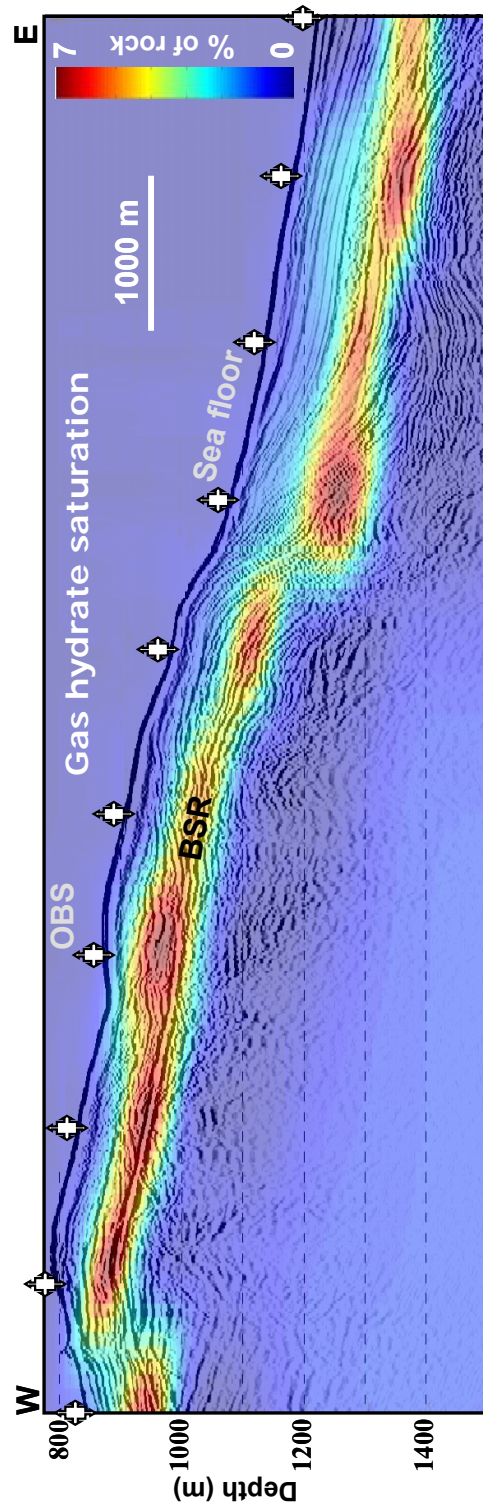
Figure 5.20. Gas hydrate saturation (volumetric fraction of total rock) across the south summit (W-E) on the Hydrate Ridge. Saturation estimation is performed by matching the observed velocities with the calculated velocities using a "Modified Wood equation" (equations E.3 and E.8 for P- and S-wave velocities, respectively).

144
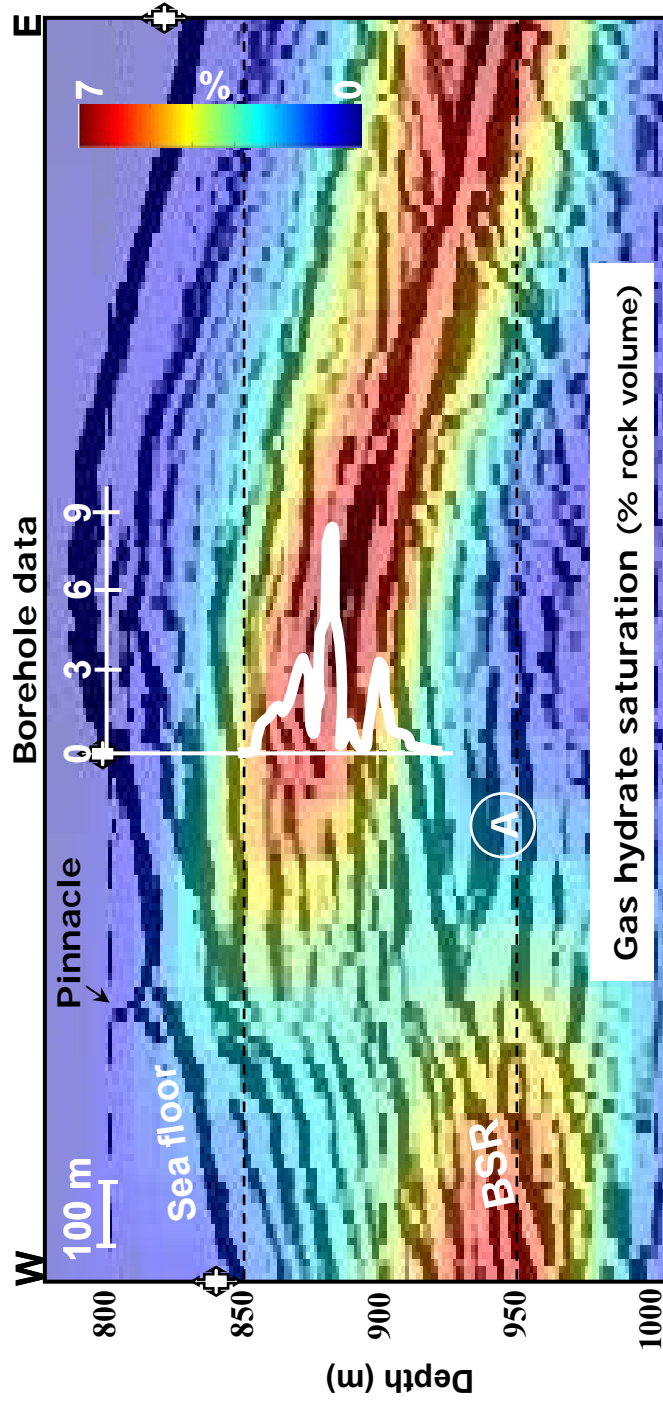
Figure 5.21. Gas hydrate saturation (volumetric fraction of total rock) estimated from borehole data (white curve) (estimated from the Chloride data, see Trehu et al., 2003, Figure 17B) and seismic data (in color plot, same as the Figure 5.20) at the south summit (covering leftmost three OBSs in the Figure 5.20) on the Hydrate Ridge. Both dataset agree well except that borehole data give better resolution than seismic data. Note a strong reflection "A" which is a path along which methane-rich fluids and free-gas migrate to the summit and a Pinnacle (a carbonate mound) which forms on the seafloor as methane reacts with Sulphate forming carbonate (see also Figure 4.3).

5.6 INTERPRETATION OF THE RESULTS

Analysis of converted S-waves on multicomponent seismic data is not a trivial task; it depends on the quality of the data, accuracy of the P-wave velocity and correlation of P- to S-wave reflection events. These require knowledge of geological settings of area and constraints from other independent sources. The S-wave velocity is estimated for a reflection event for which the P-wave reflection event is known. Since P- and S-wave reflectivity for a layer-interface are not the same, for some reflectors, correlation of events on P- and S-wave data are not trivial. Synthetic seismograms and traveltime tables helped in event correlation. Finally I match the reflectors on P- and S-wave data in depth. Seismic velocities estimated after velocity analysis in this chapter matched well with the sonic logs available at the summit and the slope basin side. The S-wave velocity analysis at the south summit and the slope basin site are well constrained by the sonic logs and geological information. However, since S-waves propagate nearly vertically to the receivers, there is not much angle coverage by the reflected S-wave (incident wave is P-wave) and therefore the NMO application (curve fitting) is not very sensitive to velocity variations. Fortunately, sonic logs are available at two locations.

After analysis of all the OBS data I produce the S-wave section across the south summit (Figure 5.16) where I match the major reflectors with the streamer (P-wave) seismic data. The reflectors are matched corresponding to PP- and PS-wave events. The SS-wave event can also be identified on the radial component geophone (e.g., Figure 5.8) and analyzed for the S-wave analysis. Such arrivals

146

will have broader reflection angle coverage at the receiver than the PS-wave arrivals.

The S-wave velocity in the hydrate-bearing sediments (from the seafloor to the BSR) does not show anomalous increase like the P-wave velocity (Figure 5.17). I interpret that the hydrate does not cement sediment grains enough to affect shear properties significantly. It is more likely that hydrates form within the pore space as part of the sediments. This is also observed in the drilling data (Trehu et al., 2003). This interpretation reduces the effect of gas hydrate as a possible cause of slope stability and slope failure, since even if hydrate dissociates (resulting into free gas and water), the shear strength of accompanying sediments will not decrease significantly which will prevent the sediments flow.

The P- and S-wave velocities are effective in identification of hydrate-bearing zones and quantification of the hydrate saturation. The lower P-wave velocity and unchanged S-wave velocity below the BSR (and close to the seafloor at the south summit) (Figure 5.17) indicate the presence of free gas, which supports the fluid migration mechanism from below the BSR to the seafloor. Free gas present below the BSR can move up if they are oversaturated (to overcome the capillary forces) and/or in the presence of fluid path. On the Hydrate Ridge, my results indicate that P-wave velocities are more sensitive than the S-wave velocities on the variation of gas-hydrate and free-gas saturation, which are well modeled with a modified Wood equation. This new velocity calculation formulation is realistic and simple to implement, and can be used to remotely estimate hydrate saturation. However, in areas where both free-gas and gas-

hydrates are present (as in the case of about 10m below the seafloor at the south summit) this formulation is not accurate. Also for better resolution of hydrate saturation higher resolution seismic velocities are required, which is possible with multicomponent data recorded with closely spaced receivers (i.e., OBC data).

Hydrate saturation estimated at the Hydrate Ridge is up to 7% of the bulk rock volume (which is 12% of the pore space and 15% of the solid phase). This saturation of hydrates in the sediments are probably not sufficient to seal the free gas below BSR level, however it will restrict the fluid motion upward through hydrate-bearing sediments. Two other reasons for the presence of free gas below BSR are: 1) thermodynamic condition below the BSR (i.e., high temperature) is not favorable for the hydrates and they are in the free gas form, and 2) saturation of free gas below BSR is low (about 2-5%) (known from the drilling result) in that case the capillary forces will not allow the free gas to move (Clennell et al., 1999). From the estimated hydrate saturation and the free gas saturation known from the drilling, it is more likely that presence of hydrate is not the only reason to keep the free gas below BSR level, but it does prohibit the fluid flow through hydrate-bearing sediments.

5.7 SUMMARY

The S-wave velocity analysis requires accurate measurement of P-wave velocity and correlation of P- and S-wave reflection events. Event correlation between P- and S-wave data is performed with the help of model-based traveltime tables and synthetic seismograms. In many situations, the event correlation is not trivial and it requires constraints from other sources. I used sonic and dipole sonic logs available at the two locations to constrain the event correlation and S-wave velocity estimation. The P- and S-wave velocities together confirm the presence of free-gas below the BSR and in the shallow zones at the south summit. The derived S-wave velocity profiles are monotonically increasing functions of depth within the hydrate-bearing sediment, which suggests that hydrates are not cementing the matrix grains enough to increase the shear properties significantly. It is likely that the hydrates are within the pore space as part of the sediments. I developed a modified Wood equation, which includes rock physics based saturation effects of hydrates, for calculation of seismic velocities in gas-hydrate-bearing sediments, and is appropriate for the Hydrate Ridge area. The mapping of the derived seismic velocities to the gas hydrates saturation at the HR results in the maximum hydrate saturation of 7% of the bulk rock volume (12 % of pore space). Because the hydrate occupies just small portion of the pore space, it is not sufficient to seal the free gas below BSR, and free gas is present likely due to the thermodynamic condition and capillary forces. The estimation of hydrate saturation agrees with drilling data, except at the south summit (up to 10m down from the seafloor) where free gas migrates up into the hydrate stability zone.

Chapter 6: Summary and future work

6.1 SUMMARY

Multicomponent seismic data can be used to derive an image of the earth's subsurface in terms of elastic properties (P- and S-wave velocities), which can be used further to infer several reservoir properties such as lithology, porosity, saturation, and fluid migration. The S-waves in a marine setting are converted waves and are recorded on the horizontal receivers with OBS or VSP survey. A seismic experiment was performed during the summer of 2002 at the Hydrate Ridge (HR) of the Cascadia convergent margin to map the gas hydrate and free gas and understand the mechanism of fluid migration. Special emphasis was given to the analysis of the S-wave velocity variations in the gas-hydrate-bearing sediments. This dissertation is focused on the development of new algorithms for multicomponent data analysis and applying them to the data acquired at the HR.

In this dissertation, I discussed the algorithms developed for seismic data analysis, which include: 1) a ray-Born based algorithm for calculating synthetic seismogram in heterogeneous and anisotropic media (chapter 2), and 2) a new traveltime calculation method in a transversely isotropic medium with a tilted axis of symmetry (TTI), where the elastic parameters and the tilt of TTI medium can vary in space (chapter 3). The ray-Born method models the subsurface as a background medium and a perturbation (heterogeneity), which is applicable in a weakly heterogeneous medium. The new traveltime method is a brute force approach based on the Fermat's principle. This algorithm was tested for prestack

depth migration with a physical model dataset. It can be used in traveltime computation in isotropic and anisotropic media.

Chapters 4 and 5 are focused on P- and S-waves analysis, respectively, using multicomponent seismic data recorded at the HR. My data analysis is centered at regions where the multicomponent OBS and VSP data are available, i.e., from the south summit to the slope basin side covering about 9km. Using the VSP data, I found convincing evidence of seismic anisotropy on the south summit site but at the slope basin side is isotropic. The anisotropy at the south summit is possibly caused by the vertical hydrate veins, which form as free-gas migrates in the hydrate stability zone (HSZ) along fractures. This anisotropy is a transverse isotropy with a horizontal axis of symmetry (HTI) where the vertical P-wave velocity is found to be higher than the horizontal velocity. Traveltime-error-contour analysis with VSP data is performed for the estimation of homogeneous anisotropic parameters. The resultant model is used to build an initial model for traveltime inversion to estimate heterogeneous and anisotropic model using VSP and OBS data. Traveltime computation method discussed in chapter 3 was used as a forward modeling method to generate synthetic traveltime data and very fast simulated annealing (VSFA) algorithm was used as an inversion scheme. Seismic anisotropic parameter (P-wave anisotropic parameter, ε) has been correlated to the fracture density in qualitative sense. However quantitative estimation of fracture parameters is not possible with this dataset.

The P- and S-waves interval velocity analysis is performed in the τ-p (intercept time − ray parameters) domain following three main steps: 1) P-wave

151

velocity analysis, 2) P- to S-wave reflection event correlation, and 3) S-wave velocity analysis. Initial calibration is done by tying the synthetics for a well log with a seismic gather from the same location. The P-wave interval velocity analysis with hydrophone OBS data results into the 1D P-wave velocities as a function of depth. The S-wave velocity analysis requires P- to S-wave reflection event correlation, for which I used synthetic seismograms and traveltime tables. A traveltime table gives the expected arrival time for various wavetypes in seismograms and synthetic seismogram is used to identify and match the moveout and correlate with real data. This is a very interpretive step. The S-wave analysis is performed similar to P-wave for the identified S-wave reflection events on the radial component geophone data. The 1D P- and S-wave velocities estimated at OBS stations are interpolated between OBS locations (1km spacing) to produce the smooth velocity models.

I developed a "Modified Wood equation" and an empirical equation (appendix E) to calculate P- and S-wave velocities. The modified Wood equation is a modification of original Wood equation with a rock physics model which is suited for the hydrate-bearing sediments at HR. I match the theoretical velocities to the observed velocities to estimate hydrate saturation. The P-wave velocity is found to be more sensitive to the saturation of gas hydrates (maximum of 7% of rock volume) and free gas than the S-wave velocity. The S-wave velocity is not abnormally high in the hydrate-saturated sediments, which indicate that hydrate may not be cementing the sediments matrix enough to increase the shear strength of the sediments. The hydrate may be in pore space as a part of the sediments.

152

6.2 FUTURE WORK

Multicomponent data analysis algorithms for converted S-waves are not fully developed. The P- to S-wave reflection event correlation is an iterative and interpretive process which requires more work to make it fast and reliable. The converted S-waves from shallow sedimentary layers arrive at the receivers at near vertical angles even at large offsets; thus in an OBS setting there is not much angle coverage for the S-waves propagation (one-way propagation is P-wave), which means that the estimated S-wave velocity by fitting the moveout may not be very accurate. The SS-wave arrivals at the receiver can be used in S-wave velocity estimation but generally such arrivals are too weak to be analyzed. Estimation of gas hydrate saturation makes use of anomalous values of seismic velocities compared to the background velocity. This creates two issues: 1) how accurate is the background velocity, and 2) what else is contributing to the velocity anomaly apart from the hydrates. Various contributions should be considered in saturation estimation. Gas hydrate exploration is an ongoing research. I used the multicomponent data recorded with shot traverses over OBS and VSP instruments; however there are more offline traverse data which can be used to constrain the 3D distribution of hydrate and free-gas. There are opportunities for fracture (anisotropy) characterization using amplitude variation with offsets and azimuths (AVOA) and shear-wave splitting analysis. More detailed information on fracture pattern will improve the fluid migration interpretation on the south summit and fracture density can be correlated to hydrate saturation in the hydrate stability zone.

153

Appendices

A. ALGORITHM FOR SLOWNESS IN ANISOTROPIC MEDIA

For a source free region, plane wave representation of the elastodynamic wave equation in general anisotropic media in the frequency-wavenumber domain is known as the Christoffel equation (e.g., p.165, Auld, 1990),

$$k^2 \Gamma_{ij} u_j = \rho \omega^2 u_i \tag{A.1}$$

where k is a wavenumber, $\mathbf{\Gamma}$ is a Christoffel matrix, $\mathbf{u}$ is a displacement vector, and ρ is density. The Christoffel equation is an eigen value equation, and its eigen values are the squares of slowness values (inverse of phase velocity) for the corresponding wave-types ($i = 1, 2, 3$). There are three solutions of the above equation representing three wave-types (one P-wave and two S-waves). The Christoffel matrix can be solved either by singular value decomposition (SVD) or analytically (Abramowitz and Stegun, 1965) since it is simply a cubic equation.

Algorithm for the estimation of phase slowness:

- Loop over propagation directions

    calculate $\mathbf{\Gamma}$ (e.g., p.211, Auld, 1990)

    solve equation (A.1) to get 3 values of k^2/ω^2

    square roots of above are the slowness values

- End loop

154

B. ALGORITHM FOR GROUP VELOCITY IN ANISOTROPIC MEDIA

Ray tracing systems in anisotropic media (equation 15, Červený, 1972) are,

$$\frac{dx_i}{dT} = a_{ijkl} p_l \frac{D_{jk}}{D}$$

(B.1)

and,

$$\frac{dp_i}{dT} = -\frac{1}{2} \frac{\partial a_{ljks}}{\partial x_i} p_l p_s \frac{D_{jk}}{D}$$

(B.2)

where a_{ijkl} are the density normalized elastic moduli, $\mathbf{x}$ is displacement vector, T is time, $\mathbf{p}$ is slowness vector, and D and D_{ij} are calculated with Červený formulation (equation 14b, Červený, 1972). Equation (B.1) is the component of group velocity vectors ($i = 1, 2, 3$). This ray tracing system fails in the degenerate case of Eigen values (i.e., if eigen values are equal).

Algorithm for the estimation of group velocity:

- Loop over propagation directions

    slowness (p's) are known for each wavetypes (Appendix A)

    calculate Christoffel matrix, $\Gamma = a_{ijkl} p_i p_k$

    calculate D_{jk} (Cerveny, 1972)

    find group velocity for each wavetypes (equation B.1)

- End loop

C. RAY-BORN SCATTERED WAVEFIELD REPRESENTATION

The scattered wavefield can be estimated using a ray-Born approximation (e.g., Beyklin, and Burridge, 1990; Eaton and Stewart, 1994). The elastodynamic equation (2.1) can be written in terms of the Green's function ($G_{mk}(\mathbf{s}, \mathbf{x}, \omega)$) as (e.g., Ben-Menahem et al., 1991; Vavryčuk, 1997; p.27, Aki and Richards, 2002),

$$\left(c_{ijkl} G_{mk,l}\right)_{,j} + \rho \omega^2 G_{mi} = -\delta_{mi} \delta(\mathbf{x} - \mathbf{s}),$$ (C.1)

where $\mathbf{c}$ is elastic coefficient matrix, $\delta(\mathbf{x})$ is the Dirac delta function, δ_{jk} is Kronecker's symbol, ρ is density, $\mathbf{x}$ is receiver location, $\mathbf{s}$ is source location, and Einstein's summation convention for repeated indices is assumes and commas imply spatial differentiation. In the above equation, G_{mi} is the i th component of displacement due to the unit impulse in the m -direction. Green's function $G_{mk}(\mathbf{s}, \mathbf{x}, \omega)$ (see section 2.3.3) is the solution of the wave equation (C.1). The solution of equation (C.1) can be linearized about a reference medium for which a solution is determined using ray methods. In a Born representation, we consider the model as a reference medium plus a perturbation (e.g., Jin et al., 1992; p. 93, Červený, 2001)

$$c_{ijkl} = c_{ijkl}^0 + \Delta c_{ijkl},$$

$$\rho = \rho^0 + \Delta \rho,$$ (C.2)

and

$$G_{mk} = G_{mk}^0 + U_{mk}$$

where c_{ijkl}^0, ρ^0, and G_{mk}^0 are the reference parameters (smooth and differentiable), and Δc_{ijkl}, $\Delta\rho$, and U_{mk} are the perturbation parameters. U_{mk} is a scattered wavefield response due to an impulsive source. The reference parameters will also satisfy the above equation of motion (C.1), i.e.,

$$\left(c_{ijkl}^0 G_{mk,l}^0\right)_{,j} + \rho^0 \omega^2 G_{mi}^0 = -\delta_{mi}\delta(\mathbf{x}-\mathbf{s}). \tag{C.3}$$

Put equation (C.2) in equation (C.1) we get

$$\left\{\left(c_{ijkl}^0 + \Delta c_{ijkl}\right)\left(G_{mk,l}^0 + U_{mk,l}\right)\right\}_{,j} + \omega^2\left(\rho^0 + \Delta\rho\right)\left(G_{mi}^0 + U_{mi}\right) = -\delta_{mi}\delta(\mathbf{x}-\mathbf{s}). \tag{C.4}$$

Using equation (C.3) and expression for G_{mk} from equation (C.2), C.4 reduces to

$$\left(c_{ijkl}^0 U_{mk,l} + \Delta c_{ijkl} G_{mk,l}\right)_{,j} + \omega^2\left(\rho^0 U_{mi} + \Delta\rho G_{mi}\right) = 0. \tag{C.5}$$

Consider an incident wave (marked with tilde '~'), and apply the first-order Born approximation ($G_{mk} = \widetilde{G}_{mk}^0 = G_{mk}^0$) to equation (C.5), we get

$$\left(c_{ijkl}^0 U_{mk,l}\right)_{,j} + \rho^0\omega^2 U_{mi} = -\left(\Delta c_{ijkl}\widetilde{G}_{mk,l}^0 + \omega^2\Delta\rho\widetilde{G}_{mi}^0\right), \tag{C.6}$$

where $U_{mi}(\mathbf{s},\mathbf{x},\omega)$ is the scattered wavefield, and the right hand side of equation (C.6) represents a source term within the single scattering approximation.

The elastodynamic equation (C.5) can be also written in terms of the Green's function at the receiver location ($\hat{G}_{ni}(\mathbf{s},\mathbf{r},\omega)$). By comparing this with the equation (C.6) and applying the boundary condition ($\Delta c_{ijkl} = 0$ at the boundary of the region of interest, D), the scattering response becomes,

157

$$U_{mn}(\mathbf{s},\mathbf{r},\omega) \approx \int_D \left[\omega^2 \Delta\rho \widetilde{G}^0_{mi}(\mathbf{s},\mathbf{x},\omega) \hat{G}^0_{ni}(\mathbf{s},\mathbf{r},\omega) + \Delta c_{ijkl} \widetilde{G}^0_{mk,l}(\mathbf{s},\mathbf{x},\omega) \hat{G}^0_{ni,j}(\mathbf{s},\mathbf{r},\omega) \right] d\mathbf{x},$$

where U_{mn} represents the superposition of all single-scattered arrivals, variables with a tilde (~) are related to the incident wavefield and those with a caret (∧) are related to the reflected wavefield. This approximation is valid for weak perturbations, i.e., $\left| \dfrac{\Delta c_{ijkl}}{c_{ijkl}} \right| << 1$ and $\left| \dfrac{\Delta\rho}{\rho} \right| << 1$. To evaluate U_{mn}, the Green's functions are required, which are known exactly for very few simple media. Further, Green's function can be approximated with the zeroth-order asymptotic ray theory (e.g., Ben-Menahem et al., 1991)

$$G_{mk}(\mathbf{s},\mathbf{x},\omega) \approx A g_m(\mathbf{s}) g_k(\mathbf{x}) e^{i\omega t}, \tag{C.7}$$

and then the scattering response reduces to (Eaton and Stewart, 1994)

$$U_{mn}(\mathbf{s},\mathbf{r},\omega) \approx \omega^2 \sum_\Omega \widetilde{g}_m(\mathbf{s}) \hat{g}_n(\mathbf{r}) \int_D d\mathbf{x} \left[\Delta\rho \delta_{ik} + \Delta c_{ijkl} \widetilde{p}_l \hat{p}_j \right] A \widetilde{g}_k \hat{g}_i e^{i\omega t} \tag{C.8}$$

where Ω represents the summation over different wavetypes (qP- and qS-waves) response, A is the amplitude coefficient, t is the traveltime (satisfies Eikonal equation), and g_i and p_i are the polarization and the slowness components, respectively, in the ith direction.

D. TRAVELTIME CALCULATION WITH DIRECT METHOD

From Figure 3.1a, the traveltimes at points (x_a, z_1) and (x_a, z_2) are given by (Schneider, Jr. et al, 1992; Faria and Stoffa, 1994)

$$t_1 = s_a (x_a^2 + z_1^2)^{1/2} \qquad (D.1)$$

and, $\qquad t_2 = s_a (x_a^2 + z_2^2)^{1/2} \qquad (D.2)$

where s_a corresponds to the average slowness from the source to point (x_a, z_1) and point (x_a, z_2). From above two equations s_a can be written as

$$s_a^2 = \frac{t_2^2 - t_1^2}{z_2^2 - z_1^2} = w \qquad (D.3)$$

where w corresponds to the average squared vertical slowness. The traveltime t_0 to point (x_a, z_0) can be written as

$$t_0^2 = t_1^2 + w(z_0^2 - z_1^2) \qquad (D.4)$$

or, in terms of angle Ψ and lateral grid spacing Δx as

$$t_0^2 = t_1^2 + w((z_2 \pm \Delta x \cot \Psi)^2 - z_1^2) \qquad (D.5)$$

Use sign (-) when $z_2 \rangle z_1$ and sign (+) when $z_2 \langle z_1$. The total traveltime, then, from the source to point (x, z_2) in Figure 3.1a, is given by

$$t = t_0 + s(\phi) \Delta x \operatorname{cosec}(\Psi) \qquad (D.6)$$

where Δx is the horizontal grid spacing, and $s(\phi)$ is the group slowness. The traveltime at grid point (x, z_2) is calculated by minimizing equation (D.6) with respect to angle Ψ

$$\frac{dt}{d\Psi} = 0 . \tag{D.7}$$

Also, $\quad \dfrac{dt}{d\Psi} = D_1 + D_2 , \tag{D.8}$

where

$$D_1 = \frac{\mp w \Delta x \operatorname{cosec}^2 \Psi (z_2 \pm \Delta x \cot \Psi)}{\{w[(z_2 \pm \Delta x \cot \Psi)^2 - z_1^2] + t_1^2\}^{1/2}} . \tag{D.9}$$

Using the group velocity approximation equation (3.2), D_2 can be written as

$$D_2 = \Delta x \operatorname{cosec} \Psi \{ \frac{2a_3 \sin \phi \cos^3 \phi - a_2 \sin \phi \cos \phi}{s(\phi)} - s(\phi) \cot \Psi \} . \tag{D.10}$$

Using equation (D.8) $\dfrac{dt}{d\Psi}$ can be calculated, but it is difficult to find the roots of equation (D.7). For simplicity, I assume that this derivative function is a smooth continuous function even for complex geology. By calculating an arbitrary number of values of $\dfrac{dt}{d\Psi}$, e.g., at $\Psi = 45^0$, 67.5^0, and 90^0, the root between 0^0 and 90^0 degree can be approximated using Lagrange interpolation.

For the traveltime computation in TTI media, I use the same formulation as discussed above, except that I use equation (3.4) instead of equation (3.2) to calculate $v_g(\phi)$ $(= 1/s(\phi))$, which is used in equation (D.6).

E. Modified Wood Equation

Four-phase (water, gas, hydrate, and matrix) Wood equation for hydrated sediments can be expressed as (Lee et al., 1996),

$$\frac{1}{\rho V_P^2} = \frac{\phi S_w}{\rho_w V_w^2} + \frac{\phi S_g}{\rho_g V_g^2} + \frac{\phi S_h}{\rho_h V_h^2} + \frac{1-\phi}{\rho_m V_m^2} \qquad \text{(E.1)}$$

where V_P, V_w, V_g, V_h, and V_m are the P-wave velocity in the hydrated sediments, water, free-gas, pure hydrate (3730 m/s), and matrix, respectively, ϕ is porosity (as a fraction), S_w, S_g, and S_h are the saturations of water, gas, and hydrate in the pore space, respectively ($S_w + S_g + S_h = 1$), and ρ_w, ρ_g, ρ_h, ρ_m, and ρ are density of water, free gas (methane), hydrate, matrix, and bulk sediment, respectively. This relation is valid for suspension model (all identities are independent).

From the rock physics model (Helgerud et al., 1999), hydrate formation does two things; it 1) reduces the porosity, and 2) changes the seismic velocities in the matrix. The new system of equations are expressed as

$$\phi = \phi_{orig} - S_h, \qquad \text{(E.2)}$$

and

$$\frac{1}{\rho V_P^2} = \frac{\phi S_w}{\rho_w V_w^2} + \frac{\phi S_g}{\rho_g V_g^2} + \frac{1-\phi}{\rho_m V_m^2}, \qquad \text{(E.3)}$$

where S_h is volumetric saturation of hydrates in the rock which is now part of solid matrix (different from the Wood equation; compare equations E.1 and E.3),

161

gas and water constitute the fluid part ($S_w + S_g = 1$), ϕ_{orig} and ϕ are the porosity before and after inclusion of hydrates. Equation (E.3) is a "Modified Wood equation". On the right side of this equation (E.3), the first two terms correspond to the fluid and the third term corresponds to the solid (includes the hydrates). In the Hydrate Ridge experiment, the matrix without hydrate is a mixture of clay ($\approx$ 80%) and quartz ($\approx$ 20%) (Trehu et al., 2003). The P-wave velocity in matrix (clay, quartz, and hydrate) after addition of hydrate is calculated with the rock physics model discussed below.

Consider, that the original volume percentage of clay and quartz are v_{clay}^0 and v_{quartz}^0, respectively. After addition of hydrate (S_h), matrix volume percentages of clay (v_{clay}), quartz (v_{quartz}) and hydrate (v_{hyd}) in the rock become (Helgerud et al., 1999)

$$v_{clay} = v_{clay}^0 \left(\frac{1 - \phi_{orig}}{1 - \phi} \right),$$

$$v_{quartz} = v_{quartz}^0 \left(\frac{1 - \phi_{orig}}{1 - \phi} \right), \qquad \text{(E.4)}$$

$$v_{hyd} = \left(\frac{S_h}{1 - \phi} \right),$$

respectively, where $v_{clay} + v_{quartz} + v_{hyd} = 1$. The P-wave velocity in the solid matrix is then given as

$$V_m = \sqrt{\frac{K_m + \frac{4}{3} G_m}{\rho_m}}, \qquad \text{(E.5)}$$

where K_m and G_m are the bulk modulus and the shear modulus of the matrix. The modulus of the solid phase are calculated from those of the individual mineral constituents using Hill's (1952) average formula given as

$$K_m = 0.5 \left[\sum_{i=1}^{3} v_i K_i + \left(\sum_{i=1}^{3} \frac{v_i}{K_i} \right)^{-1} \right],$$

and

$$G_m = 0.5 \left[\sum_{i=1}^{3} v_i G_i + \left(\sum_{i=1}^{3} \frac{v_i}{G_i} \right)^{-1} \right], \tag{E.6}$$

where v_i, K_i, and G_i are the solid volume percent, bulk modulus, and shear modulus of the individual element (clay, quartz, and hydrate) (Table 5.1). Figure 5.18a shows bulk modulus (K_m) and shear modulus (G_m) in the hydrate-bearing solid phase. Density can be found by the volume weighted average of the constituent components as,

$$\rho = \phi S_w \rho_w + \phi S_g \rho_g + (1 - \phi)\rho_m,$$

where

$$\rho_m = v_{clay}\rho_{clay} + v_{quartz}\rho_{quartz} + v_{hyd}\rho_h. \tag{E.7}$$

The S-wave velocity can be calculated similar to (Lee et al., 1996, equation 13) as

$$V_S = V_P (1 - \phi) \left(\frac{V_S}{V_P} \right)_m, \tag{E.8}$$

163

where $\left(\dfrac{V_S}{V_P}\right)_m$ is the ratio of S- to P-wave velocity in the matrix

$\left(= \sqrt{\dfrac{G_m}{K_m + \frac{4}{3}G_m}}\right).$

Above expressions for P- and S-wave velocity (equations E.3 and E.8) are used in this thesis to calculate the seismic velocities in hydrated sediments (Figure 5.18), which are matched with the observed velocities (Figure 5.17) to estimate the hydrate saturations as explained in the text (section 5.5). Hydrate saturation estimated from this formulation is volumetric saturation of hydrate in the rock (S_h) (see equation E.2), it can be converted to volumetric saturation of hydrate in the solid phase (S_h^{solid}) and in the pore space (S_h^{pore}) as

$$S_h^{solid} = \frac{S_h}{1-\phi}$$

and

$$S_h^{pore} = \frac{S_h}{\phi_{orig}} . \tag{E.9}$$

Similar to the above formulation to estimate seismic velocities in hydrated sediments (equations E.3 and E.8), Gassmann's equation can also be used (e.g., Helgerud et al., 1999) which will make use of equations E.6 and E.7 to calculate the matrix parameters (bulk modulus, shear modulus and density).

164

References

Abramowitz, M, and Stegun, I. A., 1965, Handbook of mathematical functions with formulas, graphs, and mathematical tables, Dover Pubns Publ.

Alkhalifah, T., 1995, Gaussian beam depth migration for anisotropic media: Geophysics, **60**, 1474-1484.

———— 1998, Acoustic approximations for processing in transversely isotropic media: Geophysics, **63**, 623-631.

———— 2002, Traveltime computation with the linearized Eikonal equation for anisotropic media: Geophys. Prosp., **50**, 373-382.

Alkhalifah, T., and Tsvankin, I., 1995, Velocity analysis for transversely isotropic media: Geophysics, **60**, 1550-1566.

Aki, K., and Richards, P., 2002, Quantitative Seismology: 2nd ed, University Science Books, California.

Auld, B. A., 1990, Acoustic fields and waves in solids, Vol. **1**, Krieger Publ. Co.

Backus, G. E., 1962, Long-wave elastic anisotropy produced by horizontal layering: J. Geophy. Res., **67**, 4427-4440.

Bagirov, E., and Lerche, I., 1997, Hydrates represent gas source, drilling hazard. Oil Gas J. **95**, 99-102.

Bangs, N. J. B., Sawyer, D. S., Golovchenko, X., 1993, Free gas st the base of the gas hydrate zone in the vicinity of the Chile triple junction: Geology, **21**, 905-908.

Banik, N. C., 1984, Velocity anisotropy of shales and depth estimation in the North Sea basin: Geophysics, **49**, 1411-1419.

———— 1987, An effective anisotropy parameter in transversely isotropic media: Geophysics, **52**, 1654-1664.

Barr, F. J., 1997, Dual-sensor OBC technology: The Leading Edge, **16**, 45-51.

Baysal, E., kosloff, D. D., and Sherwood, J. W.C., 1983, Reverse time migration: Geophysics, **48**, 1514-1524.

Behle, A., and Dohr, G., 1985, Converted waves in exploration seismics: in Seismic shear waves, Part B: Applications (ed Dohr, G. P.), Geophysical Press,London, **15B**, 178-223.

Ben-Menahem, A., Gibson Jr., R. L., and Sena, A G., 1991, Green's tensor and radiation patterns of point sources in general anisotropic inhomogeneous elastic media: Geophys. J. Int., **107**, 297-308.

Ben-Menahem, A., and Sena, A. G., 1990, Seismic source theory in stratified media: J. Geophys. Res., **95**, 15395-15427.

Berkhout, A. J., 1985, Seismic migration: Imaging of acoustic energy by wavefield exploration, A theoretical aspects: 3rd ed., Elsevier science Publ.

Berryman, J. G., 1979, Long-wave elastic anisotropy in transversely isotropic media: Geophysics, **44**, 896-917.

Bessonova, E. N., Fishman, V. M., Ryaboyi, V., Z., and Stinikova, G. A., 1974, The Tau method for inversion of travel times-I. Deep seismic sounding data: Geophys. J. R. astr. Soc., **36**, 377-398.

Beydoun, W. B., and Mendes, M., 1989, Elastic ray-Born l_2-migration/inversion: Geophys. J., **97**, 151-160.

Beylkin, G., and Burridge, R., 1990, Linearized inverse scattering problems in acoustic and elasticity: Wave Motion, **12**, 15-52.

Boetius, A. et al., 2000, A marine microbial consortium apparently mediating anaerobic oxidation of methane: Nature, **407**, 623-626.

Booth, D. C., and Crampin, S. C., 1983, The anisotropic reflectivity technique: theory: Geophys. J. R. astr. Soc., **72**, 755-766.

Brown, R. J., Stewart, R. R., and Lawton, D. C., 2002, A proposed polarity standard for multicomponent seismic data: Geophysics, **67**, 1028-1037.

Bulant, P., 1999, Two-point ray-tracing and controlled initial-value ray-tracing in 3-D heterogeneous block structures: J. Seis. Expl., **8**, 57-75.

Byun, B. S., Corrigan, D., and Gaiser, J., 1989, Anisotropic velocity analysis for lithology discrimination: Geophysics, **54**, 1564-1574.

Caldwell, J., 1999, Marine multicomponent seismology: The Leading Edge, **11**, 1274-1282.

Carcione, J. M., 2001, Wavefields in real media: wave propagation in anisotropic, anelastic and porous media: Handbook of Geophys. Explo., V. **31**.

Červený, V., 1972, Seismic rays and ray intensities in inhomogeneous anisotropic media: Geophys. J. R. astr. Soc., **29**, 1-13.

———— 2001, Seismic ray theory: 1st ed., Cambridge University Press.

Chapman, C. H., and shearer, P. M., 1989, Ray tracing in azimuthally anisotropic media-II. Quasi-shear wave coupling: Geophy. J., **96**, 65-83.

Claerbout, J. F., 1985, Imaging the Earth's Interior: Blackwell Science Publishers, Oxford, England.

Clennel, M. B., Hovland, M., Booth, J. S., Henry, P., and Winters, W. J., 1999, Formation of natural gas hydrates in marine sediments 1: Conceptual model of gas hydrate growth conditioned by host sediment properties: J Geophys. Res., **104**, 22985-23003.

Coates, R. T., and Chapman, C. H., 1990, Ray perturbation theory and the Born approximation: Geophys. J. Int., **100**, 379-392.

Connolly, P., 1999, Elastic impedance: The Leading Edge, **18**, 438-452.

Crampin, S., 1978, Seismic wave propagation through a cracked solid: Polarization as a possible dilatancy diagnostic: Geophys. J. R. astr. Soc., **53**, 467-496.

———— 1981, A review of wave motion in anisotropic and cracked elastic media: Wave Motion, **3**, 343-391.

———— 1985, Evidence of aligned cracks in the earth's crust: First Break, **3**, 12-15.

———— 1987, Geological and industrial implications of extensive-dilatancy anisotropy: Nature, **328**, 491-496.

Crampin, S., Chesnokov, E. M., and Hipkin, R. A., 1984, Seismic anisotropy-The state of the art: First Break, **20**, no. 3, 9-18.

Daley, P. F., and Hron, F., 1977, Reflection and transmission coefficients for transversely isotropic media: Bull. Seism. Soc. Am., **67**, 661-675.

Dellinger, J., Clarke, R., and Gutowski, P., 2001, Horizontal vector infidelity correction by general linear transform: SEG Expanded Abstracts, 865-868.

Dellinger, J., and Symes, W. W., 1997, Anisotropic finite-difference traveltimes using a Hamilton-Jacobi solver: SEG, Expanded Abstracts, 1786-1789.

Dewangan, P., and Grechka, V., 2003, Inversion of multicomponent, multiazimuth, walkaway VSP data for the stiffness tensor: Geophysics, **68**, 1022-1031.

Dickens, G. R., 1999, The blast in the past: Nature, **401**, 752-753.

Dickens, G. R., Paull, C. K., Wallace, P. & the ODP Leg 164 Scientific party, 1997, Direct measurement of in situ methane quantities in a large gas hydrate reservoir: Nature, **385**, 427-428.

DiSiena, J. P., Gaiser, J. E., and Corrigan, D., 1984, Horizontal components and shear wave analysis of three-component VSP data: in Vertical seismic profiling, Part **B**: Advanced concepts (ed Toksöz, M. N., and Stewart, R. R.), Geophysical Press, London, 177-188.

Dix, C. H., 1955, Seismic velocities from surface measurements: Geophysics, **20**, 68-86.

Domenico, S. N., 1976, Effects of brine-gas mixture on velocity in an unconsolidated sand reservoir: Geophysics, **41**, 882-894.

Duffaut, K., Alsos, T., Landrø, M., and Rognø, H., 2000, Shear-wave elastic impedance: The Leading Edge, **19**, 1222-1229.

Eaton, D. W. S., and Stewart, R. R., 1994, Migration/inversion for transversely isotropic elastic media: Geophys. J. Int., **119**, 667-683.

Ecker, C., Dvorkin, J., and Nur, A., 2000, Estimating the amount of gas hydrate and free gas from marine seismic data: Geophysics, **65**, 565-573.

Faria, E. L., and Stoffa, P. L., 1994, Traveltime computation in transversely isotropic media: Geophysics, **59**, 272-281.

Farra, V., and Madariaga, R., 1987, Seismic waveform modeling in heterogeneous media by ray perturbation theory: J. Geophys. Res., **92**, 2697-2712.

Ferguson, R. J., and Margrave, G. F., 2002, Depth imaging in anisotropic media by symmetric non-stationary phase shift, Geophys. Prosp., **50**, 281-288.

Fowler, P. J., 2003, Practical VTI approximations: a systematic anatomy: J App. Geophy., **54**, 347-367.

Fuchs, K., and Müller, 1971, Computation of synthetic seismograms with the reflectivity method and comparison with observation: Geophys. J. R. astro. Soc., **23**, 417-433.

Gaiser, J. E., 1990, Transversely isotropic phase velocity analysis from slowness estimates: J. Geophys. Res, **95**, 11241-11254.

———— 1999, Applications for vector coordinate systems of 3-D converted wave data: The Leading Edge, **18**, 1290-1300.

Gajewski, D., 1993, Radiation from point sources in general anisotropic media: Geophys. J. Int., **113**, 299-317.

Ganguly, N., Spence, G. D., Chapman, N. R., and Hyndman, R. D., 2000, Heat flow variations from bottom simulating reflectors on the Cascadia margin: Marine Geology, **164**, 53-68.

Garmany, J. D., 1984, the recovery of true particle motion from three component ocean bottom seismometer data: J. Geophys. Res., **89**, B11, 9245-9252.

———— 1989, A student's garden to anisotropy: Ann. Rev. Earth Planet. Sci., **17**, 285-308.

Garotta, R., 2000, Shear waves from acquisition to interpretation: SEG/EAGE Distinguished Instructor Series **3**, Soc. Expl. Geophys., Tulsa.

Gazdag, J., 1978, Wave-equation migration by phase shift method: Geophysics, **43**, 1342-1351.

Goodway, B., 2001, AVO and lame constants for rock parameterization and fluids detection: CSEG Recorder, **39**, 39-60.

Graebner, M., 1992, Plane-wave reflection and transmission coefficients for a transversely isotropic solid: Geophysics, **57**, 1512-1519.

Granli, J. R., Arntsen, B., Sollid, A., and Hilde, E., 1999, Imaging through gas-filed sediments using shear-wave data: Geophysics, **64**, 668-677.

Hardage, B. A., 2000, Vertical seismic profiling: principles: 3rd ed., Handbook of Exploration Geophysics, **14**, Elsevier Science Ltd. Publ.

Helbig, K., 1984a, Transverse isotropy in exploration seismics: Geophys. J. R. astro. Soc., **76**, 79-88.

——— 1984b, Anisotropy and dispersion in periodically layered media: Geophysics, **49**, 364-373.

——— 1994, Foundations of elastic anisotropy in exploration seismics: Handbook of Geophy. Expl., **22**, Elsevier Science Ltd, England.

Helgerud, M. B., Dvorkin, J., Sakai, A., and Collett, T., 1999, Elastic wave velocity in marine sediments with gas hydrates: effective medium modeling: Geophys. Res. Lett., **26**, 2021-2024.

Henriet, J. P., and Mienart, J. (eds), 1998, Gas Hydrate: Relevance to World Margin Stability and Climate Change: Spec. Publ. **137**, Geol. Soc, London

Hess, H. H., 1964, Seismic anisotropy of the uppermost mantle under oceans: Nature, **203**, 629-631.

Hill, R., 1952, The elastic behavior of crystalline aggregate: Proc. Phys. Soc., London, **A65**, 349-354.

Hokstad, K., 2000, Multicomponent Kirchhoff migration: Geophysics, **65**, 861-871.

Hornbach, M. J., Demian, M. S., and Holbrook, W. S., 2004, Critically pressured free-gas reservoirs below gas-hydrate provinces: Nature, **427**, 142-144.

Horne, S., and Leaney, S., 2000, Polarization and slowness component inversion for TI anisotropy: Geophys. Pros., **48**, 779-788.

Hou, A., and Marfurt, K. J., 2002, Multicomponent prestack depth migration by scalar wavefield extrapolation: Geophysics, **67**, 1886-1894.

Hudson, J., 1981, Wave speeds and attenuation of elastic waves in materials containing cracks: Geophys. J. R. astr. Soc., **64**, 133-150.

Hyndman, R. D., and Spence, G. D., 1992, A seismic study of methane hydrate marine bottom simulating reflectors: J. Geophys. Res., **97**, 6683-6698.

Ingber, L., 1989, Very fast simulated reannealing: Math. Comput. Modeling, **12**, 967-993.

Isaac, J. H., and Lawton, D. C., 1999, Image mispositioning due to dipping TI: A physical seismic modeling study: Geophysics, **64**, 1230-1238.

Jakobsen, M., Hudson, J. A., Minshull, T. a., and Singh, S. C., 2000, Elastic properties of hydrate-bearing sediments using effective medium theory: J. Geophys. Res., **105**, 561-577.

Jin, S, Madariaga, R., Virieux, J., and Lambaré, G., 1992, Two-dimensional asymptotic iterative elastic inversion: Geophys. J. Int., **108**, 575-588.

Jin, S., Gambois, G., and Vuillermoz, C., 2000, Shear-wave velocity and density estimation from PS-wave AVO analysis: Application to an OBS dataset from the North Sea: Geophysics, **65**, 1446-1454.

Kennett, B. L. N., 1983, Seismic wave propagation in stratified media: Cambridge University Press, Cambridge.

Kumar, D., Sen, M. K., and Ferguson, R. J., 2003, Traveltime calculation and prestack depth migration in tilted transversely isotropic media: SEG, Dallas, Expanded Abstracts, 941-944.

——— 2004a, Traveltime calculation and prestack depth migration in tilted transversely isotropic media: Geophysics, **69**, 37-44.

Kumar, D., and Sen, M. K., 2004, Traveltime calculation in tilted transversely isotropic media: 5th Conference and Exhibition on Petroleum Geophysics, Hyderabad, Expanded Abstracts, 1002-1005.

Kumar, D., Sen, M. K., and Bangs, N. L., 2004b, P-wave seismic anisotropy on Hydrate Ridge: SEG, Denver, Expanded Abstracts, 159-162.

Kvenvolden, K. A., 1988, Methane hydrate – a major reservoir of carbon in the shallow geosphere?: Chem. Geol., **71**, 41-51.

─────── 1993, Gas hydrates – geologic perspective and global change: Rev. Geopys., **31**, 173-187.

─────── 1999, Potential effects of gas hydrate on human welfare: Proceedings of the National Academy of Science, USA, **96**, 3420-3426.

Lay, T., and Wallace, T. C., 1995, Modern global seismology: Academic press.

Lecomte, I., 1993, Finite difference calculation of first traveltimes in anisotropic media: Geophys., J. Int., **113**, 318-342.

Le Rousseau, J. H., 1997, Depth migration in heterogeneous, transversely isotropic media with the phase-shift-plus-interpolation method: SEG, Expanded Abstracts, 1703-1706.

Leaney, W. S., Sayers, C. M., and Miller, D. E., 1999, Analysis of multiazimuthal VSP data for anisotropy and AVO: Geophysics, **64**, 1172-1180.

Lee, M. W., Hutchinson, D. R., Collett, T. S. & Dillon, W. P., 1996, Seismic velocities for hydrate-bearing sediments using weighted equation: J. Geophys. Res. **101**, 20347-20358.

Love, A. E. H., 1944, A treatise on the mathematical theory of elasticity: 4th ed, Dover, New York.

Lu, S., and McMechan, G. A., 2002, Estimation of gas hydrate and free gas saturation, concentration, and distribution from seismic data: Geophysics **67**, 582-593.

MacBeth, C., 2002, Multi-component VSP analysis for applied seismic anisotropy: Handbook of Geophysical Exploration, **26**, Pergamon Publ.

MacBeth, C., and Crampin, S., 1991, Comparison of signal processing techniques for estimating the effects of anisotropy: Geophy. Prosp., **39**, 357-385.

MacKay, M. E., 1995, Structural variation and landward vergence at the toe of the Oregon accretionary prism: Tectonics **14**, 1309-1320.

Mallick, S., Huang, X., Lauve, J., and Ahmad, R., 2000, Hybrid seismic inversion: a reconnaissance tool for deepwater exploration: The Leading Edge, **19**, 1230-1237.

Menke, W., 1984, Geophysical data analysis: Discrete inverse theory: Acad. Press

Milkov, A. et al., 2004, Co-existence of gas hydrate, free gas, and brine within the regional gas hydrate stability zone at Hydrate Ridge (Oregon margin): evidence from prolonged degassing of a pressurized core: Earth Planet. Sci. Lett., **222**, 829-843.

Miller, D. E., and Spencer, C., 1994, An exact inversion for anisotropic moduli from phase slowness data: J. Geophys. Res., **99**, 21651-21657.

Mukherjee, A., 2002, Seismic data processing in transversely isotropic media: A plane wave approach: PhD thesis, The University of Texas at Austin.

Nakamura, Y., Donoho, P. L., Roper, P. H., and McPherson, P. M., 1987, Large-offset seismic surveying using ocean-bottom seismographs and air guns: Instrumentation and field technique: Geophysics, **52**, 1601-1611.

Nikitin, L. V., and Chesnokov, E. M., 1984, Wave propagation in elastic media with stress-induced anisotropy: Geophys. J. R. astr. Soc., **76**, 129-133.

Nye, J. F., 1957, Physical properties of crystals: Oxford Press.

Pecher, I. A. et al., 2003, Seismic anisotropy in gas-hydrate and gas-bearing sediments on the Blake Ridge, from a walkaway vertical seismic profile: Geophys. Res. Lett., **30**, 1733-1736.

Podvin, P., and Lecomte, I., 1991, Finite-difference computation of traveltimes in very contrasted velocity models: A massively parallel approach and its associated tools: Geophys. J. Int., **105**, 271-284.

Pšenčík, I., 1998, Green's sunctions for inhomogeneous weakly anisotropic media: Geophys. J. Int., **135**, 279-288.

Qian, J., and Symes, W., 2002, Finite-difference quasi-P traveltime for anisotropic media: Geophysics, **67**, 147-155.

Rajan, S. D., and Frisk, G. V., 1989, A comparison between the Born and Rytov approximations for the inverse backscattering problem: Geophysics, **54**, 864-871.

Riddihough, R., 1984, Recent movements of the Juan de Fuca plate system: J. Geophys. Res., **89**, 6980-6994.

Riedel, M., Spence, G. D., Chapman, N. R., and Hyndman, R. D., 2001, Deep-sea gas hydrates on the northern Cascadia margin: The Lead. Edge, **20**, 87-92.

Rüger, A., 1998, Variation of P-wave reflectivity with offset and azimuth in anisotropic media: Geophysics, **63**, 935-947.

Sayers, C. M., 1994, The elastic anisotropy of shales: J. Geophys. Res., **99**, 767-774.

———1997, Determination of anisotropic velocity models from walkaway VSP data acquired in the presence of dip: Geophysics, **62**, 723-729.

Schneider, W. A. J., Ranzinger, K., Balch, A., and Kruse, C., 1992, A dynamic programming approach to first arrival travel time computation in media with arbitrarily distributed velocities: Geophysics, **57**, 39-50.

Schneider, W. A., 1978, Integral formulation for migration in two and three dimensions: Geophysics, **43**, 49-76.

Schoenberg, M., and Douma, J., 1988, Elastic wave propagation in media with parallel fractures and aligned cracks: Geophy. Prosp., **36**, 571-590.

Sen, M. K., 2002, Lecture notes on Advanced Theoretical Seismology: available online, http://www.ig.utexas.edu/people/students/classes/spring02/geo391/

Sen, M. K., and Mukherjee, A., 2003, τ-p analysis in transversely isotropic media: Geophys. J. Int., **154**, 647-658.

Sen, M. K., and Stoffa, P. L., 1991, Nonlinear one-dimensional seismic waveform inversion using simulated annealing: Geophysics, **56**, 1624-1638.

——— 1995, Global optimization method in geophysical inversion: Elsvier Sci. Publ. Co., The Netherlands.

Sena, A. G., and Toksöz, M. N., 1993, Kirchhoff migration and velocity analysis for converted and nonconverted waves in anisotropic media: Geophysics, **58**, 265-276.

Sethian, J., and Popovici, A., 1999, 3-D traveltime computation using the fast marching method: Geophysics, **64**, 516-523.

Shipley, T. H. et al., 1979, Seismic evidence for widespread possible gas hydrate horizons on continental slopes and rises: AAPG Bulletin, **63**, 2204-2213.

Silver, P. G., 1996, Seismic anisotropy beneath the continents: probing the depth of geology: Ann. Rev. Earth Planet. Sci., **24**, 385-432.

Silver, P. G., and Chan, W. W., 1988, Implications for continental structures and evolution from seismic anisotropy: Nature, **335**, 34-39.

Sloan, E. D. Jr., 2000, Clathrate hydrates of natural gases: 3rd ed. Marcel Dekker, New York.

——— 2003, Fundamental principles and applications of natural gas hydrates: Nature, **426**, 353-359.

Stephen, R.A., 1985, Seismic anisotropy in the upper oceanic crust: J. Geophys. Res., **90**, 11383-11396.

Stewart, R. R., Gaiser, J. E., Brown, R. J., and Lawton, D. C., 2002, Converted-wave seismic exploration: Methods: Geophysics, **67**, 1348-1363.

——— 2003, Converted-wave seismic exploration: Applications: Geophysics, **68**, 40-57.

Stoffa, P. L., Buhl, P., Diebold, J. B., and Wenzel, F., 1981, Direct mapping of seismic data to the domain of intercept time and ray parameter—A plane-wave decomposition: Geophysics, **46**, 410–421.

Stoffa, P. L., Fokkema, J., de Luna Freire, R., Kessinger, W., 1990, Split-step fourier migration: Geophysics, **55**, 410-421.

Stolt, R. H., 1978, Migration by Fourier transform: Geophysics, **43**, 23-48.

Stolt, R. H., and Weglein, A. B., 1985, Migration and inversion of seismic data: Geophysics, **50**, 2458-2472.

Suess, E. et al., 2001, Sea floor methane hydrates at Hydrate Ridge, Cascadia Margin. In C. K. Paull & W. P. Dillon, Natural gas hydrates: Occurrence, distribution, and detection: AGU monograph **124**, Washington DC.

Tarantola, A., 1987, Inverse problem theory: Methods of data fitting and model parameter estimation: Elsevier Publication Company.

Tatham, R. H., and Stoffa, P. L., 1976, V_P/V_S – A potential hydrocarbon indicator: Geophysics, **41**, 837-849.

Tatham, R. H., and McCormack, M. D., 1991, Multicomponent seismology in petroleum exploration: Soc. Expl. Geophys.

Tessmer, G., and Behle, A., 1988, Common reflection point data-stacking technique for converted waves: Geophysical Prospecting, **36**, 671-688.

Thomsen, L., 1986, Weak elastic anisotropy: Geophysics, **51**, 1954-1966.

——— 2002, Understanding seismic anisotropy in exploration and exploitation: SEG/EAGE Distinguished Instructor Series 5, Soc. Expl. Geophys., Tulsa.

Trehu, A. M., Torres, M. E., Moore, G. F., Suess, E., and Bohrmann, G., 1999, Temporal and spatial evolution of a gas-hydrate-bearing accretionary ridge on the Oregon continental margin: Geology **27**, 939-942.

Trehu, A. M., Bohrmann, G., Rack, F. R., Torres, M. E., and Leg 204 Scientific Party, 2003, Proceedings of the Ocean Drilling Program, Initial Reports, **204**, online at: http://www-odp.tamu/publications/204_IR/204TOC.HTM.

Trehu, A. M. et al., 2004, Three-dimensional distribution of gas hydrate beneath southern Hydrate Ridge: constraints from ODP Leg 204: Earth Planet. Sci. Let. **222**, 845-862.

Treitel, S., and Lines, L., 1982, Linear inverse theory and deconvolution: Geophysics, **47**, 1153-1159.

Trorey, A. W., 1970, A simple theory for Seismic Diffraction: Geophysics, **35**, 762-784.

Tsvankin, I., 1996, P-wave signatures and notation for transversely isotropic media: an overview: Geophysics, **61**, 467-483.

——— 1997a, Reflection moveout and parameter for horizontal transverse isotropy: Geophysics, **62**, 614-629.

——— 1997b, Moveout analysis for transversely isotropic media with a tilted symmetry axis: Geophys. Prosp., **45**, 479-512.

——— 2001, Seismic signatures and analysis of reflection data in anisotropic media: Pargamon, Oxford.

Tsvankin, I., and Thomsen, L., 1994, Nonhyperbolic reflection moveout in anisotropic media: Geophysics, **59**, 1290-1304.

——— 1995, Inversion of reflection traveltimes for transverse isotropy: Geophysics, **60**, 1095-1107.

Um, J., and Thurber, C., 1987, A fast algorithm for two-point seismic ray tracing: *Bull. Seis. Soc. Am.*, **77**, 972-986.

van der Bann, M., and Kendall, J. M., 2002, Estimating anisotropy parameters and traveltime in the τ-p domain: Geophysics, **67**, 1076-1086.

van Trier, J., and Symes, W. W., 1991, Upwind finite-difference calculation of traveltimes: Geophysics, **56**, 812-821.

Vavryčuk, V., 1997, Elastodynamic and elastostatic Green tensors for homogeneous weak transversely isotropic media: Geophys. J. Int., **130**, 786-800.

Vernik, L., and Liu, X., 1992, Ultrasonic velocity and anisotropy of hydrocarbon source-rocks: Geophysics, **57**, 727-735.

———— 1997, Velocity anisotropy in shales: A petrophysical study: Geophysics, **62**, 521-532.

Vestrum, R. W., 2001, Exploration applications of seismic velocity anisotropy: Abstract, Annual meeting, Canadian Soc. Expl. Geophys.

Vestrum, R. W., Lawton D. C., and Schmid, R., 2001, Imaging structures below dipping TI media: Geophysics, **64**, 1239-1246.

Vidale, J. E., 1986, Complex polarization analysis of particle motion: Bull. Seis. Soc. Am., **76**, 1393-1405.

———— 1988, Finite-difference calculation of travel times: Bull. Seis. Soc. Am., **78**, 2062-2076.

———— 1990, Finite-difference calculation of travel times in three dimensions: Geophysics, **55**, 521-526.

Vinje, V., Iversen, E., and Gjøystdal, H., 1993, Traveltime and amplitude estimation using wavefront construction: Geophysics, **58**, 1157-1166.

Wang, C., 2003, Velocity estimation from seismic data by nonlinear inversion and characterization of gas hydrate deposits offshore Oregon: PhD thesis, The University of Texas at Austin.

Wang, Z., 2002, Seismic anisotropy in sedimentary rocks, part 2: laboratory data: Geophysics, **67**, 1423-1440.

White, J. E., 1982, Computed waveforms in transversely isotropic media: Geophysics, **47**, 771-783.

Winterstein, D. F., 1990, Velocity anisotropy terminology for geophysicists: Geophysics, **55**, 1070-1088.

Winterstein, D. F., and Meadows, M. A., 1991, Shear-wave polarizations and subsurface stress directions at Lost Hills field: Geophysics, **56**, 1331-1348.

Winterstein, D. F., and Paulson, B. N. P., 1990, Velocity anisotropy in shales determined from crosshole seismic & VSP data: Geophysics, **55**, 470-479.

Wood, A. B., 1941, Text book of sounds, 578 pp., Macmillan, New York.

Wyllie, M. R., Gregory, A. R., and Gardner, G. H. P., 1958, An experimental investigation of factors affecting elastic wave velocities in porous media: Geophysics, **23**, 459-493.

Xia, G., Sen, M. K., and Stoffa, P. L., 1998, 1-D elastic waveform inversion: A divide-and-conquer approach: Geophysics, **63**, 1670-1684.

———— 2000, Mapping of elastic properties of gas hydrates in the Carolina trough by waveform inversion: Geophysics, **65**, 725-744.

Yilmaz, O., 2001, Seismic data analysis: processing, inversion, and interpretation of seismic data: 2nd Ed., Society of Exploration Geophysicists, Tulsa.

Yuan, J., 2001, Analysis of four-component seafloor seismic data for seismic anisotropy: PhD thesis, The University of Edinburgh.

Yuan, T., Hyndman, R. D., Spence, G.D., and Desmons, B., 1996, Seismic velocity increase and deep-sea gas hydrate concentration above a bottom-simulating reflector on the northern Cascadia continental slope: J. Geophys. Res. **101**, 13655-13671.

Zhe, J., and Greenhalgh, S. A., 1997, Prestack multicomponent migration: Geophysics, **62**, 590-613.

Zhu, X., Altan, S., and Li, J., 1999, Recent advances in multicomponent processing: The Leading Edge, **18**, 1283-1288.

Vita

Dhananjay Kumar was born in Jehanabad, Bihar, India, on January 12, 1976, to Sr. Raghunath Singh and Smt. Shanti Devi. He completed his high school from M. H. S., Jehanabad in 1990, and secondary level education from S. S. College, Jehanabad, India in 1992. He entered the Department of Geology and Geophysics at the Indian Institute of Technology, Kharagpur, India in 1995. He graduated with the Master of Science degree in Exploration Geophysics in 2000. During June 2000 to August 2001, he worked for Reliance Industries Limited, Mumbai, as a Geophysicist. In August 2001, he enrolled in the PhD program in the Department of Geological Sciences at the University of Texas at Austin. During the summer of 2003 he worked for BP America Inc, with Seismic Advanced Imaging Team, EPTG, Houston as a Geophysicist. Upon graduation he will join ChevronTexaco's Energy Technology Company, Reservoir Properties from Seismic Services Team, Subsurface Characterization in San Ramon, California. He is a member of SEG, EAGE, AGU, and SPG.

Permanent address: Baba Chauk, N Patel Nager, Road – 8, Patna-24, India.

This dissertation was typed by the author.